Springer ThesesRecognizing Outstanding Ph.D. Research

Akari Takayama

High-Resolution Spin-Resolved Photoemission Spectrometer and the Rashba Effect in Bismuth Thin Films



Springer Theses

Recognizing Outstanding Ph.D. Research

Aims and Scope

The series "Springer Theses" brings together a selection of the very best Ph.D. theses from around the world and across the physical sciences. Nominated and endorsed by two recognized specialists, each published volume has been selected for its scientific excellence and the high impact of its contents for the pertinent field of research. For greater accessibility to non-specialists, the published versions include an extended introduction, as well as a foreword by the student's supervisor explaining the special relevance of the work for the field. As a whole, the series will provide a valuable resource both for newcomers to the research fields described, and for other scientists seeking detailed background information on special questions. Finally, it provides an accredited documentation of the valuable contributions made by today's younger generation of scientists.

Theses are accepted into the series by invited nomination only and must fulfill all of the following criteria

- They must be written in good English.
- The topic should fall within the confines of Chemistry, Physics, Earth Sciences, Engineering and related interdisciplinary fields such as Materials, Nanoscience, Chemical Engineering, Complex Systems and Biophysics.
- The work reported in the thesis must represent a significant scientific advance.
- If the thesis includes previously published material, permission to reproduce this must be gained from the respective copyright holder.
- They must have been examined and passed during the 12 months prior to nomination.
- Each thesis should include a foreword by the supervisor outlining the significance of its content.
- The theses should have a clearly defined structure including an introduction accessible to scientists not expert in that particular field.

More information about this series at http://www.springer.com/series/8790

Akari Takayama

High-Resolution
Spin-Resolved
Photoemission Spectrometer
and the Rashba Effect
in Bismuth Thin Films

Doctoral Thesis accepted by Tohoku University, Sendai, Japan



Author
Dr. Akari Takayama
Department of Physics
Graduate School of Science
and Faculty of Science
Tohoku University
Sendai
Japan

Supervisor
Prof. Takashi Takahashi
Advanced Institute for Materials Research
(WPI-AIMR)
Tohoku University
Sendai
Japan

ISSN 2190-5053 ISBN 978-4-431-55027-3 DOI 10.1007/978-4-431-55028-0

ISSN 2190-5061 (electronic) ISBN 978-4-431-55028-0 (eBook)

Library of Congress Control Number: 2014947650

Springer Tokyo Heidelberg New York Dordrecht London

© Springer Japan 2015

This work is subject to copyright. All rights are reserved by the Publisher, whether the whole or part of the material is concerned, specifically the rights of translation, reprinting, reuse of illustrations, recitation, broadcasting, reproduction on microfilms or in any other physical way, and transmission or information storage and retrieval, electronic adaptation, computer software, or by similar or dissimilar methodology now known or hereafter developed. Exempted from this legal reservation are brief excerpts in connection with reviews or scholarly analysis or material supplied specifically for the purpose of being entered and executed on a computer system, for exclusive use by the purchaser of the work. Duplication of this publication or parts thereof is permitted only under the provisions of the Copyright Law of the Publisher's location, in its current version, and permission for use must always be obtained from Springer. Permissions for use may be obtained through RightsLink at the Copyright Clearance Center. Violations are liable to prosecution under the respective Copyright Law. The use of general descriptive names, registered names, trademarks, service marks, etc. in this publication does not imply, even in the absence of a specific statement, that such names are exempt from the relevant protective laws and regulations and therefore free for general use.

While the advice and information in this book are believed to be true and accurate at the date of publication, neither the authors nor the editors nor the publisher can accept any legal responsibility for any errors or omissions that may be made. The publisher makes no warranty, express or implied, with respect to the material contained herein.

Printed on acid-free paper

Springer is part of Springer Science+Business Media (www.springer.com)

Parts of this thesis have been published in the following journal articles:

- [1] "Tunable spin polarization in bismuth ultrathin film on Si(111)" A. Takayama, T. Sato, S. Souma, T. Oguchi, and T. Takahashi Nano Letters **12**, 1776 (2012)
- [2] "Giant out-of-plane spin component and the asymmetry of spin-polarization in surface Rashba states of bismuth thin film"
 - A. Takayama, T. Sato, S. Souma, and T. Takahashi Phys. Rev. Lett. **106**, 166401 (2011)
- [3] "Ultrahigh-resolution spin-resolved photoemission spectrometer with a mini Mott detector"
 - S. Souma, A. Takayama, K. Sugawara, T. Sato, T. Takahashi Rev. Sci. Instrum. **81**, 095101 (2010)

Supervisor's Foreword

The physical and chemical properties of materials are dominated by the nature of valance electrons included therein. A complete description of the electronic state of solids is formulated by a set of three basic parameters of electrons: energy (E), momentum (k), and spin. Among various experimental methods to study the electronic states of matter, angle-resolved photoemission spectroscopy (ARPES) is regarded as a unique and powerful experimental technique, which provides direct information on the relationship between the energy and momentum of electrons, namely the band structure. Recent remarkable progress of the energy resolution in ARPES has made it possible to study the detailed electronic structure in the vicinity of the Fermi level $(E_{\rm F})$ responsible for observed novel properties such as superconductivity. Spin-resolved measurement in ARPES has been long pursued because it completes the determination of all the three key parameters of electrons, and is expected to serve as a powerful method to investigate the exotic quantum properties originating from the electron spin. However, spin-resolved ARPES has an inherent difficulty in achieving a high energy resolution because the efficiency of detecting the electron spin polarization is typically three to four orders of magnitude lower than that in the non-spin-resolved measurement.

The present thesis describes the development and construction of a high-resolution spin-resolved photoemission spectrometer by overcoming the above-mentioned difficulty. The newly constructed spectrometer achieves the energy resolution of 8 meV, which is ten times better than that of the previous spectrometers (typically 100 meV) and is the world-best record at present. An important development to achieve this high resolution is a highly efficient mini Mott detector with a remarkably low noise level by overcoming the accidental discharge between electrodes at high voltage. Another noticeable aspect of the new spectrometer is a parallel-detection system with the multichannel plate and the Mott detector. This allows us to specify the energy and momentum of electrons with high accuracy during spin detection, enabling us to determine the momentum dependence of spin polarization with a high reliability that the previous single-Mott-type spectrometer never achieved.

By using the newly constructed spectrometer, the surface electronic state of Bi(111) has been investigated in great detail. Previous theoretical and experimental studies reported the spin-split surface band on Bi(111) originating from the Bi 6p orbital. This spin-split band is ascribed to the surface Rashba band, where the spin degeneracy is lifted by a combination of the strong spin-orbit coupling and the lack of the space inversion symmetry (SIS) at surface. The standard model of the Rashba effect supposes a purely two-dimensional (2D) SIS, so that the spin of the electron is laid on the surface plane and, at the same time, directed perpendicularly to the electron momentum. This results in a 2D vortex spin texture of the Fermi surface in the momentum space. In contrast to this simple picture, the present work has revealed the anomalous spin texture deviated from the standard Rashba model. The spin polarization shows strong anisotropy even in the plane, and, more surprisingly, shows a sizable out-of-plane component. This result requests further sophistication of theory in describing the anomalous behavior of spin at the surface.

The present study also provides a useful hint for application to spintronic devices. This study reports the systematic change in spin polarization as a function of film thickness in a high-quality Bi thin film grown on Si crystal. The spin polarization at surface is reduced by decreasing the film thickness. This indicates the existence of a spin-polarized state at the interface between Bi film and Si surface in a manner similar to the surface, but with the opposite spin polarization. This finding of the Rashba effect at the interface would open a way for fabricating stable and highly efficient heavy-element-based spintronic devices, because the interface is much more stable than the surface and the magnitude of spin-splitting is far larger than that of semiconductor-based devices, both of which are favorable to advanced spintronic devices.

In this book, readers will see the recent remarkable progress and the present status of spin-resolved ARPES. The book also shows how spin-resolved ARPES unravels the anomalous spin-resolved electronic structure responsible for the novel properties of materials. I believe that this book will be useful for not only photoemission specialists but also for students and general materials science researchers, because in the near future spin-resolved ARPES will be widely utilized in various research fields as one of the most essential tools to study the electronic states of materials.

Sendai, March 2014

Prof. Takashi Takahashi

Acknowledgments

I would like to acknowledge the immense support from Prof. Takashi Takahashi, who was my supervisor during my Ph.D. course. He advised me on many things such as how to conduct research, how to write a paper, and how to present data at a conference. I have learned a lot from him.

I am also thankful to Associate Professor Takafumi Sato and Assistant Professor Seigo Souma for discussing my experimental data and advising me on physics when writing papers. They have also advised me about essential techniques and methods necessary for the ARPES measurements.

Many thanks to Assistant Professors Katsuaki Sugawara and Kosuke Nakayama for their instructions and guidance, as in the preparation of a sample and the repair of apparatus. They have also advised me to spend my life in academia.

I would like to express my great appreciation to Professor Tamio Oguchi at Osaka University. He has given me many useful suggestions and comments from the point of view of theory and band-structure calculations.

I also thank the members of my laboratory for helping with my experiments: Dr. Toshiyuki Arakane, Dr. Tian Qian, Dr. Pierre Richard, Dr. Ang Ran, Yutaka Tago, Yoichi Sekiba, Kenta Mizuno, Kazuki Ise, Takuma Kawahara, Takayuki Mori, Guo Hua, Kotaro Umezawa, Kohei Kanetani, Kenichiro Kosaka, James Kleeman, Makoto Komatsu, Yusuke Tanaka, Ei Ieki, Toru Takahashi, Madoka Nomura, Takuya Shoman, Eiichi Noguchi, Kohei Honma, and Yasunari Miyata.

I would like to thank Peter Baltzer and Mitsuse Matsuki at MB Scientific for very helpful cooperation in the development of the spin-resolved ARPES system.

I am also grateful to all the staff members of the Tohoku University Technical Center for producing components necessary for my research. I would like to thank the administrative staff for taking care of many issues in the office, and I am very grateful to JSPS for financial support.

Finally, I want to acknowledge my family. Without their understanding and support, I could not have completed my Ph.D. study.

Contents

1	Introduction								
	1.1	Preface							
	1.2		round	2					
		1.2.1	Spin-Resolved Photoemission Spectroscopy	2					
		1.2.2	Rashba Effect	4					
		1.2.3	Group-V Semimetal Bismuth	8					
	1.3	Purpos	se of the Present Research	10					
	Refe	erences		12					
2	Basi	ic Princ	ciple of Photoemission Spectroscopy						
	and Spin Detector								
	2.1	-	emission Spectroscopy	15					
		2.1.1	Principle of Photoemission Spectroscopy	15					
		2.1.2	Angle-Resolved Photoemission Spectroscopy	17					
		2.1.3	Photoemission Spectral Function	19					
		2.1.4	Photoemission Spectral Intensity	21					
		2.1.5	Energy Distribution Curve and Momentum						
			Distribution Curve	22					
	2.2 Spin Detector								
		2.2.1	Various Spin Detectors	22					
		2.2.2	Principle of the Mott Scattering	24					
		2.2.3	Mott Detector	26					
		2.2.4	Derivation Method of Spin Polarization Spectrum	28					
	Refe	erences		29					
3	Dev	elopme	nt of High Resolution Spin-Resolved Photoemission						
•		_	er	31					
	3.1		e	31					
	3.2		and Construction	32					
			Mott Detector	32					
		3.2.2	Improvement of Hemispherical Analyzer System	34					

xii Contents

		3.2.3 Deflector						
		3.2.4 Discharge Problems						
		3.2.5 Surface Chamber						
		3.2.6 Other Refinements						
	3.3	System Test						
		3.3.1 Energy Resolution						
		3.3.2 Spin-Polarization						
		3.3.3 Sharman Function of the Mott Detector						
	3.4	Summary						
	Refe	erences						
4	Anomalous Rashba Effect of a Bi Thin Film on Si(111)							
	4.1	Background and Goal of Research						
	4.2	Experimental Conditions						
	4.3	Results and Discussions						
	4.4	Summary						
	Refe	erences						
5	Rashba Effect at Interface of a Bi Thin Film on Si(111)							
	5.1							
	5.2	Results and Discussions						
	5.3	Summary						
	Refe	References						
6	Con	Conclusion						
	6.1	Development of Ultrahigh-Resolution Spin-Resolved						
		Photoemission Spectrometer						
	6.2	Elucidation of Rashba Effect for Bi/Si(111) Thin Film						
		by Spin-Resolved ARPES						
	6.3	Future Plans						
Cı	ırricı	ulum Vitae						

Chapter 1 Introduction

Recently, development of new spintoronic devices without applying a magnetic field has been a target of intensive researches. The Rashba effect, which appears in the two-dimensional plane such as a surface and an interface, has been regarded as a useful candidate to develop the next-generation spintronic devices owing to the spin split nature of bands originating from the spin-orbit coupling. Spin-resolved photoemission spectroscopy is a powerful experimental technique which can simultaneously determine all key quantum parameters of electrons in solids, *i.e.*, momentum, energy, and spin. Although the spin-resolved photoemission spectroscopy is an ideal technique to clarify the details of the Rashba effect, it is not so widely used so far because of its low efficiency to detect spin polarization. It is thus urgently required to improve the performance of the spin-resolved photoemission spectrometer and to elucidate the nature of Rashba-type spin state for the development of new spintronic devices.

1.1 Preface

Angle-resolved photoemission spectroscopy (ARPES) is a powerful experimental technique which can measure energy states of electrons emitted to the vacuum from solids, gases, and liquids by the photoelectric effect. Especially, this technique has contributed to the material science since it observes simultaneously two of three essential parameters of an electron, energy (E) and momentum (k), i.e., the band dispersion. The performance of the ARPES spectrometer has improved drastically after the discovery of high-temperature superconductivity in 1986 [1]. Now the energy and angle resolutions are better than 1 meV and 0.1°, respectively. Recent remarkable progress in the energy resolution of the ARPES spectrometer has made it possible to investigate the fine electronic structure in the vicinity of the Fermi level ($E_{\rm F}$) such as the quasiparticles responsible for anomalous physical properties [2].

On the other hand, the recent development of high-functionality spintronic devices which utilize another electron degrees of freedom, *i.e.*, "spin", has attracted particular attention in both basic science and applications. In particular, hard-disk

1

2 1 Introduction

capacity was drastically enhanced by the discovery of giant magneto resistance (GMR) [3, 4] and tunneling magneto resistance (TMR) [5, 6] (Nobel Prize for Physics in 2007). And also, the device applying diluted magnetic semiconductor is studied for compatible with electronics devices [7]. Very recently, the spin-related phenomenon a produced by the spin-orbit interaction at the surface or the interface of the non-magnetic material have attracted considerable interest because the spinorbit interaction enables the generation and manipulation of spin-polarized electrons solely by an electric field. The Rashba effect [8] is known as a typical example of such a system which can be applied to the next generation spintronic devices. In the Rashba surface state, the spin direction of an electron has a strong connection to an electron momentum, thus the spin-resolved ARPES technique could be served as an excellent technique which enables the complete determination of all three electron degrees of freedom. However, in contrast to the conventional ARPES, the spin-resolved ARPES technique involves an inherent difficulty in achieving highenergy resolution because the efficiency to detect spin polarization is typically 3 orders of magnitude lower than that of the non spin-resolved measurement. Actually, the typical energy resolution of conventional spin-resolved photoemission spectrometers is about ~100 meV, therefore it is difficult to investigate various functional properties of novel materials where the spin of electrons plays an essential role in realizing the exotic physical properties.

This chapter briefly explains the current situations and issues for spin-resolved photoemission spectrometer. Basic characteristics of the Rashba effect are also discussed with a particular focus on the group-V semimetal bismuth (Bi).

1.2 Background

1.2.1 Spin-Resolved Photoemission Spectroscopy

Spin-resolved photoelectron spectroscopy is an experimental technique which was established around late 1980s and 1990s [9], and this technique greatly contributed to the understanding of the origin of magnetism, through the observation of, *e.g.*, the exchange spin splitting of electronic states in the valence band of ferromagnetic metals, since the spin-resolved photoemission technique can directly detect the electron spin [10, 11]. There are several kinds of spin detectors which are installed to a spin-resolved photoemission spectrometer [12–15]. Among various spin detectors, the Mott detector, which was theoretically discussed for the first time by Mott in 1932, is most commonly used for spin-resolved ARPES measurements [12]. The Mott detector observes the electron spin by a high-energy spin-dependent electron scattering (25 ~ 100 keV) with targets containing heavy-mass elements such as Au and Th. The reason why the Mott detector is used widely is because its stability and the self-calibrated nature. Since the electron scattering of the Mott detector takes place at high energy, the machine condition sustains almost permanently because the target surface is hard to be polluted by incident electrons.

1.2 Background 3

However, many high-energy electrons are transmitted and absorbed into the target when it hits the target, and the detection efficiency of electrons becomes 3 to 4 orders of magnitude lower due to multiply-scattered electrons which lost the information of spin. In addition, the most critical problem is an electric discharge caused by the application of high voltage. In order to obtain enough statistics and precision in spin-resolved ARPES measurements using a Mott detector, a realistic energy resolution during the measurement was set to be around 100 meV, which is 2 orders of magnitude lower than the normal ARPES measurements (< 1 meV). While spin-resolved measurements with the high-intensity light sources, such as the third-generation synchrotron light, the ultraviolet lasers, and the laboratory sources using the plasma excitation of rare gases, has been performed, it is still difficult to perform the spin-resolved measurement with sufficiently high resolution.

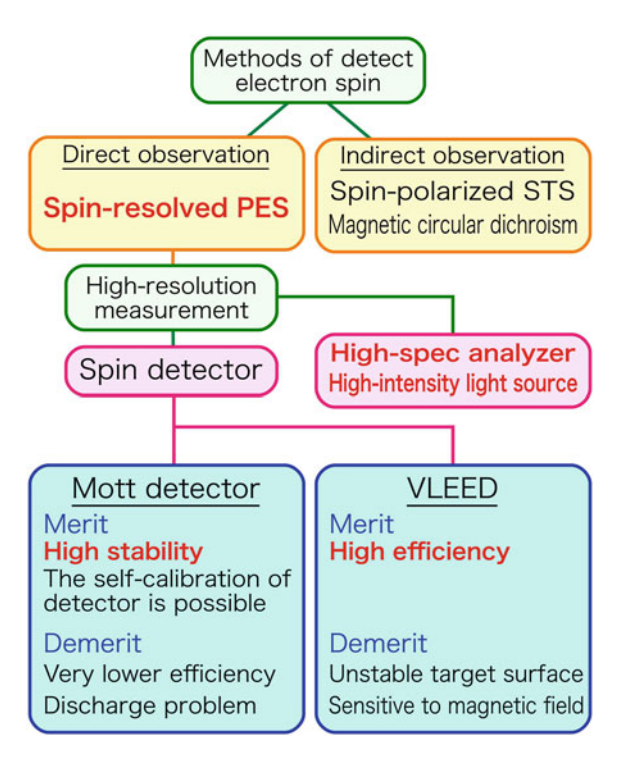
Another spin detector used for the spin-resolved ARPES measurement is based on the very-low-energy electron diffraction (VLEED), which utilizes the lowenergy electron scattering (reflection) from the spin-exchange split unoccupied states of ferromagnetic materials [15]. This method, which was reported in 1989, is expected to have higher efficiency than the Mott scattering method since a reflection probability of the low-energy electrons is approximately 10 times larger as compared to the backscattering probability of the high-energy electrons in the Mott detector. However, low-energy electrons are much more surface sensitive and thus the high performance of the VLEED detector cannot be maintained so long time owing to the oxidation of the Fe film target by the residual gas. This complexity of the target preparation and the quick deterioration of the Fe film prevent the use of the VLEED detector as a standard one in spite of its high efficiency. In 1998, Bertacco et al. reported that the Fe(001)- $p(1 \times 1)$ -O surface, which was intentionally fabricated by the oxidization of a Fe(001) film, markedly extends the lifetime of the film from a few hours to a few days [16]. Although the lifetime of the target is extended to be a several months recently, the VLEED detector has not been so widely used because of an inherently unstable nature of the target.

In addition to the photoelectron spectroscopy, there are various methods to observe a spin, such as an optical technique using the magnetic circular dichroism [17], and the spin-polarized scanning tunneling spectroscopy (STS) using the ferromagnetic probe [18]. However, these methods are difficult to discuss the details of electron spin since they essentially gives a momentum-integrated information so that it is hard to obtain experimentally the momentum dependence of the spin polarization.

Figure 1.1 displays the problems and required machine performance for the high-resolution measurements of spin-resolved ARPES. The problem we should overcome is low efficiency and stability of the detector. As for the spin detector which is connected to the photoemission spectrometer. The Mott detector and VLEED are preferable; the former has low efficiency with high-stability, while the latter, in contrast, has relatively high efficiency and unstable target surface. For the high-resolution spin resolved measurement, the most important is the efficiency of the detector, and second important is to obtain maximum performance of the analyzer because the energy resolution is essentially determined by the analyzer itself, namely, we need a high-spec analyzer. It is also effective to use a high-intensity excitation

4 1 Introduction

Fig. 1.1 Classification of detection methods of electron spin and the requirements for high-resolution measurements



light source to increase the efficiency. Moreover, to discuss the complicated spin structure like the Rashba states which strongly depends on momentum, we also need a measurement system which specifies the absolute momentum location.

1.2.2 Rashba Effect

The Rashba effect, which is caused by the strong spin-orbit coupling in the twodimensional surface or interface, is one of the most important physical phenomena which can be applied to the development of next-generation spintronic devices, since it enables the generation and manipulation of spin-polarized electrons solely by an electric field. In nonmagnetic solids, the electronic states with opposite spin have the same energy (Kramers' degeneracy) because of the time-reversal and the space-inversion symmetries.

More specifically, the following relation is requested from the space-inversion symmetries.

$$E(k,\uparrow) = E(-k,\uparrow) \tag{1.1}$$

1.2 Background 5

In addition, the following is also requested from the time-reversal symmetries.

$$E(k,\uparrow) = E(-k,\downarrow) \tag{1.2}$$

These two Eqs. (1.1) and (1.2) finally result in the following relation.

$$E(k,\uparrow) = E(k,\downarrow) \tag{1.3}$$

On the other hand, the relation (1.1) is not satisfied under the absence of the space-inversion symmetries such as surface or interface.

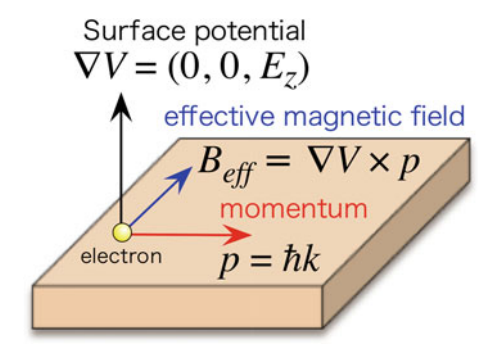
$$E(k,\uparrow) \neq E(k,\downarrow) \tag{1.4}$$

Therefore the spin degeneracy is lifted by the spin-orbit interaction, resulting in the splitting of energy bands. Now we explain an electronic spin state for free-electron model as a simple example of a broken space-inversion symmetry system. The Hamiltonian which takes into account the spin-orbit interaction term is expressed as

$$\hat{H} = \hat{H}_0 + \hat{H}_{so} = -\frac{\hbar^2}{2m} \nabla^2 + \frac{\hbar}{4m^2 c^2} \sigma \cdot (\nabla V \times p)$$
 (1.5)

where V is the crystal potential, p is the momentum operator, c is the velocity of light, and σ is the spin operator. The potential in the presence of the space inversion asymmetry can generate a net electric field. If the term $\nabla V \times p$ is considered as a magnetic field (effective magnetic field), the spin splitting arises because of the finite \hat{H}_{so} . Next we assume the case of two-dimensional free electron gas at the surface. As shown in Fig. 1.2, when an electron moves with momentum p, the electron feels potential gradient $\nabla V = (0, 0, E_z)$ along the surface normal. The $\nabla V \times p$ term acts as an effective magnetic field B_{eff} which is parallel to surface and orthogonal to $p = \hbar k$. As a result, the electron spin is quantized along the direction perpendicular to the wave vector k in the surface plane. The energy of free electron gives the following eigenvalues,

Fig. 1.2 Relationship between momentum and surface potential at surface



6 1 Introduction

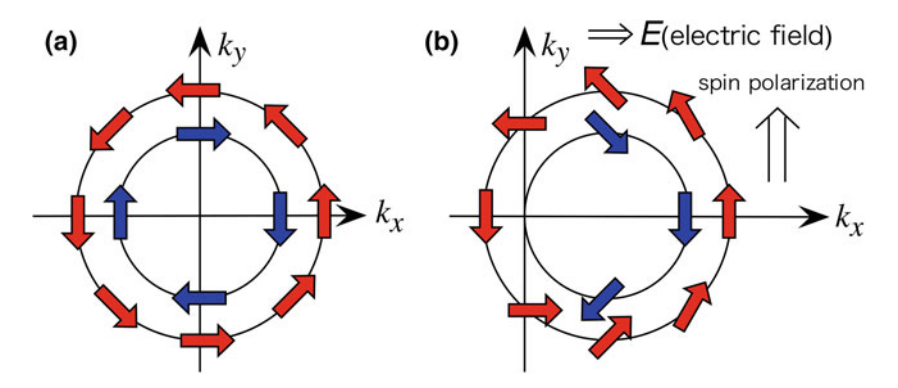


Fig. 1.3 Spin polarization vector expected for the Rashba effect at a normal Fermi surface and b Fermi surface with an applied voltage in two-dimensional free electron gas system

$$E(k) = \frac{\hbar^2}{2m}k^2 \pm \frac{\hbar^2 E_z}{4m^2 c^2}k = \frac{\hbar^2}{2m}k^2 \pm \alpha_R k$$
 (1.6)

which is well known as the Rashba effect, where α_R is a so-called Rashba parameter. This equation means that the free-electron-like parabolic band (Fig. 1.3a) splits into two bands along the k_{ll} -direction, and the positive term in the equation provides an inner state, while the negative term gives an outer one. There is a band crossing at $k_{ll} = 0$, and spins (also, B_{eff}) are anti-symmetric with respect to $k_{ll} = 0$ as required by the time-reversal symmetry. As shown in Fig. 1.3b, when the electric field is applied normal to the two-dimensional electronic-gas plane, the spin polarization arises along the direction orthogonal to the electric field.

The first observation of the surface Raahba effect by ARPES is the Au(111) surface [19]. LaShell et al. found two surface bands arising from the two-dimensional free-electron-like dispersion which exist within the gap of bulk band projection around the $\bar{\Gamma}$ point (Fig. 1.4). In normal metals, the size of band splitting by the Rashba effect is expected to be of μeV order at $k \approx 1 \text{ Å}^{-1}$, since the α_R value is of the order of $\approx 10^{-6} \text{ eV}\text{Å}$, as determined from the average surface vertical potential $(E_z \sim 1 \text{ eV})$ in the case of two-dimensional free electron at the surface. While the splitting size and the α_R value in Au(111) are 110 meV and 0.33 eVÅ, respectively, which are 5 orders of magnitude larger than that one expected from the free-electron model, the split nature of bands certainly confirms the Rashba state, as also reproduced by the calculation incorporating the spin-orbit coupling of Au 6p orbital [20]. Moreover, the spin structure of two concentric Fermi surfaces at the Γ point was verified by spin-resolved ARPES to be consistent with the Rashba picture [21]. These results suggest that the magnitude of the spin splitting by the Rashba effect depends on the strength of the atomic spin-orbit coupling, namely, the Rashba splitting becomes larger for heavier atom which has a strong spin-orbit coupling. Here, Rashba parameter α_R is given by

1.2 Background 7

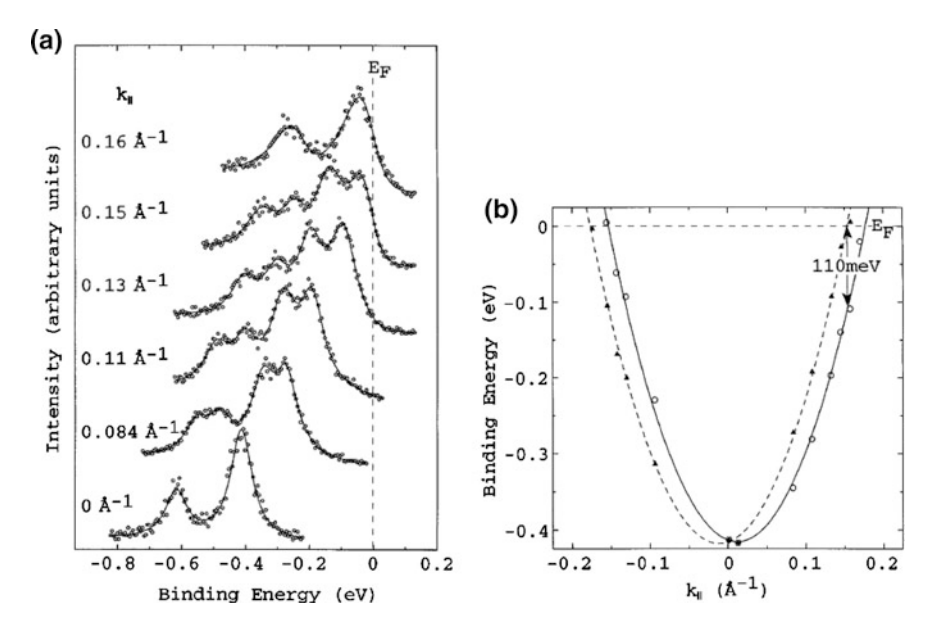


Fig. 1.4 a ARPES spectra and b band dispersion along the $\bar{\Gamma}$ - \bar{M} line (right) of Au(111) [19]

$$\alpha_R \propto \int \frac{\partial V}{\partial z} |\psi|^2 d\tau \tag{1.7}$$

where $E_z = \partial V/\partial z$ is the potential gradient perpendicular to the surface, and ψ is the wave function of the surface band [22]. Since the E_z value becomes maximum around the nucleus, the α_R value becomes large when the electron wave function of surface band is concentrated around the nucleus. Moreover, since the potential around the nucleus is nearly anti-symmetric along the z-axis, it is required that $|\psi|^2$ has to be also asymmetric with respect to the z-axis when α_R becomes large in Eq. (1.7). Nagano et al. performed first-principles band structure calculations at various surface conditions, and argued that the size of the Rashba spin splitting highly depends on the asymmetry of the wave function at the heavy nucleus around the surface [22]. This indicates that the size of the band splitting by the Rashba effect is affected not only by the spin-orbit interaction, but also by the distortion of the wave function along the surface vertical direction owing to the structure and chemical bonding characteristics.

Until know, various systems, such as the H or Li adsorbed W(110) [23–25], the group-V semimetals and their alloy surfaces [26–31], as well as the heavy-atom adsorbed semiconductor surfaces [32–36], are reported to have a Rashba effect, and intensive researches are on going.

8 1 Introduction

1.2.3 Group-V Semimetal Bismuth

Bismuth crystallizes with rhombohedral (or hexagonal) symmetry in a structure which is typical for the group-V semimetals (Fig. 1.5a), and it is the heaviest among non-radioactive elements. As shown in Fig. 1.5b, c, bulk Bi is known as a

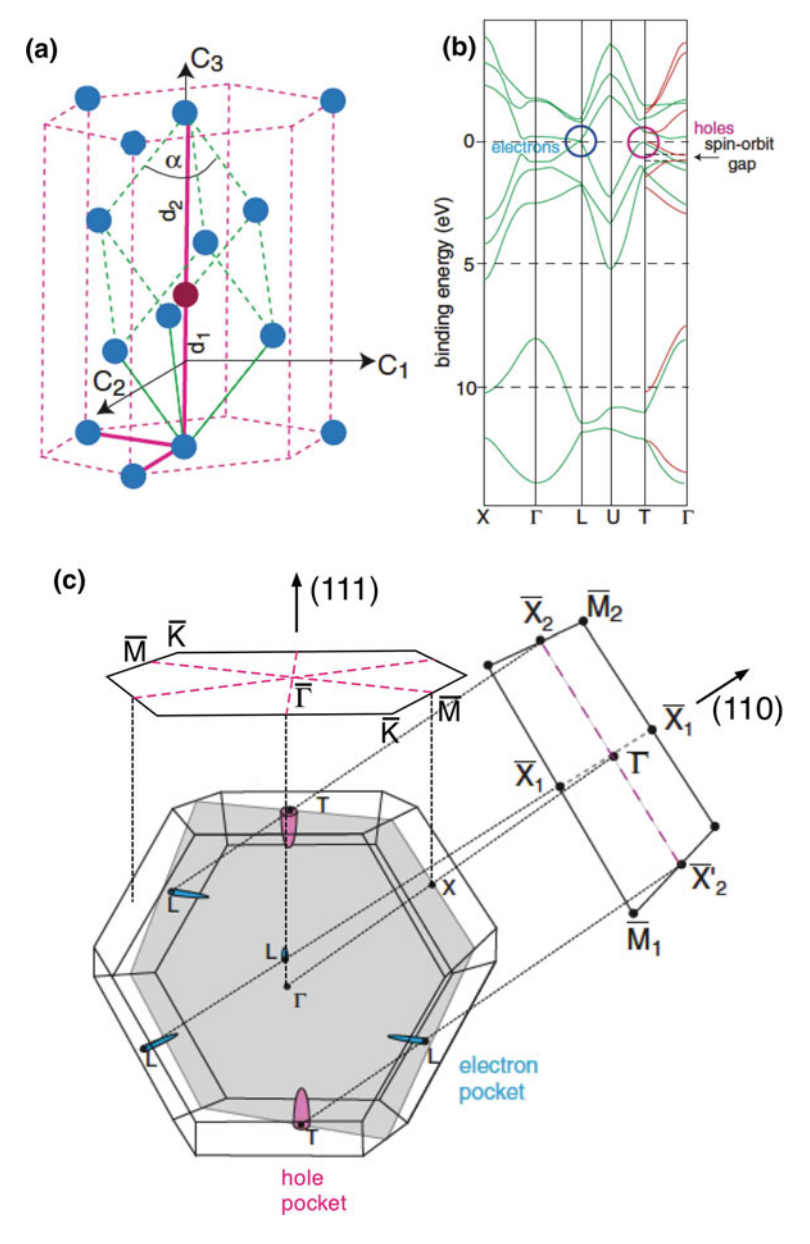


Fig. 1.5 a Bulk structure of Bi showing the rhombohedral and hexagonal unit cell. b Bulk band structure, and c Bulk brillouin zone and its projection onto the (111) and (110) surface in Bi [37]

1.2 Background 9

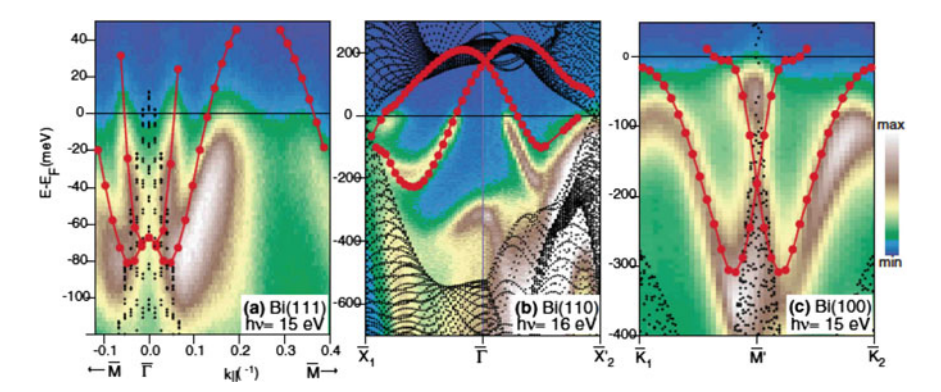
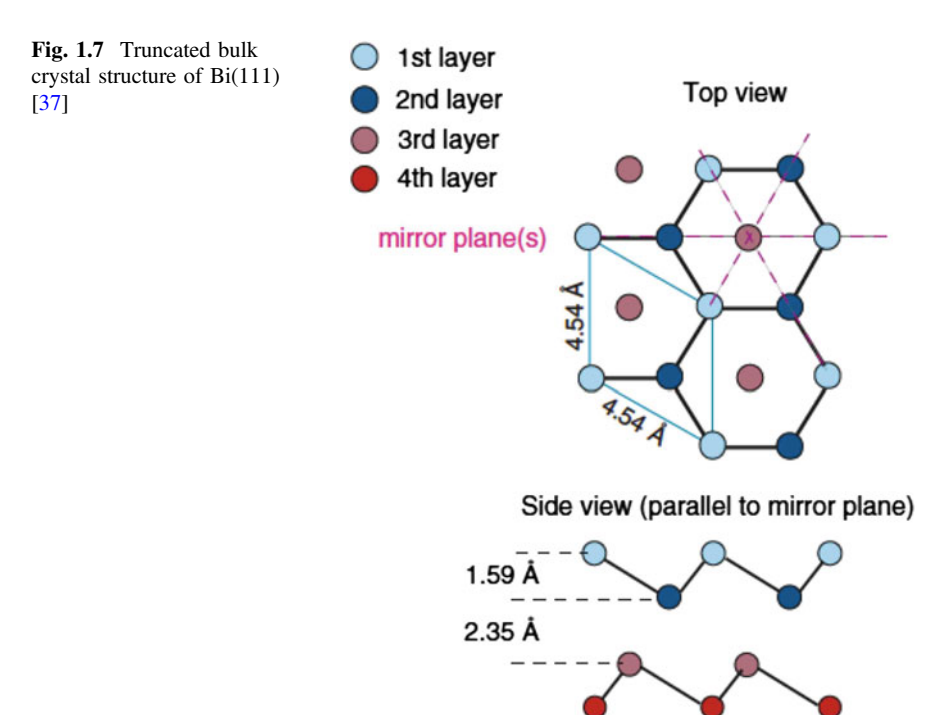


Fig. 1.6 Calculated and measured electronic structure in the vicinity of two high symmetry points on three different surface orientations in Bi [29]

semimetal which contains a hole (electron) pocket at the T (L) point [37]. The Rashba effect of Bi was reported for the first time by Ast and Höchst in 2001 [28]. They observed the existence of several complicated band structures within the bulkband projection gap in Bi(111). Koroteev et al. have concluded in 2004 that such band structures originate from the Rashba effect, since the band calculation which takes into account the spin-orbit interaction reproduces the ARPES measurement fairly well (Fig. 1.6) [29]. Bi has sizable Rashba splitting ($\alpha_R \sim 0.56 \text{ eVÅ}$) compared to other samples as reported in previous works, thus the details and the origin of Rashba effect are intensively studied so far [38–42]. In the following, the case of Bi thin film are briefly explained. Figure 1.7 shows a view showing the crystal structure in the (111) plane for bulk Bi, and it constructs hexagonal lattice in a direction perpendicular to the rhombohedral [111] axis with puckered bilayer (BL) structure [37]. Thin films are often used to obtain high-quality surface states. Details of the thin-film growth process is shown in Fig. 1.8a, which is reported in previous works such as scanning tunneling microscope (STM) and low-energy electron diffraction (LEED) [43, 44]. It is possible to fabricate the Bi thin film by a epitaxial growth on the Si(111) clean surface although the lattice constant is very different between Bi (4.538 Å) and Si (5.430 Å), due to the existence of disordered layer called "wetting-layer" between Bi and Si substrate. At the initial stage, Bi grows in the form of tiny islands with a random crystal orientation. With increasing deposition time, it transforms into a single crystal thin film (more than 8.4 monolayer). As shown in Fig. 1.8b, the structural transition from {012} direction to (111) direction suddenly takes place upon Bi deposition.

There are several unexplained phenomena in the Rashba effect of Bi. In the film, an electronic states originating from the bulk Bi are quantized and they are connected to the surface bands continuously. Thus, it has been suggested that the surface state of Bi is not a simple Rashba type [41]. So it would be necessary to take into account the relationship between bulk and surface states. Furthermore, it is expected from the theoretical calculations that the band dispersion dramatically changes depending on

10 1 Introduction



the thickness of the bilayer in ultrathin film case (< 6 BL) (note that the 1 BL film is theoretically predicted to be a two-dimensional topological insulator [45, 46]). It is also worthwhile to mention that a giant Rashba effect is reported on Bi-adsorbed Ag (111), which is 5 times larger ($\alpha_R \sim 3.05 \text{ eV}\text{Å}$) than the bulk Bi [30].

As mentioned above, the spin structure of Bi is discussed only qualitatively with a simple two-dimensional free electron model, while the Rashba effect of Bi has been reported in various examples like a simple bulk crystal, a film, and alloys. The essential factor responsible for this problem is the insufficient energy and momentum resolutions of the spin-resolved photoemission spectrometer which hinders to observe accurately the small band splitting. In addition to the low-efficiency nature of the spin-resolved ARPES, the surface state would not survive long because of the contamination of the surface due to adsorbed gas. These experimental obstacles have inhibited the detailed elucidation of the characteristics of the Rashba effect in Bi.

1.3 Purpose of the Present Research

Elucidation of the electron spin is very important to understand physical property in solid state and its surface as well as the possible applications to spintronic devices. Development of high-resolution spin-resolved photoemission spectrometer which

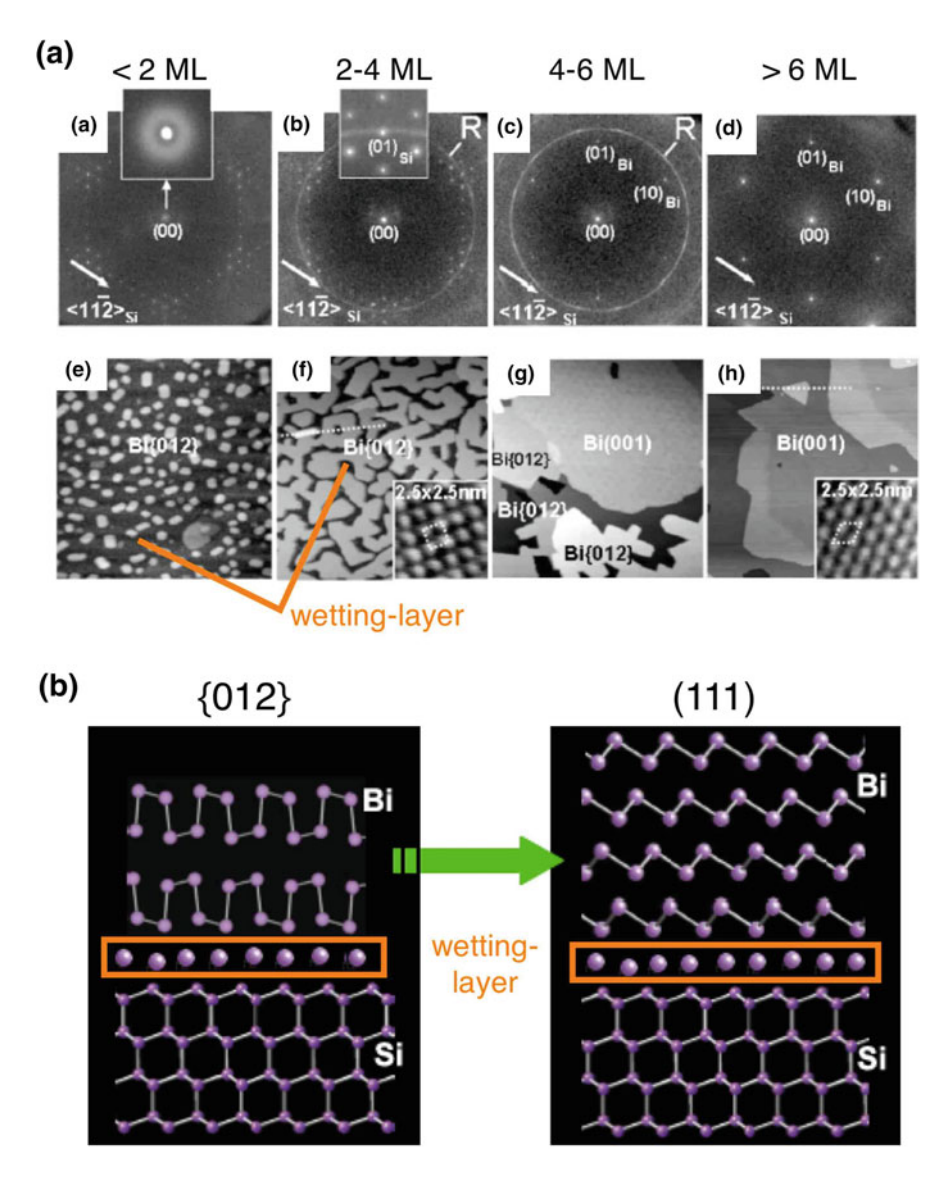


Fig. 1.8 a Thickness-dependence of spot-profile-analyzing-LEED pattern (*top*) and STM image (*bottom*) [43]. b Schematic illustration of the transformed structure in growth process of Bi thin film [44]

can determine all the key parameters of electrons (*i.e.*, energy, momentum, and spin) is expected to play a crucial role for the advancement of these studies. Furthermore, by high-resolution measurements, we will be able to discuss the spin-related physical phenomena not only qualitatively but also quantitatively, which would certainly lead to the deeper understanding of the condensed matter physics.

12 1 Introduction

First purpose of this study is to develop high-resolution spin-resolved ARPES spectrometer equipped with a highly efficient mini Mott detector. By utilizing the spectrometer, we have directly determined the electronic structure of Bi thin film to elucidate the details of the Rashba effect. In Chap. 2, the theory of photoemission spectroscopy and spin detection method will be mainly explained. Especially, the former focus on angle-resolved photoemission spectroscopy (ARPES), and the latter focus on the Mott detector. In Chap. 3, the detail of the high-resolution spin-resolved photoemission spectrometer constructed by this study and the results of experiments for system evaluation will be described. In Chaps. 4 and 5, the Rashba effect of Bi thin film grown on the Si substrate will be described. Anisotropic Rashba effect from momentum-dependent measurement and the interface Rashba effect between metal-semiconductor from thickness-dependent spin-resolved ARPES measurements will be discussed in Chaps. 4 and 5, respectively. In Chap. 6, the summary of this thesis will be provided.

References

- 1. J.G. Bednorz, K.A. Müller, Z. Phys. B Condens. Matter 64, 189 (1986)
- S. Hüfner (ed.), Very High Resolution Photoelectron Spectroscopy (Springer, Heidelberg, 2007)
- 3. P. Grünberg, R. Schreiber, Y. Pang, M.B. Brodsky, H. Sowers, Phys. Rev. Lett. 57, 2442 (1986)
- 4. M.N. Baibich, J.M. Broto, A. Fert, F. Nguyen Van Dau, F. Petroff, P. Eitenne, G. Creuzet, A. Friedrich, J. Chazelas, Phys. Rev. Lett. **61**, 2472 (1988)
- 5. T. Miyazaki, N. Tezuka, J. Magn. Magn. Mater. 139, 231 (1995)
- 6. J.S. Moodera, L.R. Kinder, T.M. Wong, R. Meservey, Phys. Rev. Lett. 74, 3273 (1995)
- 7. J. Inoue, H. Itoh, Spintronics -Basic Edition (Kyoritsu Shuppan, Japan, 2010) (in Japanese)
- 8. Y.A. Bychkov, E.I. Rashba, J. Phys. C. 17, 6039 (1984)
- 9. P.D. Johnson, Rep. Prog. Phys. 60, 1217 (1997)
- 10. E. Kisker, K. Schröder, W. Gudat, M. Campagna, Phys. Rev. B 31, 329 (1985)
- K. Ono, A. Kakizaki, K. Tanaka, K. Shimada, Y. Saitoh, T. Sendohda, Solid State Commun. 107, 153 (1998)
- 12. T. Kinoshita, Jpn. Soc. Synchrotron Radiat. Res. 7, 1 (1994) (in Japanese)
- 13. G.-C. Wang, R.J. Celotta, D.T. Pierce, Phys. Rev. B 23, 1761 (1981)
- 14. J. Unguris, D.T. Pierce, R.J. Celotta, Rev. Sci. Instrum. 57, 1314 (1986)
- 15. D. Tillmann, R. Thiel, E. Kisker, Z. Phys. B Condens. Matter 77, 1 (1989)
- 16. R. Bertacco, M. Merano, F. Ciccacci, Appl. Phys. Lett. 72, 2050 (1998)
- 17. Y. Ishida, H. Kanto, A. Kikkawa, Y. Taguchi, Y. Ito, Y. Ota, K. Okazaki, W. Malaeb, M. Mulazzi, M. Okawa, S. Watanabe, C.-T. Chen, M. Kim, C. Bell, Y. Kozuka, H.Y. Hwang, Y. Tokura, S. Shin, Phys. Rev. Lett. 107, 077601 (2011)
- 18. T. Kawagoe, J. Surf. Sci. Soc. Jpn. 26, 40 (2005). (in Japanese)
- 19. S. LaShell, B.A. McDougall, E. Jensen, Phys. Rev. Lett. 77, 3419 (1996)
- 20. G. Nicolay, F. Reinert, S. Hüfner, P. Blaha, Phys. Rev. B 65, 033407 (2001)
- M. Hoesch, M. Muntwiler, V.N. Petrov, M. Hengsberger, L. Patthey, M. Shi, M. Falub, T. Greber, J. Osterwalder, Phys. Rev. B 69, 241401(R) (2004)
- M. Nagano, A. Kodama, T. Shishidou, T. Oguchi, J. Phys.: Condens. Matter 21, 064239 (2009)
- 23. E. Rotenberg, S.D. Kevan, Phys. Rev. Lett. 80, 2995 (1998)

References 13

- 24. E. Rotenberg, J.W. Chung, S.D. Kevan, Phys. Rev. Lett. 82, 4066 (1999)
- 25. M. Hochstrasser, J.G. Tobin, E. Rotenberg, S.D. Kevan, Phys. Rev. Lett. 89, 216802 (2002)
- K. Sugawara, T. Sato, S. Souma, T. Takahashi, M. Arai, T. Sasaki, Phys. Rev. Lett. 96, 046411 (2006)
- T. Kadono, K. Miyamoto, R. Nishimura, K. Kanomaru, S. Qiao, K. Shimada, H. Namatame,
 A. Kimura, M. Taniguchi, Appl. Phys. Lett. 93, 252107 (2008)
- 28. C.R. Ast, H. Höchst, Phys. Rev. Lett. 87, 177602 (2001)
- Y.M. Koroteev, G. Bihlmayer, J.E. Gayone, E.V. Chulkov, S. Blügel, P.M. Echenique, Ph Hofmann, Phys. Rev. Lett. 93, 046403 (2004)
- C.R. Ast, J. Henk, A. Ernst, L. Moreschini, M.C. Falub, D. Pacilé, P. Bruno, K. Kern, M. Grioni, Phys. Rev. Lett. 98, 186807 (2007)
- 31. F. Meier, H. Dil, J. Lobo-Checa, L. Patthey, J. Osterwalder, Phys. Rev. B 77, 165431 (2008)
- 32. I. Gierz, T. Suzuki, E. Frantzeskakis, S. Pons, S. Ostanin, A. Ernst, J. Henk, M. Grioni, K. Kern, C.R. Ast, Phys. Rev. Lett. 103, 046803 (2009)
- K. Sakamoto, H. Kakuta, K. Sugawara, K. Miyamoto, A. Kimura, T. Kuzumaki, N. Ueno, E. Annese, J. Fujii, A. Kodama, T. Shishidou, H. Namatame, M. Taniguchi, T. Sato, T. Takahashi, T. Oguchi, Phys. Rev. Lett. 103, 156801 (2009)
- 34. E. Frantzeskakis, S. Pons, M. Grioni, Phys. Rev. B 82, 085440 (2010)
- K. Sakamoto, T. Oda, A. Kimura, K. Miyamoto, M. Tsujikawa, A. Imai, N. Ueno, H. Namatame, M. Taniguchi, P.E.J. Eriksson, R.I.G. Uhrberg, Phys. Rev. Lett. 102, 096805 (2009)
- 36. K. Yaji, Y. Ohtsubo, S. Hatta, H. Okuyama, K. Miyamoto, T. Okuda, A. Kimura, H. Namatame, M. Taniguchi, T. Aruga, Nat. Commun. 1, 17 (2010)
- 37. Ph Hofmann, Prog. Surf. Sci. 81, 191 (2006)
- 38. T. Hirahara, T. Nagao, I. Matsuda, G. Bihlmayer, E.V. Chulkov, Y.M. Koroteev, P.M. Echenique, M. Saito, S. Hasegawa, Phys. Rev. Lett. **97**, 146803 (2006)
- T. Hirahara, T. Nagao, I. Matsuda, G. Bihlmayer, E.V. Chulkov, Y.M. Koroteev, S. Hasegawa, Phys. Rev. B 75, 035422 (2007)
- T. Hirahara, K. Miyamoto, I. Matsuda, T. Kadono, A. Kimura, T. Nagao, G. Bihlmayer, E.V. Chulkov, S. Qiao, K. Shimada, H. Namatame, M. Taniguchi, S. Hasegawa, Phys. Rev. B 76, 153305 (2007)
- T. Hirahara, K. Miyamoto, A. Kimura, Y. Niinuma, G. Bihlmayer, E.V. Chulkov, T. Nagao, I. Matsuda, S. Qiao, K. Shimada, H. Namatame, M. Taniguchi, S. Hasagawa, New J. Phys. 10, 083038 (2008)
- A. Kimura, E.E. Krasovskii, R. Nishimura, K. Miyamoto, T. Kadono, K. Kanomaru, E.V. Chulkov, G. Bihlmayer, K. Shimada, H. Namatame, M. Taniguchi, Phys. Rev. Lett. 105, 076804 (2010)
- 43. T. Nagao, J.T. Sadowski, M. Saito, S. Yaginuma, Y. Fujikawa, T. Kogure, T. Ohno, Y. Hasegawa, S. Hasegawa, T. Sakurai, Phys. Rev. Lett. 93, 105501 (2004)
- 44. T. Nagao, S. Yaginuma, J.T. Sadowski, M. Saito, Y. Fujikawa, T. Ohno, S. Hasegawa, T. Sakurai, J. Surf. Sci. Soc. Jpn. 26, 344 (2005) (in Japanese)
- 45. S. Murakami, Phys. Rev. Lett. 97, 236805 (2006)
- 46. Y.M. Koroteev, G. Bihlmayer, E.V. Chulkov, S. Blügel, Phys. Rev. B 77, 045428 (2008)

Chapter 2 Basic Principle of Photoemission Spectroscopy and Spin Detector

To understand and discuss the experimentally obtained photoemission data, it is important to understand the principle of an experimental method and an analysis of the data. In this chapter, the basic principle of photoemission spectroscopy and the spin detector is explained, by particularly emphasizing the angle-resolved photoemission spectroscopy technique and the Mott detector.

2.1 Photoemission Spectroscopy

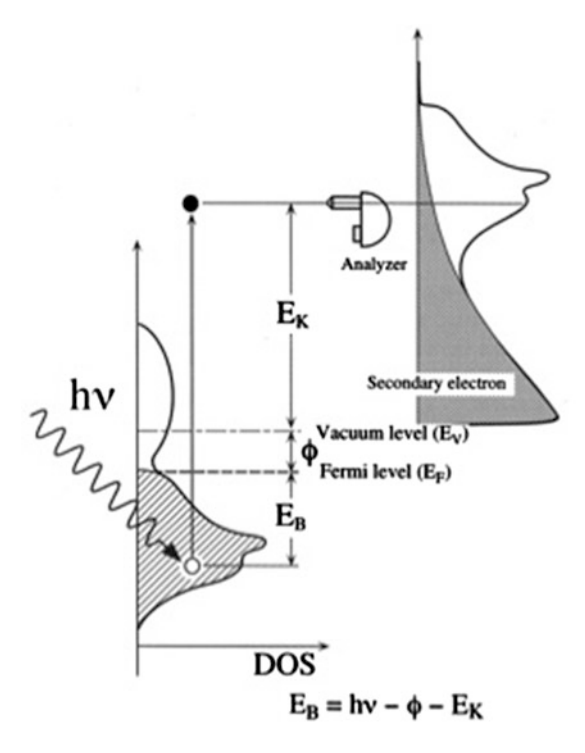
2.1.1 Principle of Photoemission Spectroscopy

Photoemission spectroscopy (PES) is a well-known technique which measures the electronic structure of a solid through the external photoelectric effect. With the types of the photon energies used for the PES measurements, the PES technique is roughly classified into two types; *i.e.*, X-ray PES (XPS) and ultraviolet PES (UPS). Recently, with the development of highly brilliant photon source in synchrotron radiation, the distinction between the XPS and UPS became unclear, thus they are rather identified by the energy region of interest, *i.e.* the core level or the valence band [1]. The PES technique is also classified into two categories; angle-integrated and angle-resolved mode. The former obtains the density of states and the later obtains the band dispersion [2]. For the PES measurement, photons excite electrons from the crystal surface by the external photoelectric effect. By fixing the energy of incident photons and observing the velocity (kinetic energy) of excited photoelectrons, it is possible to determine the density of states at a fixed binding energy of electrons in the material [1].

The principle of the PES technique is shown in Fig. 2.1. The electron is initially excited by absorbing a photon, in which energy conservation across the excitation is satisfied. From the observed photoelectron kinetic energy E_k ,

$$E_{\rm B} = hv - E_k - \phi \tag{2.1}$$

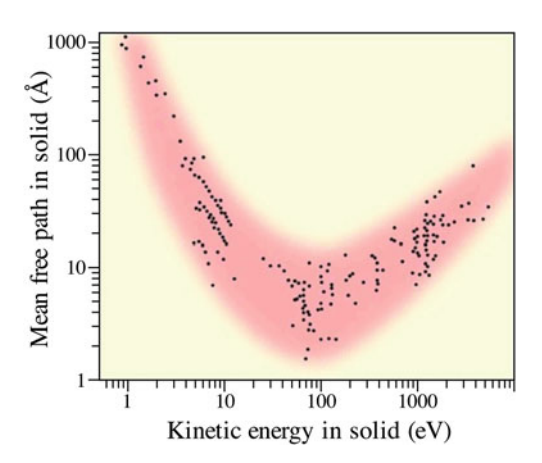
Fig. 2.1 Band structure of the sample is imaged by the excitation of electrons from the occupied states in the sample (*left*) with the photons of energy *hv*



where $E_{\rm B}$ is the binding energy of an electron, hv is the incident photon energy and ϕ is the work function. Since hv and ϕ are already-known value, we can determine $E_{\rm B}$ when E_k is identified experimentally.

The PES technique is inherently surface sensitive. Figure 2.2 shows a relationship between the escape depth and the kinetic energy of photoelectrons, called "universal curve" [3, 4]. Photoelectron escape depth varies according to the energy

Fig. 2.2 Escape depth of electrons as a function of electron kinetic energy in a solid [4]



of the photoelectrons, while it also depends on the dielectric function of the material. The escape depth of photoelectrons for the kinetic energy of 20–100 eV is only 5–10 Å. Therefore, a special attention is necessary for the surface condition of the sample.

2.1.2 Angle-Resolved Photoemission Spectroscopy

Angle-Resolved Photoemission Spectroscopy (ARPES) is a powerful and unique experimental technique to observe simultaneously energy and momentum, namely, the band dispersions. During the photoemission process, we consider the changes to the photoelectron's momentum (Fig. 2.3). In the ARPES, an initial momentum k is given by the emission polar angle θ (measured from the surface normal). The momentum of excited photoelectron in a crystal is expressed as the surface parallel component $\hbar k_{II}$ and the perpendicular component $\hbar k_{\perp}$. After photoelectron is emitted from the crystal to a vacuum, the momentum is expressed as the parallel $\hbar K_{II}$ and the perpendicular $\hbar K_{\perp}$ component, respectively. The momentum of exiting electrons from a sample is altered by the crystal potential at the surface. However the parallel component $\hbar k_{II}$ is conserved owing to the translation symmetry of the crystal surface.

$$\hbar k_{\parallel} = \hbar K_{\parallel} \tag{2.2}$$

On the other hand, the energy of photoelectron emitted to a vacuum is given by

$$E_k = \frac{(\hbar K)^2}{2m} \tag{2.3}$$

where m is a electron mass. From Eqs. (2.1), (2.2), (2.3),

$$k_{\parallel} = \frac{\sqrt{2m(hv - \phi - E_B)}}{\hbar} \sin \theta \tag{2.4}$$

When final state of electron is assumed as free electron, the perpendicular component k_{\perp} is expressed by Eq. (2.5), while it is not conserved.

$$k_{\perp} = \frac{\sqrt{2m(h\nu - \phi - E_B)\cos^2\theta + U_0}}{\hbar} \tag{2.5}$$

where U_0 is variable called "inner potential", typically it is defined as an energy of valence band bottom [5]. However, the k_{\perp} value has a finite width (Δk_{\perp}) because the escape depth of photoelectron Δ_z is very short. Form the uncertainty principle,

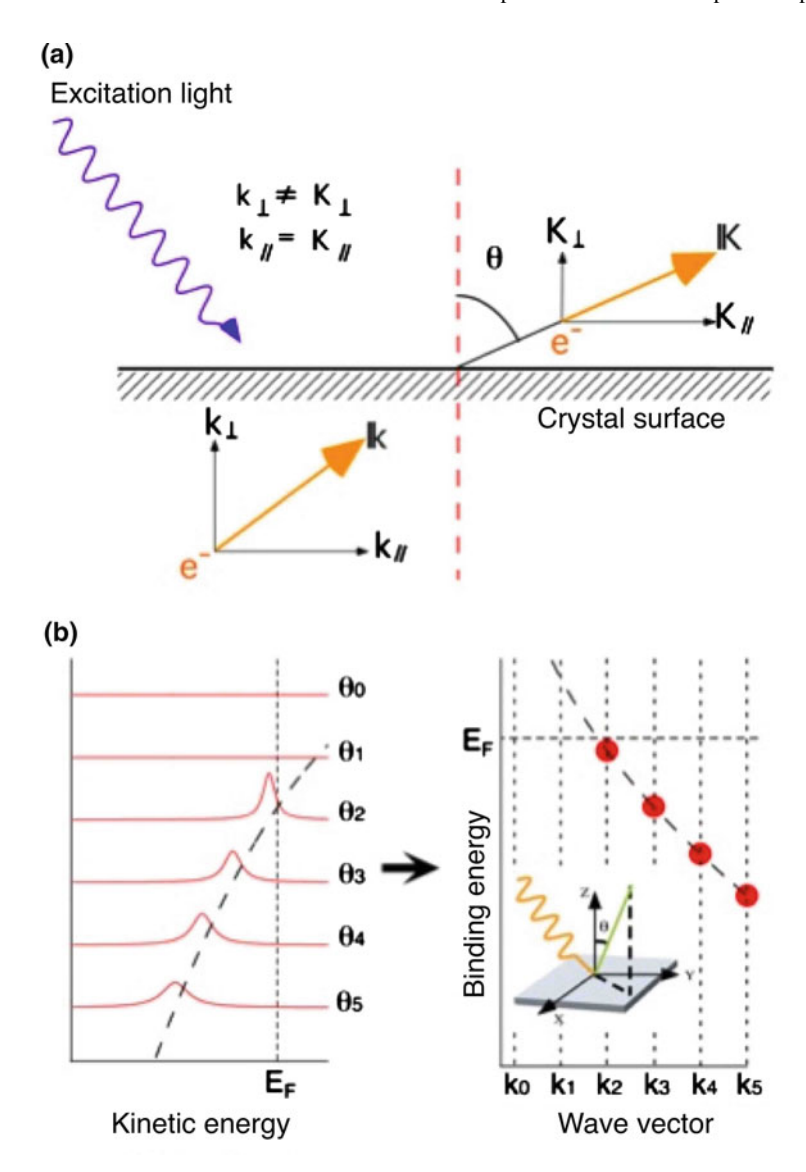


Fig. 2.3 a Momentum of electrons exited from the sample is altered by the crystal potential at the surface. While the parallel component $(k_{//})$ is conserved by the translation symmetry of crystal, the perpendicular component is not. **b** An example of a band map. The momentum (wave vector) corresponding to the measurement angle (θ) is transformed by an Eq. (2.4)

$$\Delta_z \cdot \Delta k_{\perp} \sim 1 \tag{2.6}$$

Due to the effect which is called "final-state broadening" [6], the K_{\perp} component in the final state also has a finite width.

In the case of a 2D state like the surface, the interface, and the layered materials such as graphene, it is possible to ignore k_{\perp} . Hence the band dispersion is simply determined experimentally from Eq. (2.4).

2.1.3 Photoemission Spectral Function

In this section, the meaning of the photoemission spectra more theoretically explained. When we do not take account into a lattice-relaxation and an electron correlation (electron-electron interaction), photoemission spectrum is expressed as the product of the initial-state (ψ_i) and final-state (ψ_f) electron wave functions. However, this picture is not completely valid where the many-body interaction exists. Photoemission spectrum is given by a spectral function which includes the many-body interaction and the final-state effect.

A photoemission or inverse photoemission spectral function at certain momentum k is given by

$$A(k,\omega) = A^{+}(k,\omega) + A^{-}(k,\omega) \tag{2.7}$$

$$A^{-}(k,\omega) = f(\omega)A(k,\omega) \tag{2.8}$$

$$A^{+}(k,\omega) = [1 - f(\omega)]A(k,\omega) \tag{2.9}$$

where $A^+(k, \omega)$ is the inverse photoemission spectral function, $A^-(k, \omega)$ is the photoemission spectral function, and $f(\omega)$ is the Fermi distribution function that represents the electron occupancy. By using the one-particle Green function $G(k, \omega)$, $A(k, \omega)$ is also given by

$$A(k,\omega) = -\frac{1}{\pi} \text{Im}G(k,\omega)$$
 (2.10)

where

$$G(k,\omega) = \sum_{f} \left| \left\langle \psi_{f}^{N-1} \middle| c_{k} \middle| \psi_{i}^{N} \right\rangle \right| \left[\frac{P}{\omega + E_{f}^{N-1} - E_{i}^{N}} - i\pi\delta(\omega + E_{f}^{N-1} - E_{i}^{N}) \right]$$

$$+ \sum_{f} \left| \left\langle \psi_{f}^{N+1} \middle| c_{k}^{+} \middle| \psi_{i}^{N} \right\rangle \right| \left[\frac{P}{\omega + E_{f}^{N-1} - E_{i}^{N}} - i\pi\delta(\omega + E_{f}^{N+1} - E_{i}^{N}) \right]$$

$$(2.11)$$

P is the Cauchy integral, ψ_i (ψ_f) and E_i (E_f) are wave function and intrinsic energy of the initial (final) state. c_k (c_k^+) is annihilation (creation) operator [6]. The former term of Eq. (2.11) corresponds to photoemission spectroscopy, and the later is to inverse photoemission spectroscopy. Thus, $A(k, \omega)$ is given by

$$A(k,\omega) = \sum_{f} \left| \left\langle \psi_{f}^{N-1} \middle| c_{k} \middle| \psi_{i}^{N} \right\rangle \right| \delta(\omega + E_{f}^{N-1} - E_{i}^{N})$$

$$+ \sum_{f} \left| \left\langle \psi_{f}^{N+1} \middle| c_{k}^{+} \middle| \psi_{i}^{N} \right\rangle \right| \delta(\omega + E_{f}^{N+1} - E_{i}^{N})$$

$$(2.12)$$

The former term of Eq. (2.12) corresponds to the photoemission spectral function, and the to the inverse photoemission spectral function. In the one-electron approximation without interaction, $G(k, \omega)$ and $A(k, \omega)$ is given by

$$G(k,\omega) = \frac{1}{\omega - \varepsilon_k^0 + i0^+} \tag{2.13}$$

$$A(k,\omega) = \delta(\omega - \varepsilon_k^0) \tag{2.14}$$

where ε_k^0 is the binding energy of the bare band.

Now we consider a case with interaction. Then $G(k, \omega)$ and $A(k, \omega)$ are given with the use of self-energy $\Sigma(k, \omega)$ by,

$$G(k,\omega) = \frac{1}{\omega - \varepsilon_k^0 - \Sigma(k,\omega)}$$
 (2.15)

$$A(k,\omega) = \frac{1}{\pi} \frac{-\text{Im}\Sigma(\mathbf{k},\omega)}{\left[\omega - \varepsilon_k^0 - \text{Re}\Sigma(\mathbf{k},\omega)\right]^2 + \left[\text{Im}\Sigma(\mathbf{k},\omega)\right]^2}$$
(2.16)

Equation (2.15) is called the Dyson equation. Re Σ and Im Σ satisfy the following conditions from the Kramers-Kronig relation.

$$\operatorname{Re}\Sigma(\mathbf{k},\omega) - \operatorname{Re}\Sigma(\mathbf{k},\mu) = \frac{1}{\pi} \operatorname{P} \int_{-\infty}^{\infty} \frac{\operatorname{Im}\Sigma(\mathbf{k},\omega') - \operatorname{Im}\Sigma(\mathbf{k},\infty)}{\omega - \omega'} d\omega' \qquad (2.17)$$

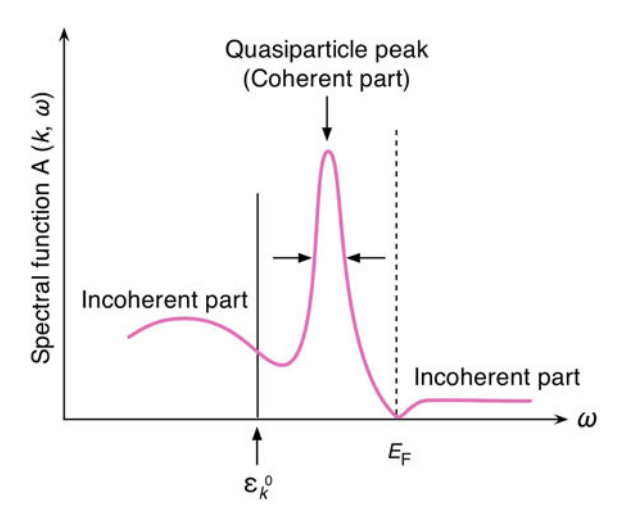
$$Im\Sigma(\mathbf{k},\omega) - Im\Sigma(\mathbf{k},\infty) = -\frac{1}{\pi}P\int_{-\infty}^{\infty} \frac{Re\Sigma(\mathbf{k},\omega') - Re\Sigma(\mathbf{k},\mu)}{\omega - \omega'} d\omega' \qquad (2.18)$$

Re Σ and Im Σ can be calculated when we know $G(k, \omega)$.

$$Im\Sigma(\mathbf{k},\omega) = \frac{ImG(\mathbf{k},\omega)}{ReG(\mathbf{k},\omega)^2 + ImG(\mathbf{k},\omega)^2}$$
(2.19)

$$\operatorname{Re}\Sigma(\mathbf{k},\omega) = \omega - \varepsilon_{\mathbf{k}}^{0} - \frac{\operatorname{Re}G(\mathbf{k},\omega)}{\operatorname{Re}G(\mathbf{k},\omega)^{2} + \operatorname{Im}G(\mathbf{k},\omega)^{2}}$$
(2.20)

Fig. 2.4 An example of a photoemission spectral function in a system with the strong many-body interactions [6]



From these equations, we enable to calculate self energy if we know the spectral function.

Lifetime of a quasi-particle is proportional to $|\text{Im}\Sigma(k,\omega)|^{-1}$, and a peak width of the quasi-particle is $2|\text{Im}\Sigma(k,\omega)|$. Re $\Sigma(k,\omega)$ corresponds to an energy shift from ε_k^0 , reflecting the interaction. A quasiparticle peak (coherent part) arises as a sharp peak, while broad incoherent part arises in an unoccupied state and in the higher E_B side than ε_k^0 (Fig. 2.4) [6].

2.1.4 Photoemission Spectral Intensity

The photoemission spectral intensity observed in the experiment is given by

$$I(k,\omega) = I_0(k) \sum_{\delta k} d\omega' A(k',\omega') f(\omega') R(\omega,\omega') + SOL + Background \qquad (2.21)$$

where

$$I_0(k) \propto \left| \left\langle \psi_f \middle| A \cdot p \middle| \psi_i \right\rangle \right|^2$$
 (2.22)

The I_0 depends on the polarization vector of incident light (A) and the momentum vector (p), and the atomic orbital component. The R, which is the resolution function of the spectrometer, is the Gaussian. The SOL (second order light) is a background by an incident light and the Background includes other effects such as secondary electrons.

From Eq. (2.22), it is expected that $I_0(k)$ has a maximum value when the broadening of the initial state $\Delta \psi_i$ is close to de Broglie wave length of the final

state ψ_f . Namely, there is a most effective energy of the incident light to excite an electron in a specific orbital. The photo-excitation cross-section can be calculated for the respective atomic orbital [7]. In general, electrons in the *s*- or *p*-orbital show high cross-section with low-energy photons, while the *d*- or *f*-electrons show the same with high-energy photons.

2.1.5 Energy Distribution Curve and Momentum Distribution Curve

In the ARPES measurements, as displayed in Fig. 2.5, the spectra measured at a constant k is called the energy distribution curve (EDC) and the spectra measured at a constant energy is called the momentum distribution curve (MDC). Photoemission spectrum is usually referred to the EDC. The EDC is more suitable to show the "light" band dispersion, while the MDC is more effective for the "heavy" band. Peaks in the EDCs or the MDCs correspond to the high photoelectron density, indicating the center of an electron band. Other information, such as a quasiparticle lifetime, can be extracted by observing the width of these peaks [8].

2.2 Spin Detector

2.2.1 Various Spin Detectors

The nature of electrons in solids is described by three quantum parameters, energy, momentum, and spin. The first experiment which observed the electron spin was reported by Stern and Gerlach in 1922 [9]. Figure 2.6 is a schematic view of this experiment. A silver (Ag) atom is heated and vaporized in an oven, and then it becomes atomic beam and is evaporated to a photographic plate through a slit. In this experiment, atomic beam of Ag passes and split by gradient magnetic field applied from a slit to a photographic plate. From this result, Uhlenbeck and Goudsmit proposed that an electron has angular momentum corresponding to "spin" and magnetic momentum [10]. Now we commonly understood that such a phenomenon is caused by the Ag 5s electron spin. However, it is unrealistic to observe electron spin by this method because electron is much lighter than Ag atom and the resultant split size is expected to be fairly small.

For the electron spin-polarization measurements, many kinds of spin detector have been developed utilizing various spin-dependent scattering processes as shown in Table 2.1 [11–15]. Common characteristics of these detectors are to use heavy elements as a target like gold (Au) and tungsten (W) owing to their large spin-orbit coupling (SOC). Recently, spin detector which utilizes the spin exchange interaction has been also developed [14]. Among them, the Mott detector is one of

2.2 Spin Detector 23

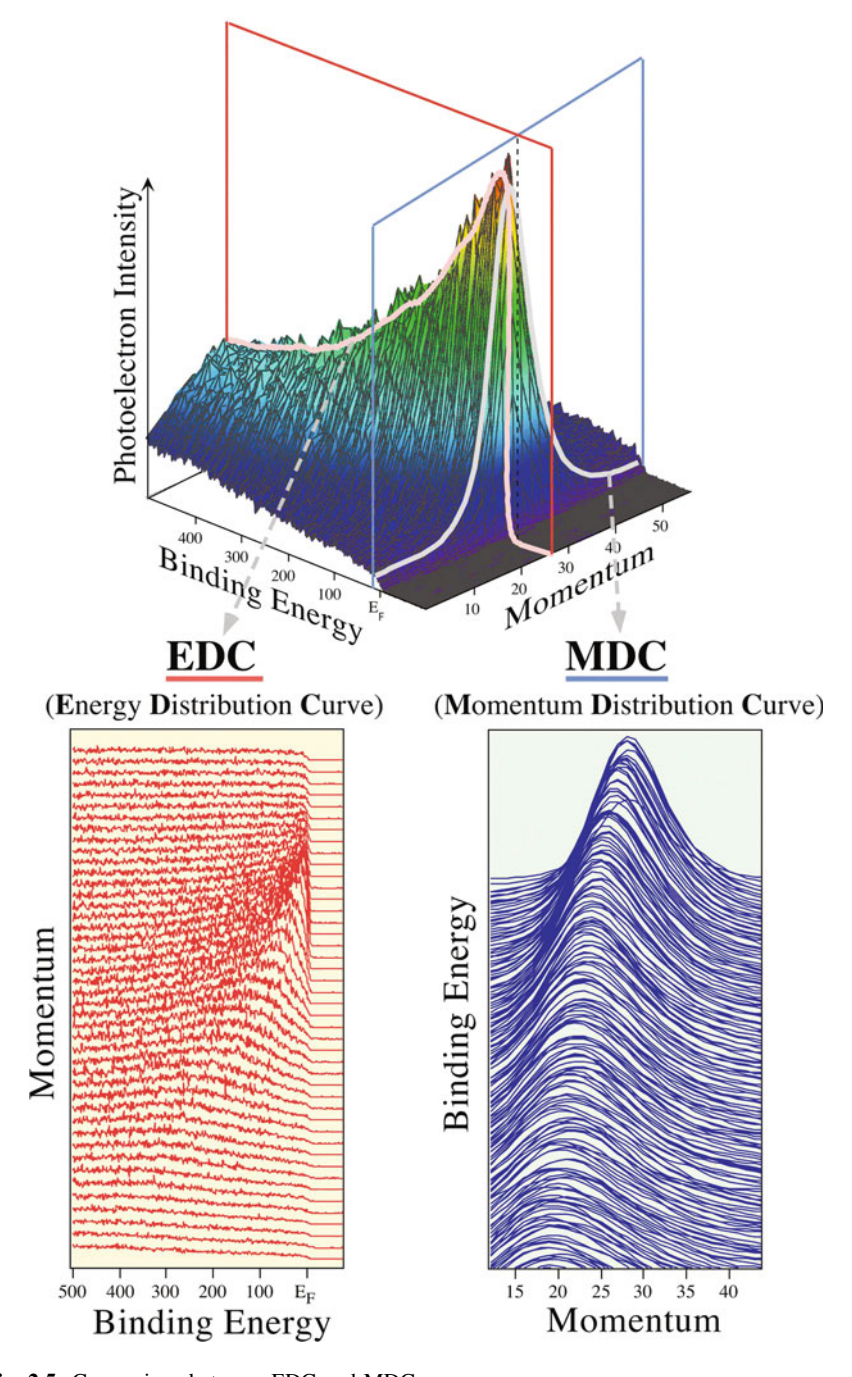
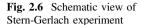


Fig. 2.5 Comparison between EDC and MDC



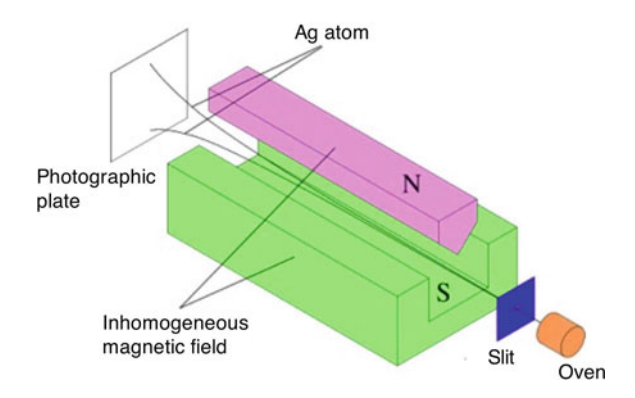


Table 2.1 Comparison of the performance of various spin detectors [15]

Method	Interaction	Operation voltage	$S_{ m eff}$	Figure of merit	Target
Mott	Spin-orbit	20-100 kV	0.1-0.2	$1-5 \times 10^{-4}$	Au thin film
SPLEED	Spin-orbit	150 V	0.2–0.3	$1-2 \times 10^{-4}$	W single crystal
Diffuse scattering	Spin-orbit	150 V	~0.2	~1 × 10 ⁻⁴	Au thin film
VLEED	Spin- exchange	6–10 V	0.3-0.4	~10 ⁻²	Fe single crystal

the most widely used detector to measure the electron spin polarization due to its high stability and usefulness of the self-calibration. From the next section, principle of the Mott scattering and the detail of Mott detector are explained.

2.2.2 Principle of the Mott Scattering

The asymmetry of the spin polarization in the Mott scattering arises from SOC between the electron and the nucleus. Mott spin detector is based on this scattering [16]. As seen in Fig. 2.7, in the electron's rest frame, the positively charged nucleus looks to move toward the electron and, an effective magnetic field **B** is generated at the position of the electron. The magnetic field is given by

$$\mathbf{B} = -\frac{1}{c}\mathbf{v} \times \mathbf{E} = \frac{Ze}{cr^3}\mathbf{r} \times \mathbf{v} = \frac{Ze}{mcr^3}\mathbf{L}$$
 (2.23)

where \mathbf{v} is the velocity of the electron, \mathbf{r} is the distance between the electron and the nucleus, and Z is the atomic number of the nucleus. The electron orbital angular momentum about the nucleus \mathbf{L} and electric field of the nucleus \mathbf{E} are given by

2.2 Spin Detector 25

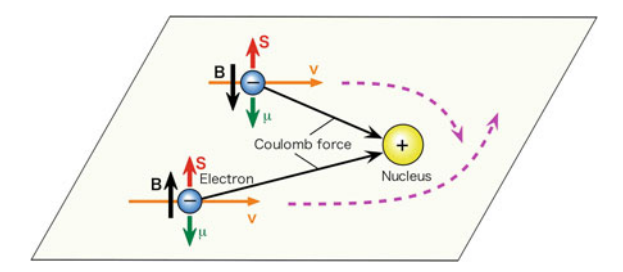


Fig. 2.7 Electron experiences electric and magnetic fields by a scattering to a nucleus (Mott scattering)

$$\mathbf{E} = (Ze/r^3)\mathbf{r} \tag{2.24}$$

$$\mathbf{L} = m\mathbf{r} \times \mathbf{v} \tag{2.25}$$

The magnetic moment of an electron μ_e is defined as

$$\mu_e = -\frac{g_s e}{2mc} \mathbf{S} \tag{2.26}$$

where g_s is the gyromagnetic ratio ($g_s \approx 2$), it means that; when an electron has upward spin perpendicular to orbital plane, μ_e points to the downward direction. Here we take into account spin precession (Thomas precession 1/2), and the potential by the SOC (V_{LS}) that arises from the interaction between the electron magnetic moment and the **B** of the nucleus, as given by

$$V_{LS} = -\mu_e \cdot \mathbf{B} = \frac{Ze^2}{2m^2c^2r^3} \mathbf{L} \cdot \mathbf{S}$$
 (2.27)

The sign of the V_{LS} is determined by whether **S** and **L** are aligned or anti-aligned. The SOC becomes the maximum when the spin direction is perpendicular to the orbital plane. It is indicated that the upward (downward) spin is easy to be scattered toward right (left) way. In addition, V_{LS} becomes larger as the Z is larger and the \mathbf{v} is faster, so that the Mott detector makes electron collide to a target prepared by heavy element such as Au at high speed (voltage).

Now we consider the system in Fig. 2.8a. The electron beam strikes toward the Au target by high voltage. Depending on the scattering angle, the differential scattering cross section $\sigma(\theta)$ also shows an asymmetry. $\sigma(\theta)$ is given by

$$\sigma(\theta) = I_0(\theta) \cdot (1 + S(\theta)\mathbf{P} \cdot \hat{\mathbf{n}}) \tag{2.28}$$

where $I_0(\theta)$ is the differential scattering cross section for unpolarized electron beam, \mathbf{P} is the polarization vector of incident electrons, $\hat{\mathbf{n}}$ is the unit vector normal to a scattering plane, and $S(\theta)$ is the Sherman function. From Eq. (2.28), we notice that a vertical spin component to a scattering plane only contributes to the $\sigma(\theta)$. Scattering

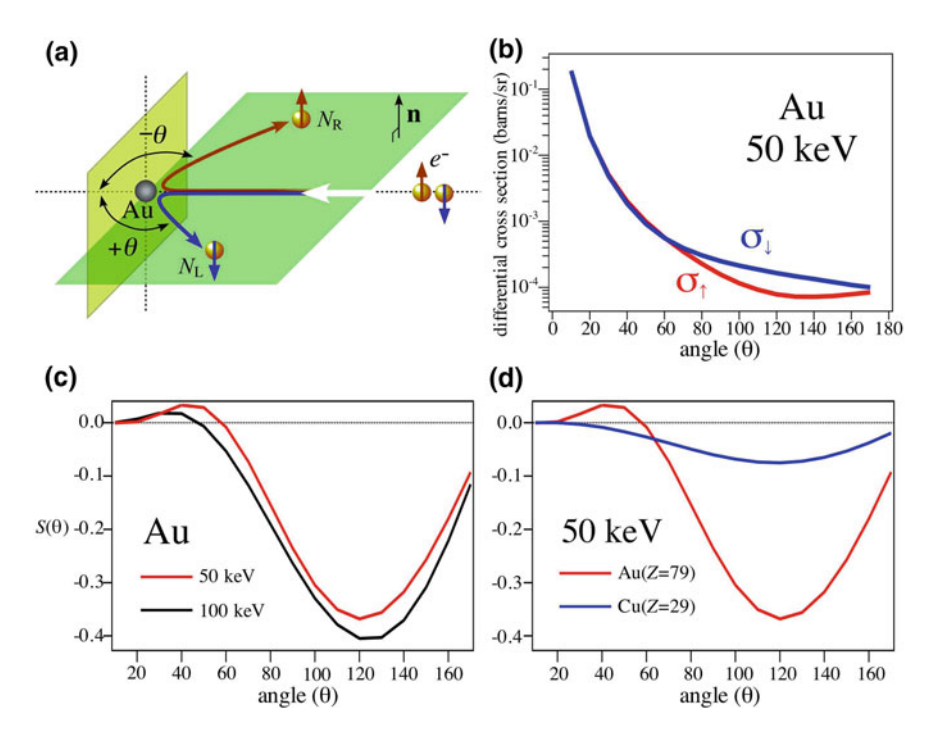


Fig. 2.8 a Schematic view of electron spin scattering for heavy atom. **b** Cross section for gold as a function of back scattering angle at 50 keV. **c**, **d** Energy and atomic-number dependence of the Sherman function, respectively [17]

asymmetry $A(\theta)$ is defined by the differential scattering cross section for up and down spin $\sigma_{\uparrow}(\theta)$, $\sigma_{\downarrow}(\theta)$

$$A(\theta) \equiv \frac{\sigma_{\uparrow}(\theta) - \sigma_{\downarrow}(\theta)}{\sigma_{\uparrow}(\theta) + \sigma_{\downarrow}(\theta)} = PS(\theta)$$
 (2.29)

As shown in Fig. 2.8b, $\sigma(\theta)$ and $A(\theta)$ depend on the scattering angle and they have a maximum value at $\theta = 120^{\circ}$ [17]. $S(\theta)$ also becomes the maximum at $\theta = 120^{\circ}$, however the $S(\theta)$ value strongly depends on the incident electron energy and Z of the target material (Fig. 2.8c, d). The absolute value of $S(\theta)$ becomes larger as Z becomes larger and \mathbf{v} becomes faster. Since the up spin is scattered toward the $-\theta$ side and the down spin toward the $+\theta$ side, we need a pair electron detectors which are set to $\pm 120^{\circ}$.

2.2.3 Mott Detector

A traditional Mott detector utilizes incident electron with high energy (~100 keV) to enhance the scattering asymmetry. One needs a special attention to suppress the discharge in high-voltage electrode for the Mott detector, thus the large-detector

2.2 Spin Detector 27

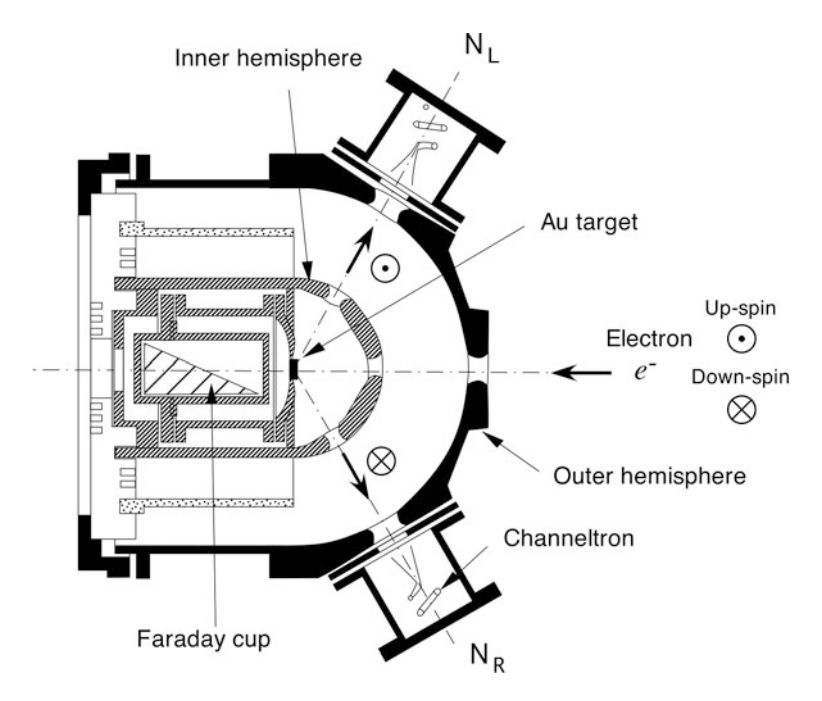


Fig. 2.9 Schematic view of mini Mott detector based on retarding-potential design

size is (over 1 m³) a demerit. However, recently, the mini Mott detector with "retarding -potential type" has been developed; this can be operated at relatively low energy (~30 keV) [18]. Figure 2.9 shows a schematic view of the retardingpotential-type mini Mott detector. Now the size of the Mott detector is much smaller than the previous case. In this type of Mott detector, energy-reduced electrons by a multiple scattering are excluded by the retarding potential. A Mott detector has usually two-pair electron detectors such as channeltron in order to observe spin for two axes. Lens elements are built into the Mott detector to make a focused electron beam onto the target. Au (Z = 79) is widely used as a target material owing to its high stability. Recently thorium (Z = 90) is also used [19], while it requires scrupulous attention for handling due to its radioactive nature. Thin film target is used to reduce multiple and plural scatterings which reduce the scattering asymmetry. Taking account into the multiple scatterings, the Sherman function is replaced with an "effective Sherman function S_{eff} ". The value of S_{eff} is specific to each instrument. The absolute value of $S_{eff}(\theta)$ is smaller than the $S(\theta)$, while the variation of $S_{eff}(\theta)$ near 120° is milder than $S(\theta)$.

The efficiency of the Mott detector is defined as

$$\varepsilon = \left| S_{eff}(\theta) \right|^2 \cdot I/I_0 \tag{2.30}$$

where ε is called as a figure of merit, I_0 is the number of electrons entering the Mott detector and I is the total number of the scattered electrons measured by the left and right electron detectors. A typical value of $S_{eff}(\theta)$ for various mini Mott detectors with the electron acceleration energy of 25 kV is ~0.1 [19], thus the typical figure of merit is the order of 10^{-4} . The efficiency of detecting the spin polarization is three orders-of-magnitude lower than that of the regular (non-spin-resolved) measurement. So for high efficiency, electron detectors are centered at $\pm 120^{\circ}$ and enables to collect electrons with a finite acceptance angle.

2.2.4 Derivation Method of Spin Polarization Spectrum

In this sectionan actu, al procedure to obtain the spin-polarized spectra from the experimentally obtained spectra is explained.

Figure 2.10 illustrates the procedure for this. When the EDC has spin polarization like Fig. 2.10a, we can obtain the "total" spectrum by spin-integrated AR-PES. Here the number of up or down spins is expressed as N_{\uparrow} , N_{\downarrow} respectively, and the "total" spectrum is given by $N_{\uparrow} + N_{\downarrow}$. As displayed in Fig. 2.10b, the spin polarization P range is $-1 \le P \le 1$. $N_{\rm L}$ ($N_{\rm R}$) denotes the intensity measured in the left (right) channeltron detector at angle θ ($-\theta$). From Eq. (2.28), $N_{\rm L}$ and $N_{\rm R}$ are given by

$$N_{\rm L} = N_{\uparrow} I_0(\theta) (1 + S_{\rm eff}(\theta)) + N_{\downarrow} I_0(\theta) (1 - S_{\rm eff}(\theta))$$
 (2.31)

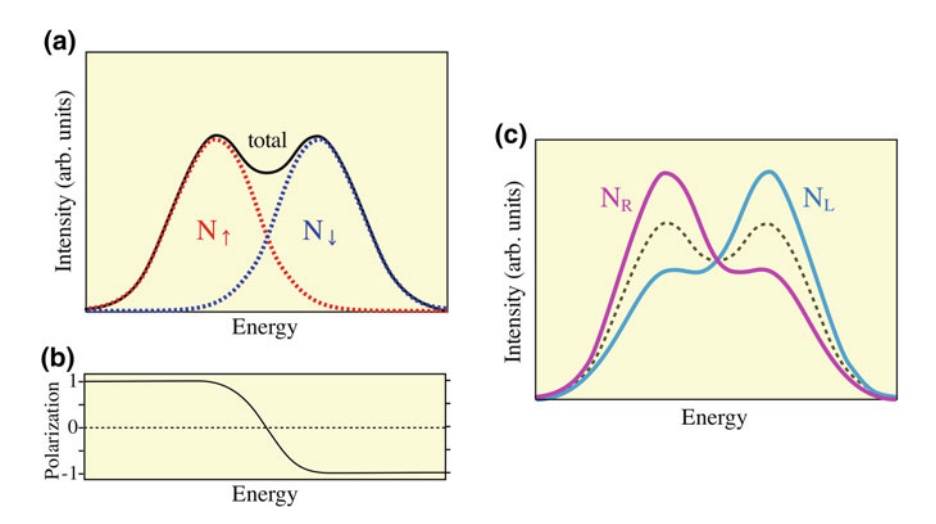


Fig. 2.10 Procedure to extract the spin-resolved spectra from the experimentally observed data. \mathbf{a} N_{\uparrow} and N_{\downarrow} are intrinsic spin-polarized spectra. A *solid line* (Total) is spin-integrated photoemission spectrum. \mathbf{b} Spin polarization as a function of energy in \mathbf{a} . \mathbf{c} Spectra for $S_{eff} = 0.3$ determined from the spin-resolved photoemission experiment

2.2 Spin Detector 29

$$N_{\rm R} = N_{\uparrow} I_0(\theta) (1 - S_{\rm eff}(\theta)) + N_{\downarrow} I_0(\theta) (1 + S_{\rm eff}(\theta))$$
 (2.32)

This represents the experimentally obtained spin-resolved spectra (Fig. 2.10c). Next, we calculate " $N_L + N_R$ " and " $N_L - N_R$ " using Eqs. (2.31) and (2.32).

$$N_{\rm L} + N_{\rm R} = 2I_0(\theta)(N_{\uparrow} + N_{\downarrow})$$
 (2.33)

$$N_{\rm L} - N_{\rm R} = 2I_0(\theta)S_{\rm eff}(\theta)(N_{\uparrow} - N_{\perp}) \tag{2.34}$$

Here, P and $A(\theta)$ are defined as

$$P = \frac{N_{\uparrow} - N_{\downarrow}}{N_{\uparrow} + N_{\downarrow}} \tag{2.35}$$

$$A(\theta) = \frac{N_L - N_R}{N_L + N_R} \tag{2.36}$$

From Eqs. (2.29), (2.35), and (2.36),

$$A(\theta) = \frac{N_L - N_R}{N_L + N_R} = \frac{N_{\uparrow} - N_{\downarrow}}{N_{\uparrow} + N_{\downarrow}} S_{eff}(\theta) \equiv P S_{eff}(\theta)$$
 (2.37)

Finally we deform the Eq. (2.37) to calculate N_{\uparrow} and N_{\downarrow} .

$$1 + P = 1 + \frac{A(\theta)}{S_{eff}(\theta)} = \frac{2N_{\uparrow}}{N_{\uparrow} + N_{\downarrow}}$$

$$1 - P = 1 - \frac{A(\theta)}{S_{eff}(\theta)} = \frac{2N_{\uparrow}}{N_{\uparrow} + N_{\downarrow}}$$
(2.38)

$$N_{\uparrow} = \frac{1}{2} (1 + P)(N_{\uparrow} + N_{\downarrow})$$

$$N_{\downarrow} = \frac{1}{2} (1 - P)(N_{\uparrow} + N_{\downarrow})$$
(2.39)

Thus if the $S_{eff}(\theta)$ is known and the asymmetry is measured, the polarization can be calculated; therefore it is essential to determine an accurate S_{eff} value of the Mott detector prior to the experiment.

References

- T. Takahashi, Photoemission solid-state physics, *Kotai Butsuri*. Solid States Phys. 29, 189 (1994) (in Japanese)
- 2. F.J. Himpsel, Adv. Phys. 32, 1 (1983)

- 3. E.W. Plummer, W. Eberhardt, *Angle-resolved photoemission as a tool for the study of surface* (Advance in Chemical Physics, 2007)
- 4. M.P. Seah, W.A. Dench, Surf. Interface Anal. 1, 2 (1979)
- 5. P.J. Feibelman, D.E. Eastman, Phys. Rev. B 10, 4932 (1974)
- 6. M. Date (Ed.), Kyosokan-Denshi-kei Strongly Correlated Electron System. (Kodansha, 1997) (in Japanese)
- 7. J.J. Yeh, I. Lindau, At. Data Nucl. Data Tables 32, 1 (1985)
- 8. T. Valla, A.V. Fedorov, P.D. Johnson, B.O. Wells, S.L. Hulbert, Q. Li, G.D. Gu, N. Koshizuka, Science 285, 2110 (1999)
- 9. W. Gerlach, O. Stern, Zeitschrift für Physik 9, 353 (1922)
- 10. G.E. Uhlenbeck, S. Goudsmit, Phy. Rev. 34, 145 (1929)
- 11. K. Soda, Nihon Butsuri Gakkai-shi (Butsuri) 45, 804 (1990) (in Japanese)
- 12. G.C. Wang, R.J. Celotta, D.T. Pierce, Phys. Rev. B 23, 1761 (1981)
- 13. J. Ungris, D.T. Pierce, R.J. Celotta, Rev. Sci. Instrum. 57, 1314 (1986)
- T. Okuda, Y. Takeichi, Y. Maeda, A. Harasawa, I. Matsuda, Rev. Sci. Instrum. 79, 123117 (2008)
- T. Okuda, Y. Takaichi, A. Kakizaki, Nihon Butsuri Gakkai-shi (Butsuri) 65, 849 (2010) (in Japanese)
- 16. N.F. Mott, H.S.W. Massey, The Theory of Atomic Collision 3rd edition (Oxford, 1987)
- 17. S.R. Lin, Phy. Rev. 133, A965 (1964)
- 18. F.C. Tang, X. Zhang, F.B. Dunning, K. Walters, Rev. Sci. Instrum. **59**, 504 (1988)
- 19. G.C. Burnett, T.J. Monroe, F.B. Dunning, Rev. Sci. Instrum. 65, 1893 (1994)

Chapter 3 Development of High Resolution Spin-Resolved Photoemission Spectrometer

This chapter describes an ultrahigh-resolution spin-resolved photoemission spectrometer with a highly efficient mini Mott detector. To determine the three-dimensional spin-polarization, an electron deflector has been situated between the analyzer and the Mott detector. The spectrometer achieves the energy resolutions of 0.9 and 8 meV for non-spin-resolved and spin-resolved modes, respectively. The performance of the spectrometer is demonstrated by the observation of a clear Rashba splitting of the surface states in bismuth.

3.1 Outline

Figure 3.1 shows a schematic diagram of the ultrahigh-resolution spin-resolved ARPES spectrometer which has been developed in this study [1]. This spectrometer consists of mainly four parts, (1) a photoemission measurement system including a large (40 cm in diameter) hemispherical electron-energy analyzer and an ultrahighvacuum measurement chamber, (2) a spin-detection system based on a mini Mott detector, (3) an intense xenon/helium plasma discharge lamp, and (4) a surface chamber to prepare the thin-film samples. The photoemission measurement system, which is the most important part of the whole system, consists of a hemispherical analyzer, measurement chamber, a vacuum chamber and a preparation chamber. A mini Mott detector used as a detector of an electron spin is developed to achieve high efficiency, and it is connected to the analyzer through the electron deflector. The Mott detector observes the spin polarization of essentially two independent axes by using 4 channeltrons, enabling us to determine the in-plane and out-of-plane spin component. Moreover, the spectrometer is capable of performing a regular (spinintegrated) ARPES measurement by using a multi-channel plate (MCP). The optical system consists of helium (He) and xenon (Xe) [2] plasma discharge lamps and a monochromator with the gratings, in which we can select photon energy if necessary. In the surface chamber, we can prepare the bismuth (Bi) thin-film samples by the evaporation of Bi on semiconducting substrate, and we can also check the quality of the sample by using low-energy electron diffraction (LEED). The samples are

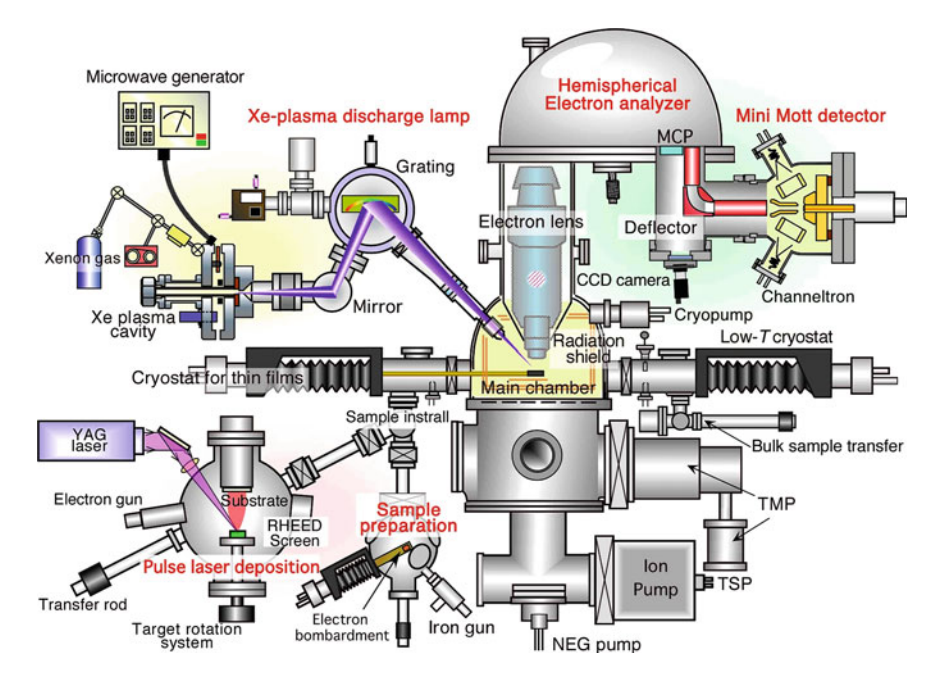


Fig. 3.1 Schematic view of high-resolution spin-resolved photoemission spectrometer

transferred in situ to the ARPES measurement chamber, which is particularly useful for elucidating the electronic states of the samples containing a clean well-ordered surfaces required for the accurate ARPES measurements.

This chapter describes the details of the each components of the spin-resolved ARPES spectrometer. In addition, the details of the measurements are also provided to evaluate the performance of the spectrometer.

3.2 Design and Construction

3.2.1 Mott Detector

A Mott detector is probably a most widely used spin detector. However, in the case of spin-resolved ARPES, it is inherently difficult to achieve a high-energy resolution because the efficiency for detecting the spin-polarization by utilizing the backscattering electrons is typically three orders-of-magnitude lower than that of non-spin-resolved measurement. To solve this problem and to perform high-resolution spin-resolved ARPES measurements, we have designed and developed a highly efficient mini Mott detector.

Figure 3.2 shows the detail of the mini Mott detector. Figure 3.2a shows the schematic picture of the mini Mott detector in which the detector parts inside the

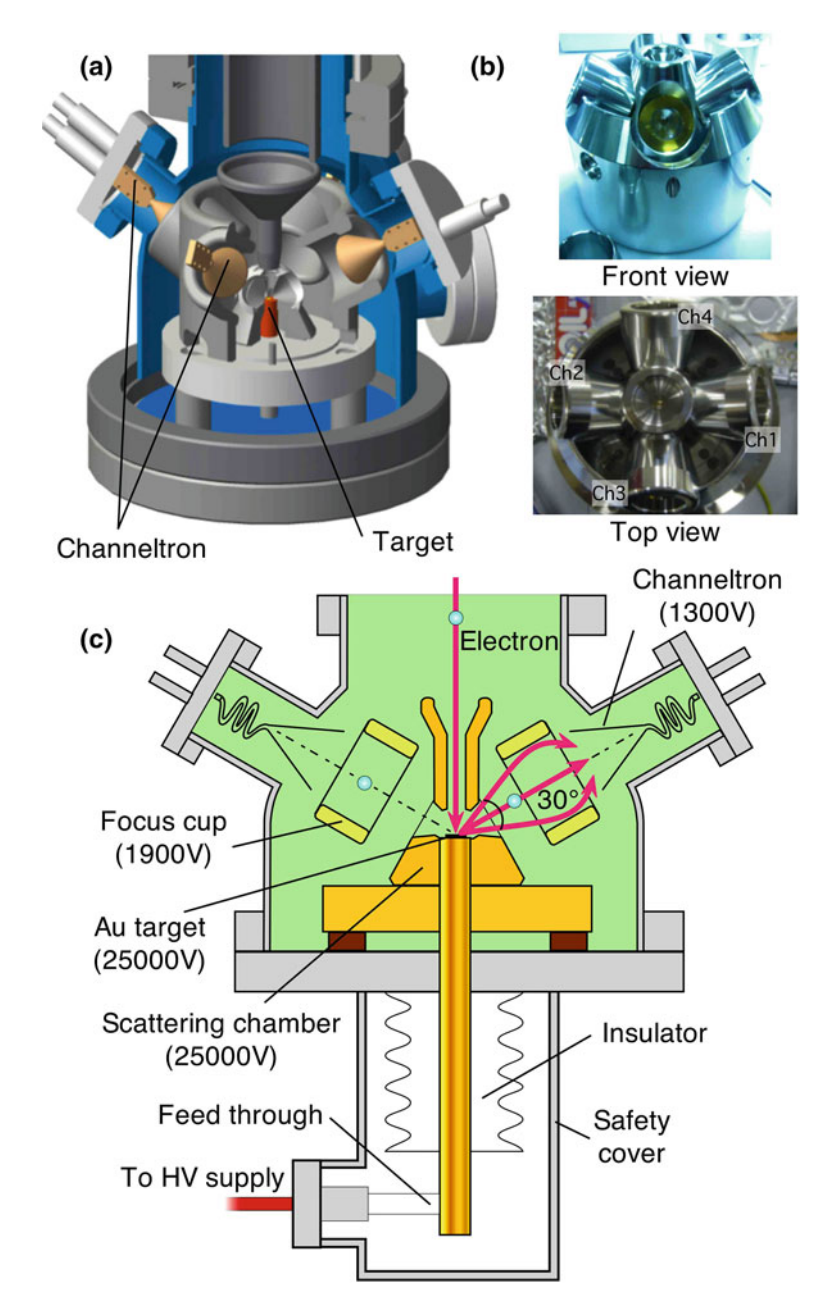


Fig. 3.2 New Mott-detector. a Three-dimensional illustration. b Photographs of the scattering chamber viewed from the side and top. c Two-dimensional schematic view

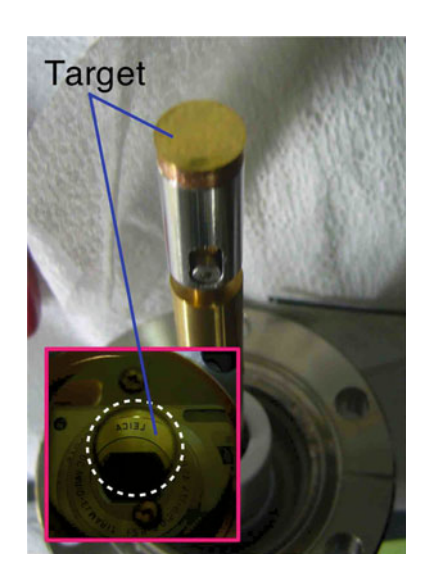
vacuum chamber are highlighted for a better understanding of its structure. We adapted a retarding-potential-type design. The merit of this design is that the energy-reduced electrons due to inelastic scatterings can be well excluded. The detector has made to be in compact size $(30 \times 30 \times 50 \text{ cm}^3)$, taking into account the compatibility with the analyzer. In this detector, electrons are accelerated toward a target at the center of the Mott detector to 25 keV, then scattered and detected by channeltrons. As shown in Fig. 3.2b, all the vacuum components of the detector have a rounded shape to eliminate the discharge caused by strong local electric field. Aluminum was chosen as a material since it is craft-friendly. Figure 3.2c is a 2D schematic view of the Mott detector. A gold film is used as a scattering target, because it has a large atomic-number (Z) value of 79 and also because it is stabile and manageable. An important point to increase the efficiency of the Mott detector is that an acceptance angle to collect backscattered electrons is enlarged compared to previous Mott detectors. The effective Sherman function S_{eff} and the scattering cross section have a maximum value at around ±120°. If the acceptance angle of electrons increases with respect to $\pm 120^{\circ}$, the S_{eff} value reduces only slightly while the photoelectron intensity increases dramatically. Thus, it is possible to adjust the width of the acceptance angle within the range that the effective S_{eff} value does not reduce so much. We have set the acceptance angle of the detector to be $\pm 15^{\circ}$ with respect to 120°. The electrons scattered from the target first pass the focus cup electrode and are finally detected by four channeltrons. A retarding potential is applied between the focus cup and the channeltrons. When the retarding potential is set at high voltage, number of detected electron decreases and thus the efficiency goes down. Taking into account these issues, the voltage of the focus cup and the channeltrons are set at 1,900 and 1,300 V, respectively.

Another important issue to increase the efficiency of the Mott detector is the increase in the number of backscattered electrons. In this regard, in order to decrease the probability of the multiple scatterings caused by the roughness of the target, the target surface has been polished and flattened. Specifically, the target was first prepared with oxygen-free copper (ϕ 10 mm). Then, the surface was mechanically polished by hands by using silicon carbide abrasive (#3,000, #6,000) and diamond pastes (ϕ 3, 1, ½ µm). Polished target was cleaned in alcohol, then covered with evaporated gold, and finally inserted into the Mott detector (Fig. 3.3). The scattering efficiency of the Mott detector is as high as 2.3×10^{-2} , which is one order of magnitude higher than the previous detector.

3.2.2 Improvement of Hemispherical Analyzer System

This section describes the hemispherical electron analyzer which enables both spinintegrated and spin-resolved ARPES measurements. In most of previous spinresolved ARPES spectrometers, the spin detector is mounted at the exit of the analyzer instead of the MCP. This design loses the advantage of the multichannel detection with MCP to achieve the high-speed and high-resolution measurement.

Fig. 3.3 Photographs of a gold target. Surface was polished to show a mirror-like reflection



However, when we discuss the complicated spin structure which strongly depends on k such as a surface states of the Rashba system and topological insulators, it is of particular importance to perform the spin-resolved ARPES measurements by specifying the absolute k location in the k space.

As seen in Fig. 3.4, the analyzer consists of inner- and outer hemisphere, in which positive and negative electric potential are applied to the inner (radius R_1) and the outer (radius R_2) hemisphere, respectively. When electrons enter the slit of the analyzer, they are divided by an electrostatic force from the charged hemispheres, depending upon their energy and momentum. Electrons with higher energies are collected closer to the outer hemisphere, likewise electrons with low energies are collected towards the inside. If electron's energy is too high and low, they are absorbed to hemisphere and cannot reach the exit of the analyzer. The energy resolution $\Delta E_{\rm instrument}$ (eV) at a hemispherical analyzer is given by

$$\Delta E_{\rm instrument} = \frac{E_p W}{2R} \tag{3.1}$$

where W (mm) is the width of the entrance slit and E_p (eV) is energy through the center between inner- and outer- hemisphere (pass energy) [3, 4]. We are able to select the W, E_p values from 0.1, 0.2, 0.4, 0.8, 1.6, 3.2 mm, and 1, 2, 5, 10, 20, 50 eV, respectively in our analyzer. The average radius $R = R_1 + R_2$ (mm) of the analyzer is 200 mm and this R is believed to be an nearly optimized value by taking into account the accuracy of the manufacture.

At the and of the analyzer, the electrons reach the MCP, phosphor screen, and charge coupled device (CCD) camera. In the conventional ARPES spectrometer, the MCP is placed just at the center between the inner- and outer-sphere electrodes to detect simultaneously the energy and the angle of photoelectrons as shown in

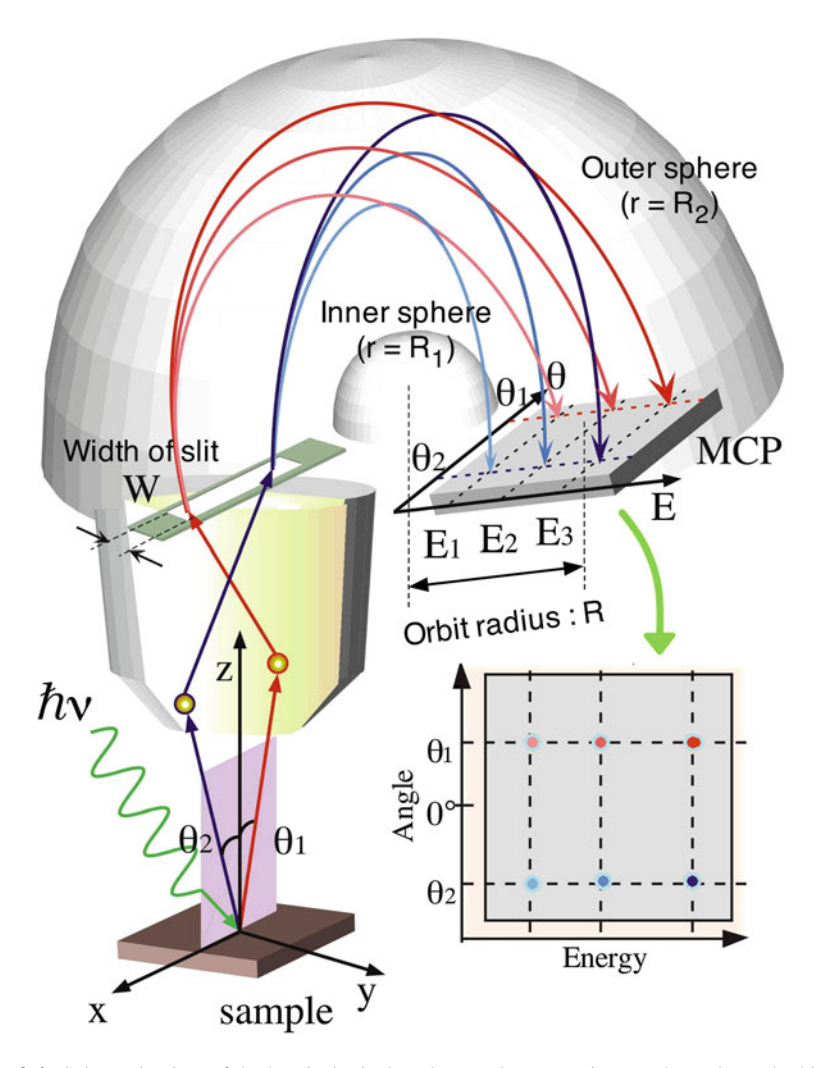


Fig. 3.4 Schematic view of the hemispherical analyzer. Electron trajectory depends on the kinetic energy and momentum of emitted electrons

Fig. 3.5a [5]. When we observe three quantum parameters of electron, namely, energy, momentum, and spin, it is requested that the MCP and the Mott detector are connected with each other in the vacuum. Therefore the MCP has been shifted toward the inner sphere by 1 cm and a hole (4 mm in diameter) has been made between the MCP and the outer sphere (Fig. 3.5a, b). Figure 3.5c shows a photograph of the electron-detection system. The system enables to determine the band dispersion and the spin polarization by the MCP and the Mott detector, respectively. Electrons arrived at the MCP are accelerated by large electric field (typically 1,900 V) so that they hit the walls of the channels, causing a cascade of secondary

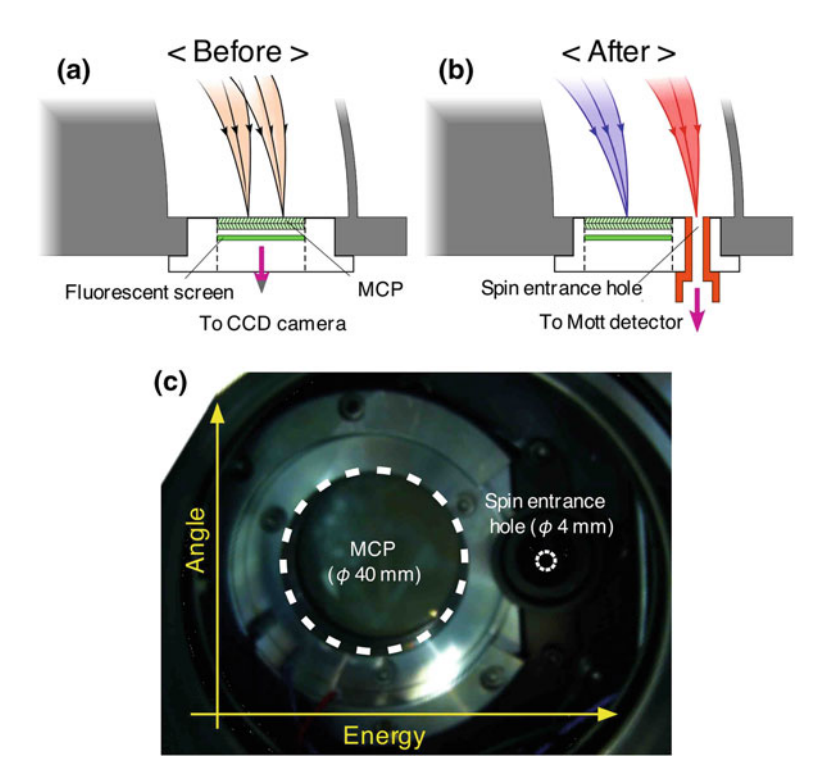


Fig. 3.5 Comparison of the electron-detection system a Before and b After the improvement. c Actual electron-detection system after the improvement

electrons. In this way, the MCP acts as an amplifier, greatly increasing the number of electrons in each channel. Upon exiting the MCP, electrons are further accelerated by a voltage of 3,800 V, before hitting a phosphor screen. This screen reacts to the high-energy electrons, emitting a flash of photons for each collision. Finally, a CCD camera aligned in series with the MCP and phosphor system captures these photons. The image of electron distribution on the MCP is captured by a CCD camera about 35 cm away from the MCP to avoid the physical interference with the deflector.

3.2.3 Deflector

Since the Mott detector observes the spin polarization for essentially two independent axes, we can determine the polarization of only x and y axes if we install the Mott detector just at the exit hole of the analyzer. To observe the spin polarization for all the three axes, the 90° deflector is set between the exit hole of the analyzer and the Mott detector (Fig. 3.6). In this geometry, we can detect in-plane

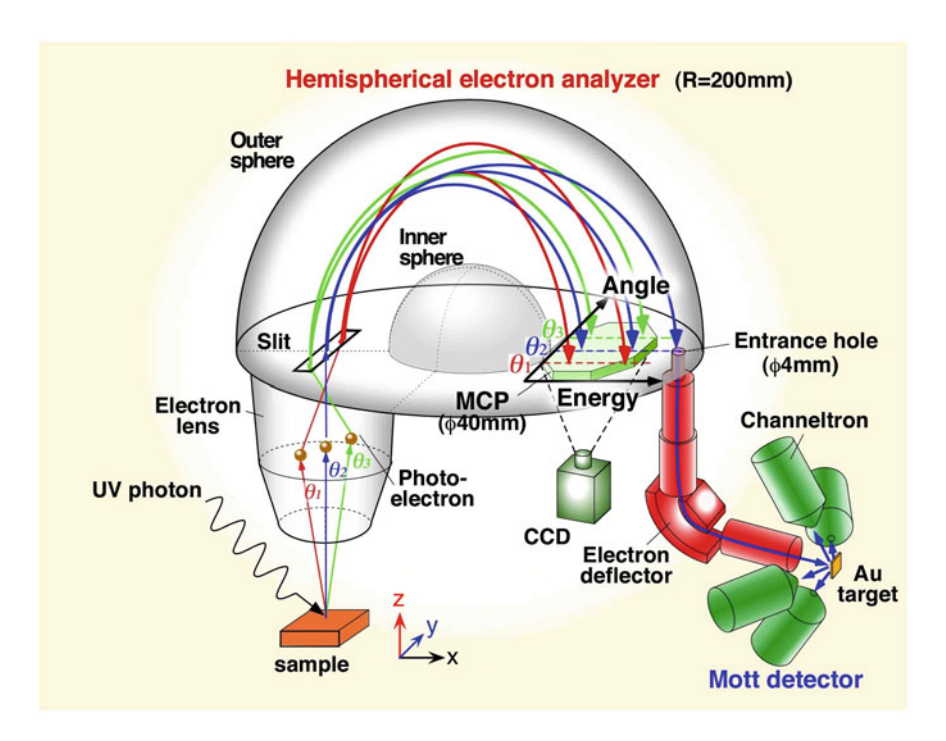


Fig. 3.6 Spin-detection system

(y) spin component by right-and left-side channeltrons and out-of-plane (z) spin component by up-and down-side channeltrons. In addition, by rotating the sample in the x-y plane by 90°, we can determine the three-dimensional spin polarization.

Figure 3.7 shows a schematic view of the deflector. This deflector consists of a few lens elements. Since the electron trajectory is controlled by electric field, the direction of spin is not affected by this electric field. When electron collides and are scattered by the gold target, a most important issue is that the electron beam should converge onto a narrow region of the target. We first examined whether or not electrons really reaches the target position, by a channeltron replaced with the target. Next, the condition of the collision was verified by the fluorescence plate. The size of the electron beam on the target has been estimated to be ϕ 1 mm (inset to Fig. 3.7). We have also confirmed that the electron deflector keeps ~100 % transmittance.

One also needs to aware of an influence of magnetic field during the spin detection. If residual magnetic field exists in the spectrometer, the intrinsic information of spin may be lost. A photoemission spectrometer typically blocks the geomagnetism (\sim 500 mG) by the Mu-metal shield. However, this shield cannot be inserted into the deflector and the Mott detector in our case, because of their complex and compact structure. On the other hand, the time interval for electrons to pass from the entrance hole to the target is estimated to be \sim 10⁻⁷ s, leading to our

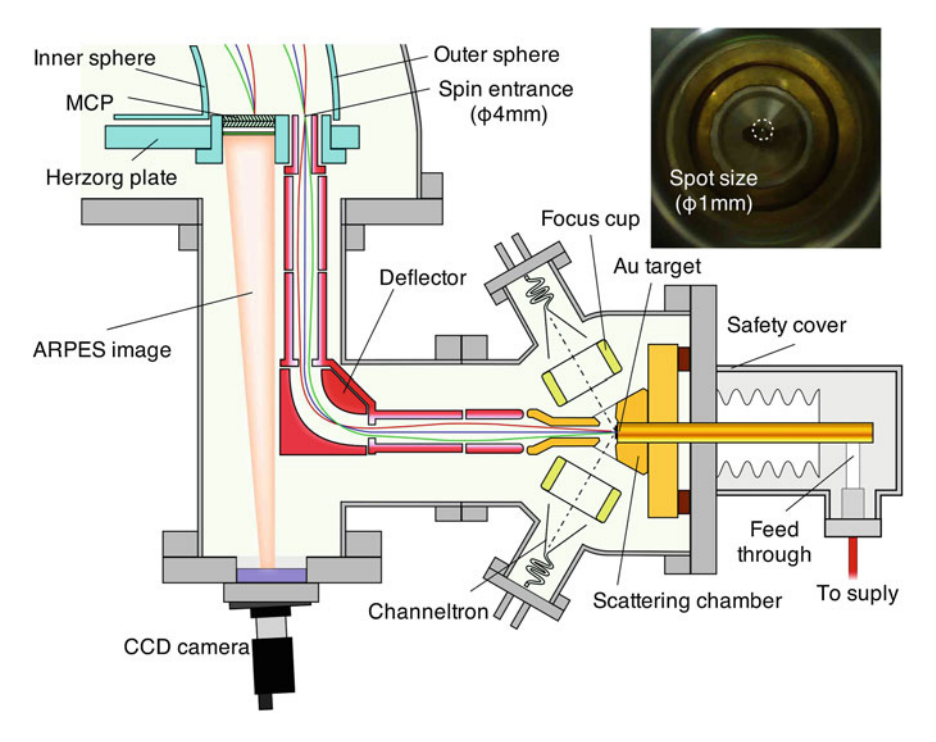


Fig. 3.7 A detailed diagram of the spin-detection system. *Upper right* inset shows the image of the fluorescent screen when electron beam is focused

estimation that the spin rotation is much less than 1° assuming that the full geomagnetism penetrates the vacuum camber. We have used non-magnetic elements such as titanium for the vacuum components and tools to reduce the effect of the magnetic field. The magnetic field at the Mott detector has been estimated to be less than 300 mG.

3.2.4 Discharge Problems

In the Mott detector, electric discharge can be naturally generated by applying the high voltage. In the case of the high-resolution spin-resolved measurement, number of electrons detected by the Mott detector is only a few counts per second (cps) therefore the background noise must be eliminated as low as we can. Unfortunately, the Mott detector encountered several serious electric discharges during the course of the development. This section explains these discharge problems.

The discharge is caused mainly by the strong local electric field in the detector. As displayed in Fig. 3.8, a breakdown voltage depends on the feature of electrode and distance between electrodes [6–8]. In the case of the Mott detector in this study,

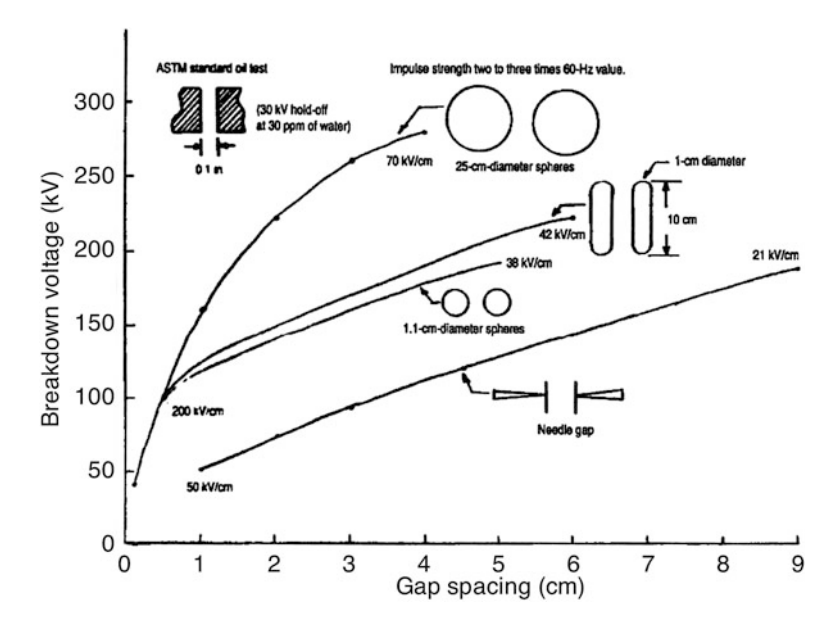


Fig. 3.8 Insulation performance of electrodes with various *shapes* compared to the breakdown voltage and gapsize at $T=25~^{\circ}\mathrm{C}$ [6]

narrowest distance between electrodes is less than 5 mm. Since the high voltage of more than 20 kV are applied in this narrow space, it causes a discharge if an electrode has a small scratch. The discharge spots are between the scattering chamber (25,000 V) and the focus cup (1,900 V), and between the scattering chamber and the end electrode of the deflector (3,300 V). These electrodes have some scratches and fine linear scars, which are probably produced by the surface fabrication and the parts assembly in the manufacture process. In order to remove these scratches, electrodes were polished by the following process; first, prominent and large scars were removed by lathe, then the electrodes were polished by sandpapers (#1,500, #2,000). The lapping films (#4,000, #6,000) were used at the end (Fig. 3.9a). Moreover, the four focus cups were coated by titanium carbide (TiC; a material with high hardness) to prevent a new scratch. Finally, all of the parts are cleaned in the alcohol. A discharge also took place between the high-voltage electrode and the ground potential. In particular, the channeltrons, in which the high voltage of 3,300 V is applied, has a lot of small components such as screws. To prevent a discharge for channeltorn, we have improved an insulating property by inserting a mica sheet as shown in Fig. 3.9b. A most dangerous discharges with sounds and sparks have been observed at the 25 kV high-voltage terminate. In order to remove the discharge, the insulation of the terminate was strengthened with the Teflon sheets and seals (Fig. 3.9c). Another origin of the discharge is the residual attachments like dust. Therefore, all the part of the Mott detector were repeatedly cleaned with alcohol, and then fabricated and installed into the Mott detector. After the baking, we applied the high-voltage for a long time to remove dusts.

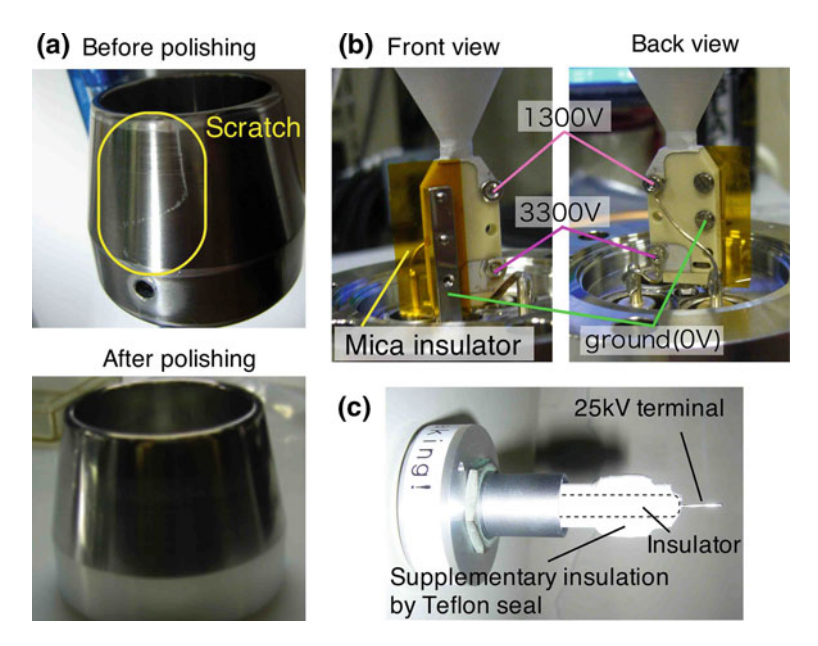


Fig. 3.9 Examples of the insulation process. **a** Focus cups were polished to eliminate some scratches. **b** Channeltron inserted with a mica insulator. **c** Feedthrough wrapped with a Teflon insulator

Figure 3.10 shows the photoemission spectra of Au 4*f* levels; top and low panels highlight the data without or with discharge, respectively. Before fixing the discharge problems, the noise level was increased on increasing the tagert voltage, and an intrinsic spectrum feature could not be extracted. However, after solving the discharge problem of the Mott detector, we achieved the noise level of ~0.1 cps at 25 kV.

3.2.5 Surface Chamber

In order to fabricate high-quality samples, a surface chamber has been constructed and is connected to the spin-resolved ARPRS spectrometer. Figure 3.11 shows a schematic view of the surface chamber. A surface chamber contains two heating systems for a metal or a semiconductor, a few kinds of dispensers, a quartz crystal microbalance, an ion gun for sputtering, and LEED and auger electron spectroscopy (AES) system for checking the surface. It allows the in situ preparation of the sample and its transfer to the spin-resolved spectrometer. The vacuum of the surface chamber is basically kept 1×10^{-10} Torr to prepare a high-quality sample surface. This section explains the detail of the surface chamber.

As shown in Fig. 3.12, a sample folder mounted in the manipulator has two functionalities; one is an electrical heating system mainly used for the

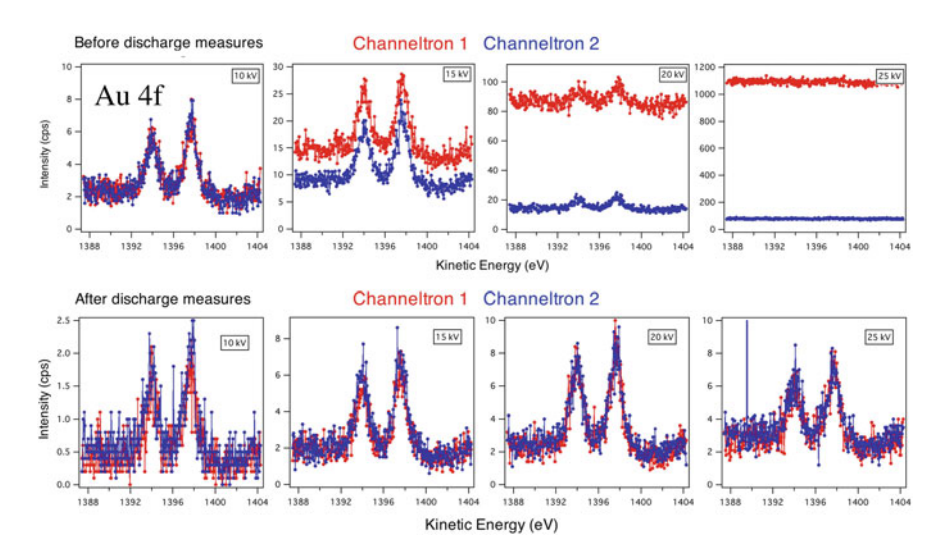


Fig. 3.10 Comparison of the Au 4*f* spectra before and after fixing the discharge problem. By eliminating the discharge, the Au 4*f* peaks become clearly visible

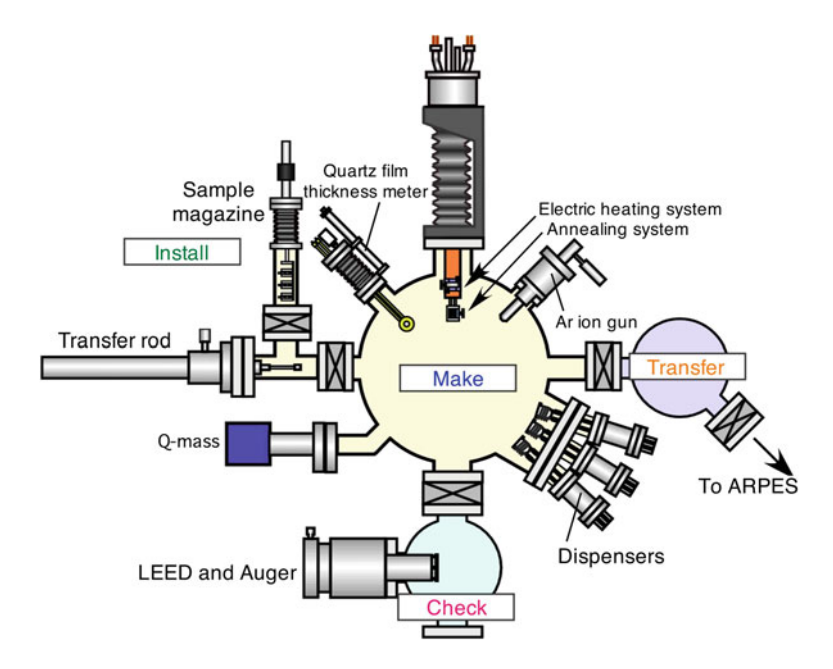


Fig. 3.11 Schematic view of the sample preparation chamber

semiconductors, and the other is the annealing system for metal which utilizes the radiation heating. These holders are faced to the opposite side, respectively, so we can select a sample holder depending on the material of the sample. To obtain a

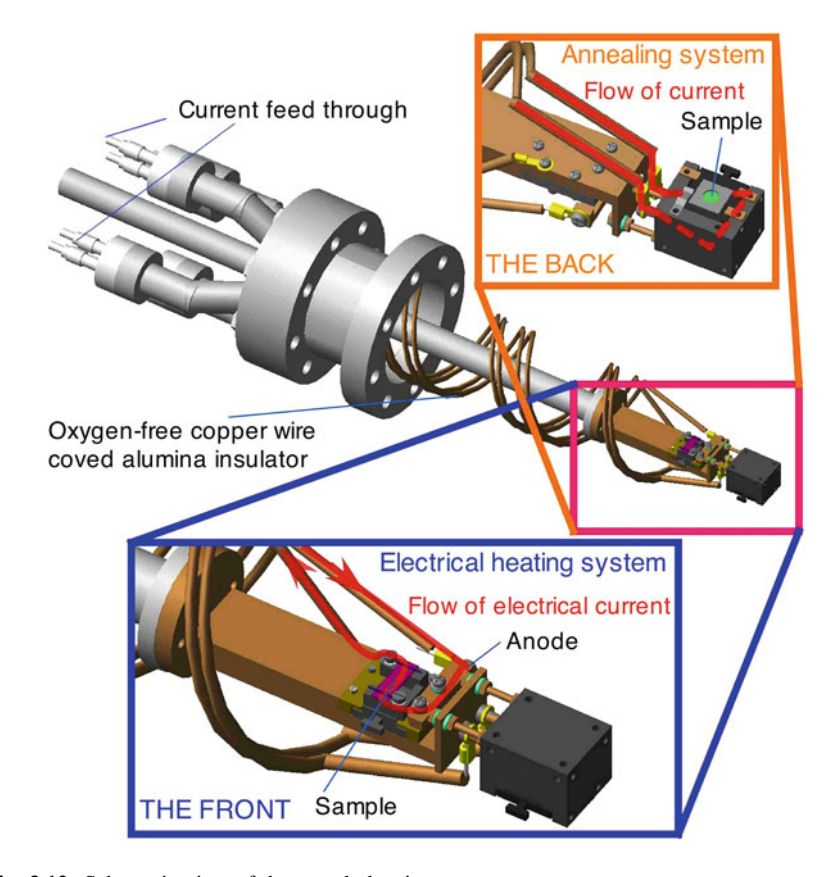


Fig. 3.12 Schematic view of the sample heating system

clean surface of the semiconductors such as Si(111)-1 × 1 reconstructed surface, we have to precisely control the heating temperature as well as its time scale by electrical heating system. A schematic view of a holder for the electrical heating system is displayed in Fig. 3.13. A sub holder is insulated from a main holder by the alumina insulator, thus current flows through a semiconductor like a bridge. The holder is made of molybdenum taking into account its high melting point. A current is controlled with an accuracy of 5 mA by a stabilized DC power supply together with a digital multi-meter, and the temperature is monitored with an accuracy of 1°. In the case of the metal sample, a clean surface is obtained by argon (Ar) ion sputtering and annealing. Figure 3.14 is a schematic view of the sputter and annealing system. Impurities, which are absorbed at the surface or appears to the the surface from the bulk, are removed by colliding Ar ions. Then, the surface becomes flattened by the high-temperature annealing. By repeating this cycle, we can obtain an atomically flat surface.

In order to prepare thin film like Bi/Si(111), atoms are evaporated by a dispenser on the substrate. This method is known as a molecular beam epitaxy (MBE). This

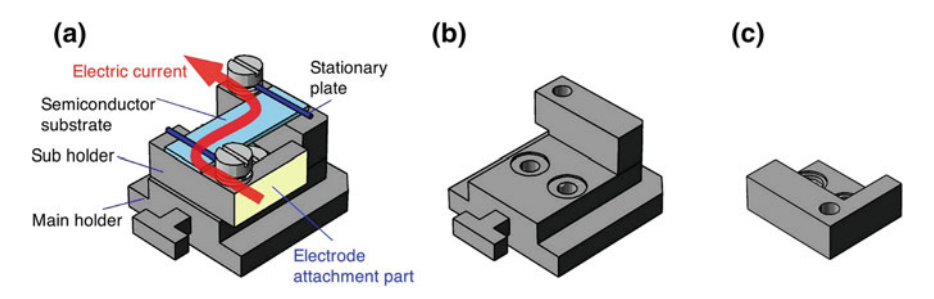
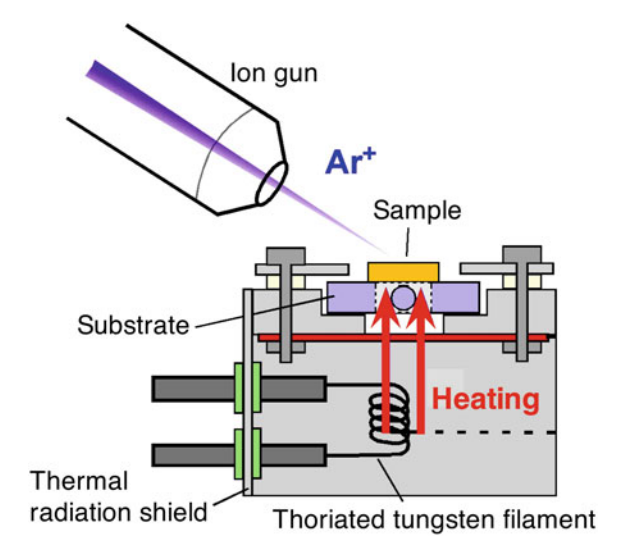


Fig. 3.13 a Sample holder composed of b A main part and c A sub part

Fig. 3.14 Schematic view of spatter and annealing system



study used a self-produced Bi dispenser (Fig. 3.15). Small pieces of Bi are entered into a tantalum tube, and are melted by the heat radiation of the tungsten filament. The deposition rate is estimated by the quartz-oscillator thickness monitor and the film thickness is controlled by varying the deposition time and rate.

The quality of the prepared sample is checked by LEED and AES in this surface chamber. The LEED is a technique to determine the surface structure of crystalline materials by bombardment with a collimated beam of low-energy electrons (20–200 eV), and it shows various electron-diffracted patterns at the fluorescent screen (see Fig. 3.16) depending on the surface structure [9]. The AES is a technique to determine atomic composition and to check impurity rate of surfaces by bombardment with a collimated beam of high-energy electrons (~1500 eV). It is noted that the AES sometimes destroy the surface owing to the collision of high-energy electrons.

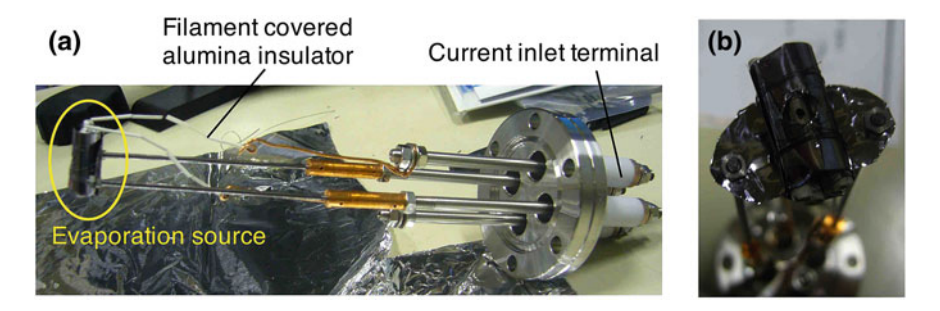


Fig. 3.15 a Overall and b Front views of the Bi dispenser

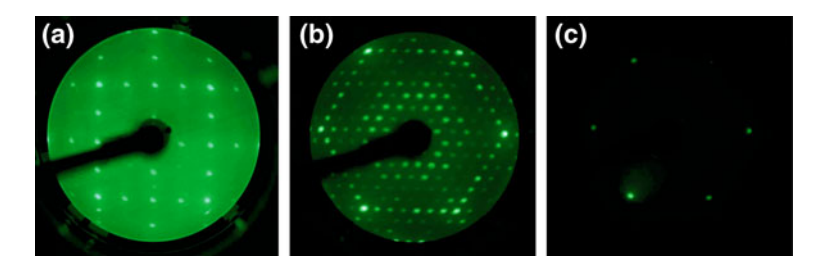


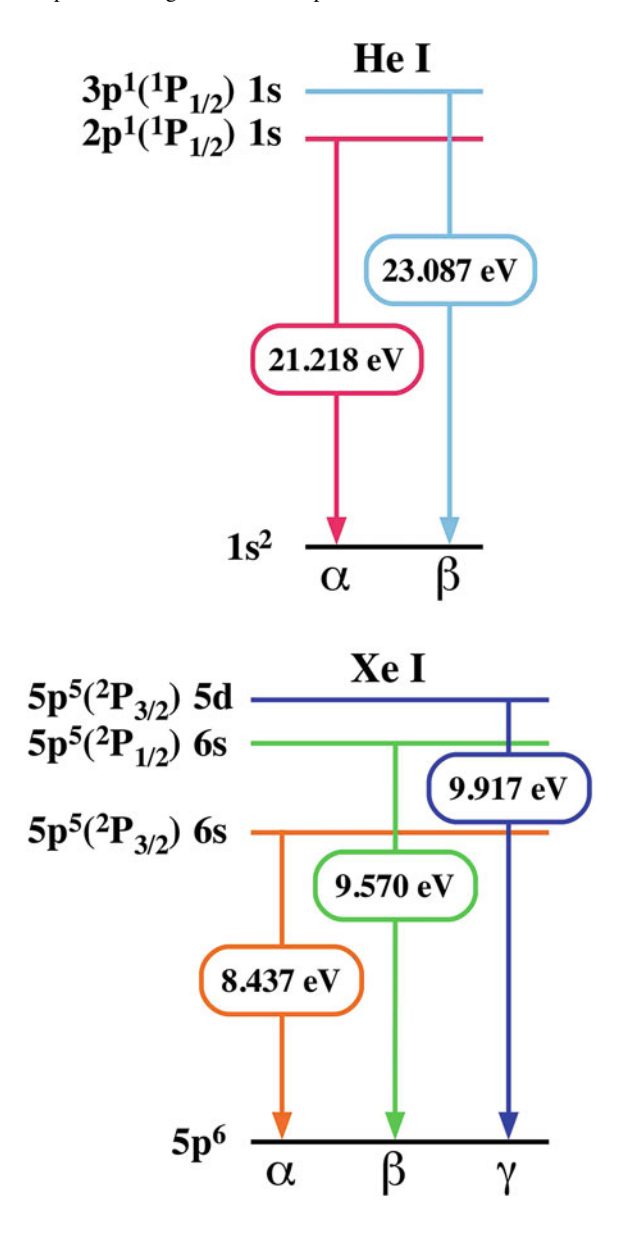
Fig. 3.16 LEED patterns for a Si(100)-1 \times 1, b Si(111)-7 \times 7, and c Bi(111)-1 \times 1

3.2.6 Other Refinements

It is important to use the highly brilliant excitation light source in order to improve the efficiency. The apparatus contains the electron cyclotron resonance (ECR) gas lamps with He and Xe. Photons in this style of lamp are generated by ionizing a gas to produce spectral emission. Cyclotron resonance is the phenomenon in which charged particles in a magnetic field begin to orbit in a circle perpendicular to the direction of magnetic field due to the Lorentz force. ECR lamps exploit this effect in order to confine a plasma of electrons using a magnet such as SmCo₅. The photon fluxes of the He I α line and the Xe I α line are 0.5 × 10¹³ photons/s, 1.6 × 10¹³ photons/s, respectively. The photon energy will depend on the types of gasses and resonance lines (Fig. 3.17). One of them is selected by the monochromator for experimental purpose. In this study, the Xe I line (8.437 eV) and the He I α line (21.218 eV) were used mainly. The line width of the lamp ΔE_{lamp} also influences the energy resolution, and the total energy resolution ΔE including the energy resolution of the analyzer $\Delta E_{\text{instrument}}$ (Eq. 3.1) is given by

$$\Delta E = \sqrt{\left(\Delta E_{\text{instrument}}\right)^2 + \left(\Delta E_{\text{lamp}}\right)^2} \tag{3.2}$$

Fig. 3.17 Example of the excitation diagram for He and Xe



At present, the ΔE_{lamp} value is achieved to be 1.2 meV for the He I α line and ~100 μ eV for the Xe I line, respectively. Moreover, the aluminum filter is used to prevent contamination of the measurement chamber by residual gasses in the He gas, and the MgF₂ window is used for the xenon lamp. To obtain high-quality data, an ultra-high vacuum is always necessary for the ARPES system. This ensures both the safety of the apparatus and the atomic cleanliness of samples. Figure 3.18 shows a systematic diagram of the vacuum system for the apparatus. The basic pumping

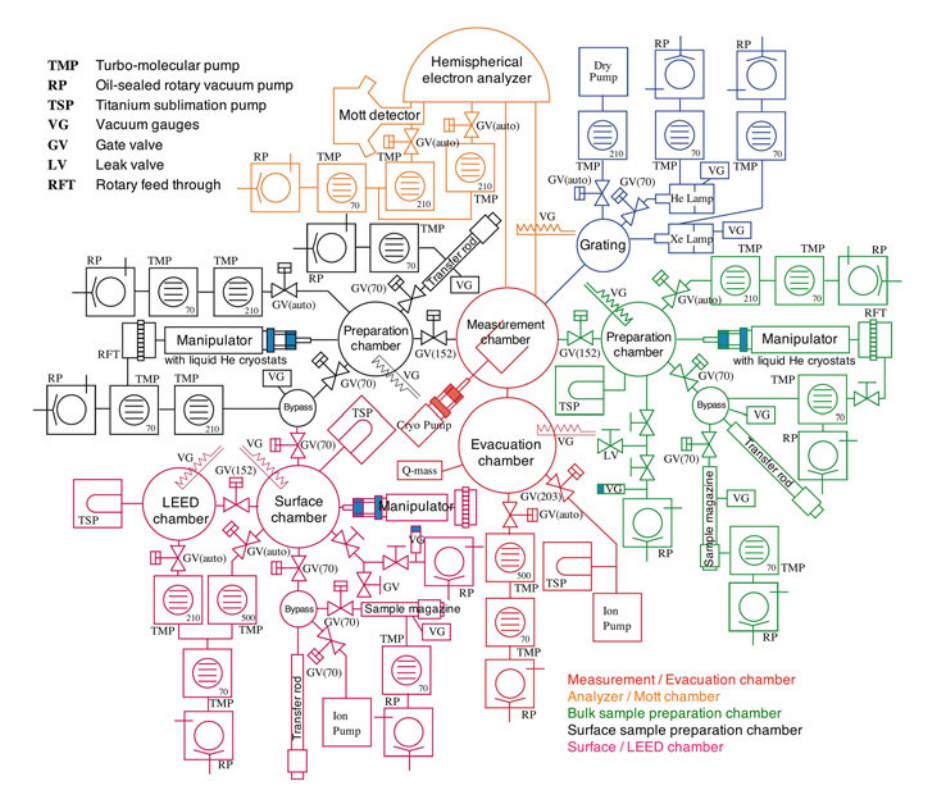


Fig. 3.18 Illustration of the ultra-high vacuum system

relies on a combination of rotary and turbo molecular pumps connected in series. Sputter-ion pumps and titanium sublimation pumps are also used. These are extremely effective for removing highly reactive gasses by chemical absorption. The cryopump, which is supercooled by liquid helium, removes inactive gas such as helium and hydrogen. The apparatus also contains the quadrupole mass spectrometer, so we can monitor the atom/molecule-specified vacuum levels. Moreover, all the apparatus are baked and degassed to improve the quality of the vacuum, thus the vacuum of the analyzer and the measurement chamber is 3×10^{-11} Torr.

Another important issue of the improvement of the apparatus is noted here. The sample stage and the measurement chamber are designed to reduce the stray heating radiation and magnetic fields. A measurement chamber is connected to a cryopump, which supercools them using the helium cycling system. This creates a cold surface capable of condensing gasses in the chamber, effectively removing them from the system. It is also insulated using a layer of Mu-metal to block static and low frequency magnetic fields. A sample stage has a helium cryostat to cool down the metal (semiconductor) samples down to 3.5 K (20 K). A preparation chamber has a screwdriver, a file, a knife to cleave a sample, and a gold evaporator for the calibration of the Fermi level.

3.3 System Test

3.3.1 Energy Resolution

The energy resolution of the spin-resolved system has been estimated by measuring the Fermi edge of polycrystalline gold at 10 K with the mini Mott detector. Figure 3.19a shows the valence-band photoemission spectra of gold measured with the He I α line (21.218 eV) at T=300 K. All the spectra observed by four channeltrons have the same feature as the non-spin-resolved photoemission data using the MCP. Figure 3.19b shows a photoemission spectrum measured with the Xe I line (8.437 eV) with the four channeltrons of the Mott detector. We find a steep Fermiedge cutoff whose slope is located within ± 5 meV with respect to $E_{\rm F}$. The observed PES spectrum is fitted by the Fermi–Dirac distribution function to determine the total energy resolution ΔE for this apparatus. A fitting function is given by

$$I(k,\omega) = I_0(k) \sum_{\delta k} \int d\omega' A(k',\omega') f(\omega') R(\sigma,\omega')$$
 (3.3)

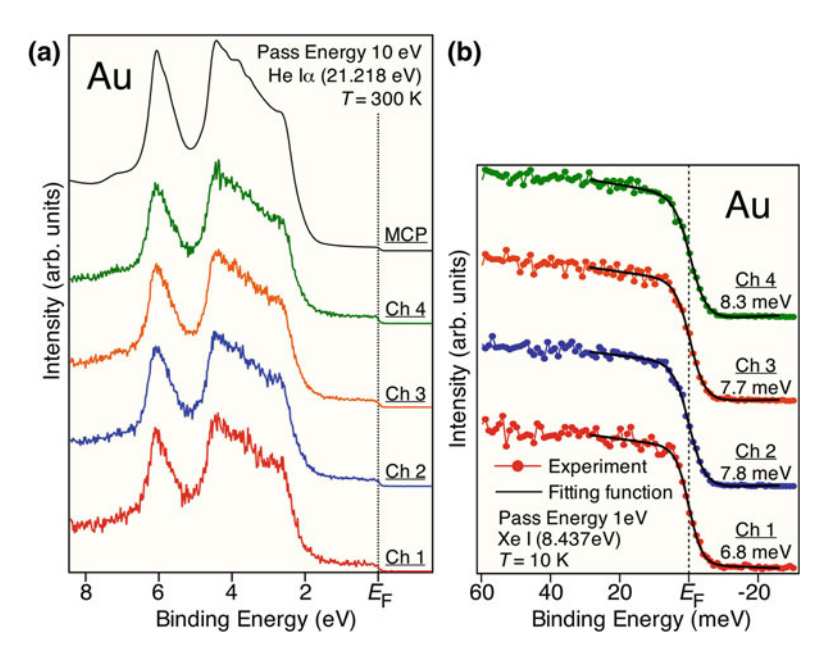


Fig. 3.19 a Valence-band and **b** near- $E_{\rm F}$ PES spectra of polycrystalline gold film measured by channeltrons of the new Mott detector. The spectrometer achieves the energy resolution of 8 meV with the spin-resolved mode

3.3 System Test 49

where

$$f(\omega) = \frac{1}{e^{\omega/k_B T} + 1} \tag{3.4}$$

$$R(\omega) = \frac{e^{-\omega^2/2\sigma^2}}{\sqrt{2\pi\sigma^2}} \tag{3.5}$$

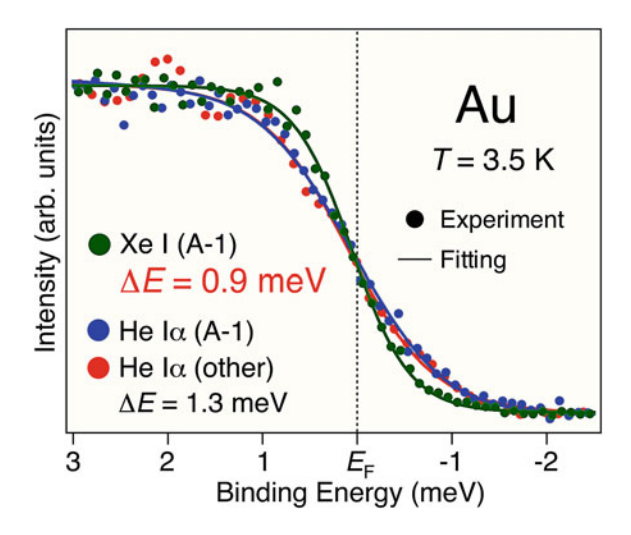
 $A(\omega)$ $a\omega + b$ reflects the assumption of a linear density of states near the Fermi level. This is multiplied by $f(\omega)$ (Fermi distribution function that represents the electron occupancy) at T = 10 K, and convoluted with a resolution function $R(\omega)$. The full width at half maximum (FWHM) for the experimental resolution term is given by 7

$$\Delta E = \text{FWHM} = \sqrt{8 \text{In} 2} \cdot \sigma \tag{3.6}$$

where σ is the standard deviation. From the fitting, energy resolution is obtained to be 6.8–8.3 meV for these channeltrons. This definitely establishes the high energy-resolution nature of the present spin-resolved ARPES system.

Next we determined the energy resolution of the MCP system. Figure 3.20 is a photoemission spectrum of a polycrystalline gold film measured with the Xe I line (8.437 eV) and the He I α line (21.218 eV) with the MCP at 3.5 K. Similar to the measurement with the Mott detector, we have performed numerical fittings to these spectra and obtained the energy resolution to be 0.9 meV for Xe I in the highest case. In addition, although the MCP has been moved in this spectrometer, the observed spectra with the He I α line is similar ($\Delta E = 1.3$ meV) to the other spectrometers, suggesting that the influence of the MCP movement is negligible.

Fig. 3.20 High-resolution near- E_F PES spectra of polycrystalline gold film measured by the MCP with the spin-integrated mode



3.3.2 Spin-Polarization

Next we have texted the spin-detection ability of the Mott detector. This test has been performed by measuring the surface Rashba states of Bi(111) since it is well known that the Rashba-type spin-orbit interaction lifts the spin-degeneracy of the Shockley-type surface band [10–15]. The experimental details for the Bi thin film on Si(111) as well as the detail of the sample preparation method is explained in Chap. 4. Figure 3.21a shows the ARPES intensity at Fermi energy (E_F) plotted as a function of two-dimensional wave vector around the $\bar{\Gamma}$ point of the surface Brillouin zone (BZ) and the corresponding band dispersions along the $\bar{\Gamma}$ \bar{M} line measured with \the Xe I line at T=30 K. All of these bands and Fermi surfaces are attributed to the surface states, where in-plane spin polarization is expected to show k-dependent structure as shown by arrows in Fig. 3.21a. Figure 3.21b shows the spin-resolved ARPES spectra for the in-plane spin polarization measured with the Xe I line at T=30 K in region A in Fig. 3.21a. Spin direction of the Mott detector was aligned to the y (parallel to the surface) and z (perpendicular to the surface) axes of the sample, and the energy resolution was set at 16 meV. The figure also

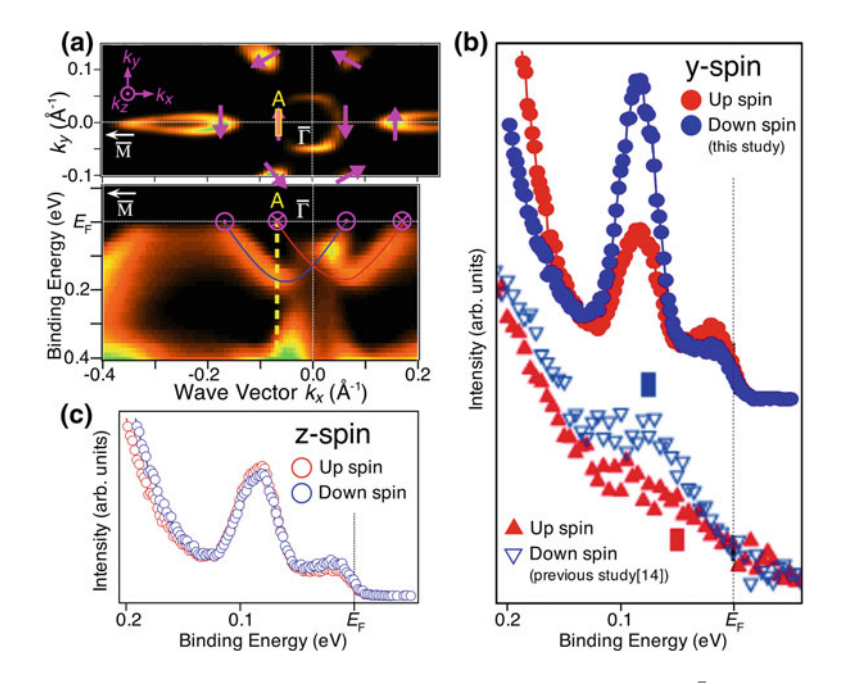
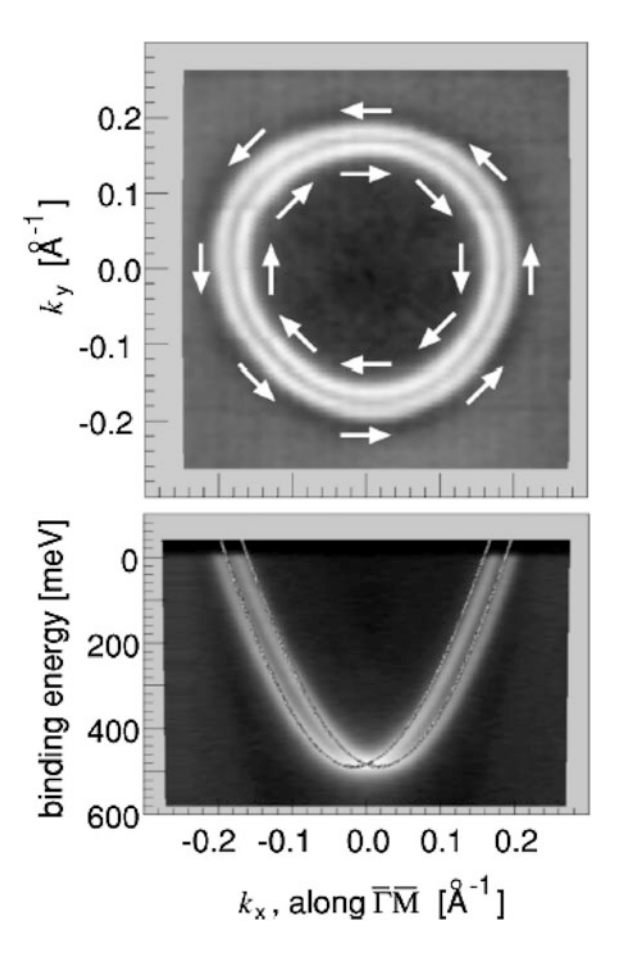


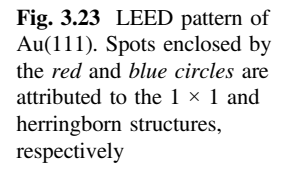
Fig. 3.21 a Fermi-surface mapping of Bi(111) at T=30 K around the $\bar{\Gamma}$ point and band dispersions along the $\bar{\Gamma}$ \bar{M} direction. The *arrows* indicate the spin direction at specific k points. *Blue* and *red lines* are guides for eyes to trace energy bands and spin direction. **b** In-plane (y) spin-resolved ARPES spectra measured at point A [see **a**] with the Xe I line at 30 K, the upper and downer spectra are observed by our and previous Mott detectors [14], respectively. **c** Out-of-plane (z) spin-resolved ARPES spectra

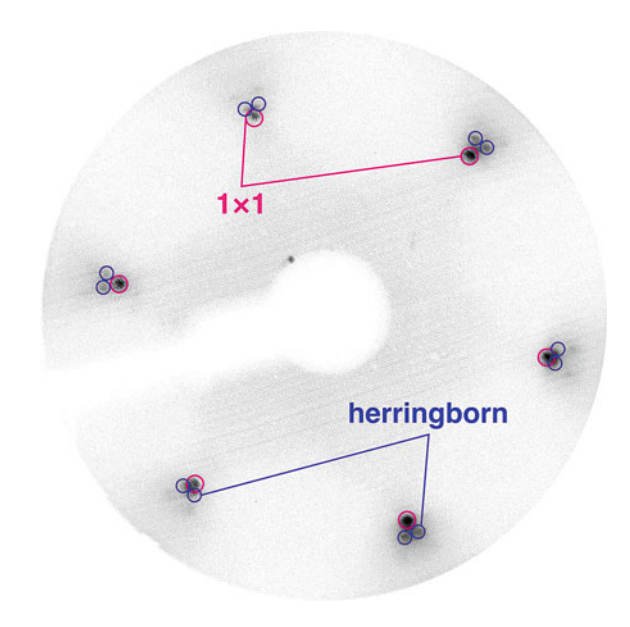
3.3 System Test 51

Fig. 3.22 Rashba-split surface state of Au(111) [19]



shows the result of previous study in comparison with this work. The effective Sherman function value S_{eff} is simply assumed to be 0.1 in our case to obtain the spin-resolved ARPES spectra. As clearly seen in Fig. 3.21b, the two peaks at 80 meV and $E_{\rm F}$, which were not well resolved in the previous studies [14] are clearly distinguished. More importantly, the 80 meV peak is stronger in the down-spin spectrum than that in the up-spin counterpart, while the $E_{\rm F}$ -peak is relatively stronger in the up-spin spectrum. This behavior is in sharp contrast to the z-axis case showing no discernible change in the up- and down-spin spectra in Fig. 3.21c. This result suggests a good agreement with the theoretical prediction of the intensity variation of the spin-resolved energy bands due to the surface Rashba effect [14]. The present spin-resolved ARPES measurement of the Bi(111) surface thus provides a direct evidence for the Rashba effect in the surface electronic states of Bi(111). In addition, it demonstrates the high energy-and spin-resolution capability of the present spin-resolved ARPES spectrometer.





3.3.3 Sharman Function of the Mott Detector

It is very important to experimentally determine the accurate $S_{\it eff}$ value of the Mott detector when we discuss the spin polarization of the band and the Fermi surface quantitatively. In this study, the $S_{\it eff}$ value is determined by the Au(111) surface state which has the Rashba-type spin-split bands. As shown in Fig. 3.22, Au(111) shows two free-electron-like parabolic surface bands and two concentric circular Fermi surfaces [16–19]. Such spin polarization conforms the conventional Rashba effect where the inner (outer) circular Fermi surface has in-plane clockwise (anti-clockwise) spin polarization without the out-of-plane spin component [18, 19]. We assumed that the spectra of Au(111) observed by the Mott detector has a 100 % in-plane spin component, thus by fitting the observed spectra, it is possible to estimate the adequate $S_{\it eff}$ value.

The sample was prepared by repeated cycles of Ar ion sputtering at 1 kV and annealing of a mechanically polished Au(111) surface. To remove impurities (mainly carbon) completely, the annealing temperature was set at $T \sim 650$ °C for repeated cycles, and at T = 500 °C for last annealing, although the annealing was performed at T = 500 °C in the previous report [19]. Figure 3.23 shows a LEED pattern for prepared Au(111). We clearly confirm Au(111) 1 × 1 spots. We can also see another spots around the 1 × 1 spot, which are called "herringborn" derived from reconstructed surface [20–22]. This indicates that a high quality sample has been fabricated in this study.

3.3 System Test 53

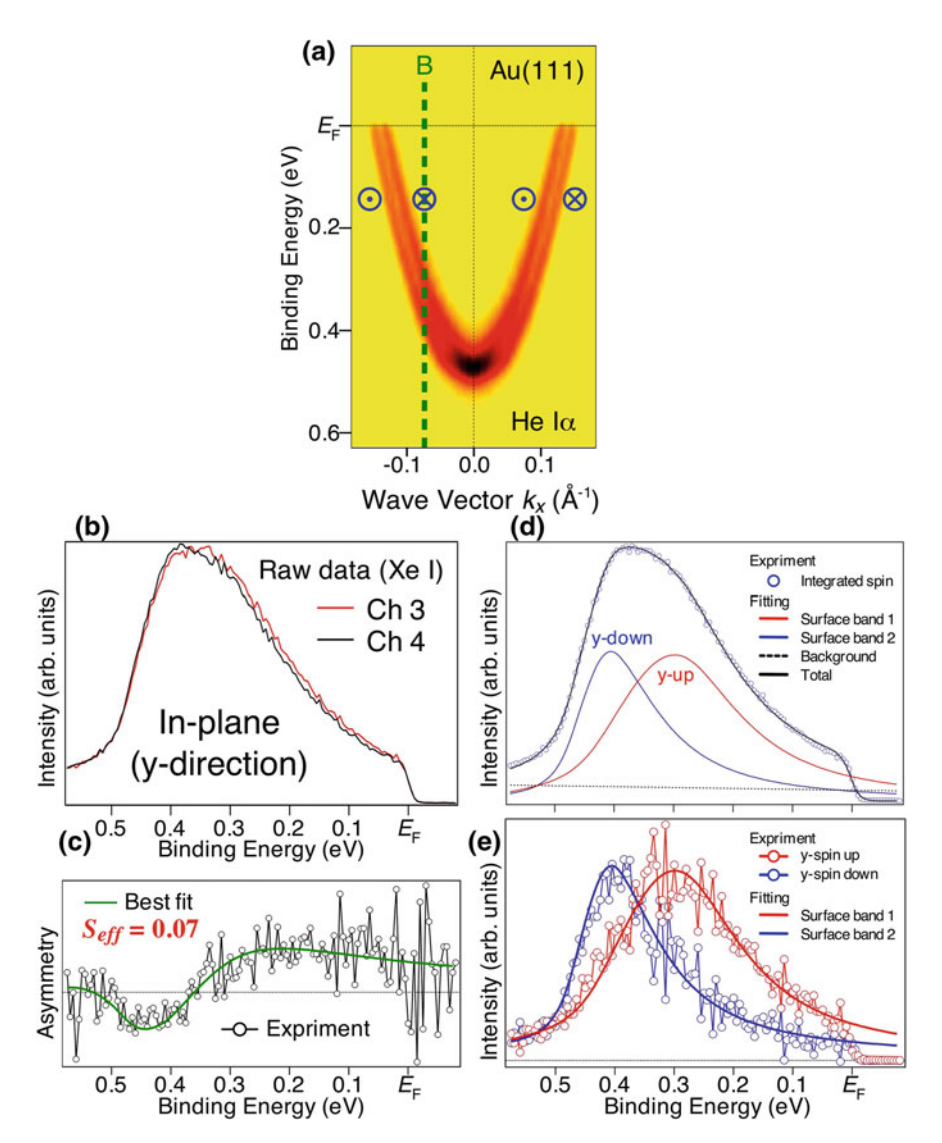


Fig. 3.24 a The photoemission intensity of Au(111) around the $\overline{\Gamma}$ point measured with the He Iα line. b-e Determination of the effective Sherman function. b Raw ARPES spectra observed with channeltrons. c-d Numerical fittings for the spin-integrated spectrum and spin polarization. e Spin-resolved EDCs and corresponding fitting results for $S_{eff} = 0.07$

Figure 3.24a shows the band dispersion of the Au(111) surface state around the $\bar{\Gamma}$ point measured with the He I α line at T=30 K. Figure 3.24b shows raw spectra measured by the right-and left-side channeltorns with the Xe I line in region B in Fig. 3.24a. We can obtain in-plane spin-polarized EDCs from these spectra (see

Sect. 2.2.4). The up- and down-spin EDCs are slightly different, witch means that these bands have a spin polarization. Now we determine the value S_{eff} from the result. First a total ($N_{\rm R}+N_{\rm L}$) and differential ($N_{\rm R}-N_{\rm L}$) spectrum were obtained from the experimental spectra, then a scattering asymmetry A defined as ($N_{\rm R}-N_{\rm L}$)/ ($N_{\rm R}+N_{\rm L}$) was derived (Fig. 3.24c). Here the total (spin-integrated) spectrum is assumed to consist of the up-and down-spin EDCs which are polarized to be 100 % with a background. For this reason, the total spectrum is fitted by two Lorentzians with a finite background as shown in Fig. 3.24d. Finally, the S_{eff} is estimated as 0. 07 \pm 0.01 from the experimental scattering asymmetry A and the numerical fittings. It is noted that the calculated EDCs by assuming $S_{eff}=0.07$ reasonably overlaps with the experimental data (Fig. 3.24e), supporting the validity of the obtained S_{eff} value.

3.4 Summary

To perform the high-resolution spin-resolved ARPES measurements, we have developed an ultrahigh-resolution spin-resolved ARPES spectrometer with a highly efficient mini Mott detector. In order to increase the efficiency of the Mott detector, we developed a new detector with a large acceptance angle and a flat target. To perform the regular and spin-resolved ARPES measurements at the same time, the MCP was shifted toward the inner-sphere of the hemispherical electron analyzer by 1 cm. The electron deflector situated in front of the Mott detector enabled the determination of the spin polarization in three independent directions. The spectrometer achieves the energy resolutions of 0.9 and 8 meV for non-spin-resolved and spin-resolved modes, respectively. The performance test of the spectrometer was performed by measuring well-separated spin-polarized Rashba-split surface bands in Bi(111). The effective Sherman function S_{eff} of the Mott detector is estimated as 0.07 ± 0.01 by measuring the Au(111) surface state. These results demonstrate that the high-resolution spin-resolved ARPES technique opens a pathway to studying the novel spin states of various materials such as surface Rashba systems, half metals, and topological insulators.

References

- S. Souma, A. Takayama, K. Sugawara, T. Sato, T. Takahashi, Rev. Sci. Instrum. 81, 095101 (2010)
- S. Souma, T. Sato, T. Takahashi, P. Baltzer, Rev. Sci. Instrum. 78, 123104 (2007)
- 3. E.M. Purcell, Phys. Rev. 54, 818 (1938)
- 4. H.D. Polaschegg, Appl. Phys. 9, 223 (1976)
- 5. P. Baker, B. Wannberg, M.C. Göthe, Rev. Sci. Instrum. 62, 643 (1991)
- W. North, High Power Microwave Tube Transmission (Los Alamos National Laboratory, Los Alamos, 1994)

References 55

7. T. Kouno, *Shin-pan Kodenatsu-Kogaku New edition High-voltage engineering* (Asakura Publishing Co., Ltd, Japan, 1994) (in Japanese)

- 8. A. Ando, M. Inutake, *Kodenatsu-Kogaku High-voltage engineering* (Asakura Publishing Co., Ltd, Japan, 2006) (in Japanese)
- 9. The Surface Science Society of Japan (ed.), *Hyomen denshi-sen kaisetu Surface electron diffraction for nanotechnology* (Maruzen Publishing Co., Ltd, Japan, 2003) (in Japanese)
- 10. C.R. Ast, H. Höchst, Phys. Rev. Lett. 87, 177602 (2001)
- Y.M. Koroteev, G. Bihlmayer, J.E. Gayone, E.V. Chulkov, S. Blügel, P.M. Echenique, Ph. Hofmann, Phys. Rev. Lett. 93, 046403 (2004)
- 12. Ph Hofmann, Prog. Surf. Sci. 81, 191 (2006)
- T. Hirahara, T. Nagao, I. Matsuda, G. Bihlmayer, E.V. Chulkov, Y.M. Koroteev, P.M. Echenique, M. Saito, S. Hasegawa, Phys. Rev. Lett. 97, 146803 (2006)
- T. Hirahara, K. Miyamoto, I. Matsuda, T. Kadono, A. Kimura, T. Nagao, G. Bihlmayer, E.V. Chulkov, S. Qiao, K. Shimada, H. Namatame, M. Taniguchi, S. Hasegawa, Phys. Rev. B 76, 153305 (2007)
- A. Kimura, E.E. Krasovskii, R. Nishimura, K. Miyamoto, T. Kadono, K. Kanomaru, E.V. Chulkov, G. Bihlmayer, K. Shimada, H. Namatame, M. Taniguchi, Phys. Rev. Lett. 105, 076804 (2010)
- 16. S. LaShell, B.A. McDougall, E. Jensen, Phys. Rev. Lett. 77, 3419 (1996)
- 17. G. Nicolay, F. Reinert, S. Hüfner, P. Blaha, Phys. Rev. B 65, 033407 (2001)
- J. Henk, M. Hoesch, J. Osterwalder, A. Ernst, P. Bruno, J. Phys. Condens. Matter 16, 7581 (2004)
- M. Hoesch, M. Muntwiler, V.N. Petrov, M. Hengsberger, L. Patthey, M. Shi, M. Falub, T. Greber, J. Osterwalder, Phys. Rev. B 69, 241401(R) (2004)
- M.A. Van Hove, R.J. Koestner, P.C. Stair, J.P. Bibérian, L.L. Kesmodel, I. Bartoš, G.A. Somorjai, Surf. Sci. 103, 189 (1981)
- 21. U. Harten, A.M. Lahee, J.P. Toennies, Ch. Wöll, Phys. Rev. Lett. 54, 2619 (1985)
- 22. F. Reinert, G. Nicolay, Appl. Phys. A **78**, 817 (2004)

Chapter 4 Anomalous Rashba Effect of a Bi Thin Film on Si(111)

This chapter describes the high-resolution spin- and angle-resolved photoemission spectroscopy (spin-resolved ARPES) result of Bi thin film on Si(111) substrate to investigate the spin structure of surface states. Unlike the conventional Rashba splitting, the magnitude of the in-plane spin polarization was found to be asymmetric between the two elongated surface hole pockets across the Brillouin-zone center. Moreover, the spin polarization has a giant out-of-plane component as large as the in-plane counterpart which switches the sign across the $\overline{\Gamma M}$ line. These observations are discussed in relation to the threefold symmetry of the bilayer Bi crystal.

4.1 Background and Goal of Research

The Group-V semimetal bismuth (Bi) is a prime candidate to investigate the surface Rashba effect [1], since the energy splitting is fairly large owing to the heavy mass of the Bi atom. A first demonstration of the band splitting was reported by Ast and Höchst [2], where they have shown the existence of two types of surface-derived Fermi surfaces (FSs) different from the bulk states in Bi(111), a small hexagonal electron pocket centered at the $\overline{\Gamma}$ point and six elongated hole pockets as shown in Fig. 4.1. Soon after this report, Koroteev et al. [3] have concluded that these two different FSs originate from the spin-split bands due to the strong spin-orbit coupling. Bi is a prime candidate to investigate the nature of the Rashba spin splitting since the magnitude of the splitting is fairly large owing to the heavy mass character of the Bi atom. In comparison to other Rashba systems, the spin splitting of the Bi(111) surface state is at least one-order of magnitude larger than that of Au(111) [4–7] and semiconductor heterostructures [8], thus the Rashba effect of Bi has been intensively studied by many experiments and theoretical calculations in order to clarify the fundamental properties of the Rashba effect [2, 3, 9–12]. Recently, spin-resolved ARPES study of Bi [11] elucidated that the band splitting indeed derives from the Rashba splitting where the in-plane spin polarization vector is antisymmetric with respect to the zone center (Fig. 4.2), as expected from the theory [1].

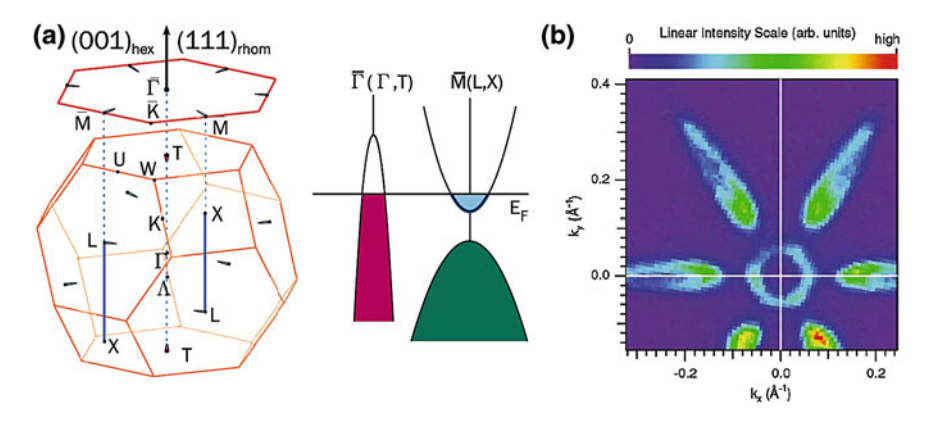


Fig. 4.1 a Schematic view of the Brillouin zone and bulk band structure of Bi(111) [10]. b Fermi surface of Bi(111) around the $\overline{\Gamma}$ point [2]

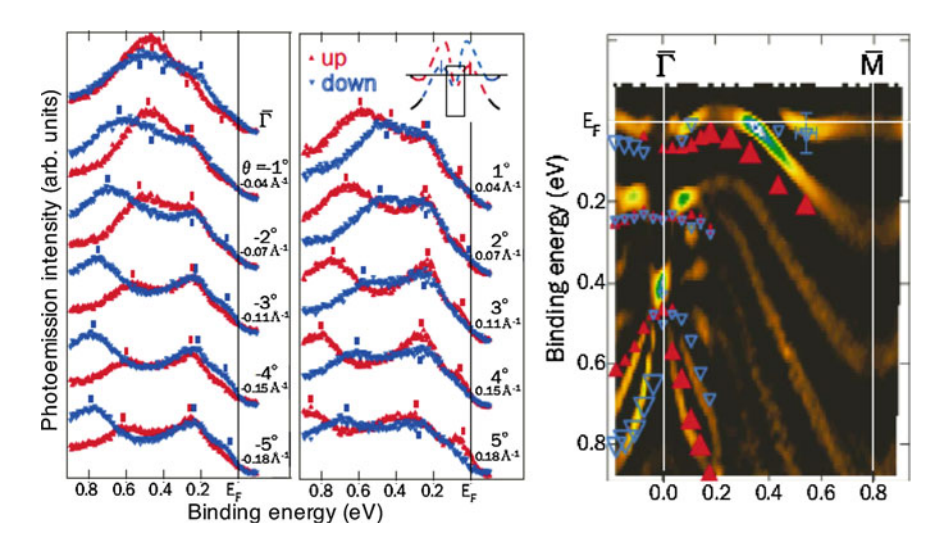


Fig. 4.2 Result of the spin-resolved ARPES measurements for the Bi(111) thin film in the previous study [11]

However, the spin structure of Bi was discussed by assuming a simple isotropic two circular Fermi-surface model as in the case of Au(111) [4–7] owing to insufficient energy resolution and momentum accuracy of the previous spin-resolved ARPES measurements, although the FSs and the band dispersion of Bi clearly show strong anisotropy. It is thus unclear to what extent the so-far believed simple vortical spin structure in conventional Rashba model is adequate. To find a possible deviation would be crucial in the correct understanding of the surface properties of the Rashba system.

In this chapter, we show by the spin-resolved ARPES measurements with greatly improved resolution and the higher k region accuracy that the surface spin states of the Bi/Si(111) thin film exhibit unprecedented characters unlike the conventional Rashba splitting.

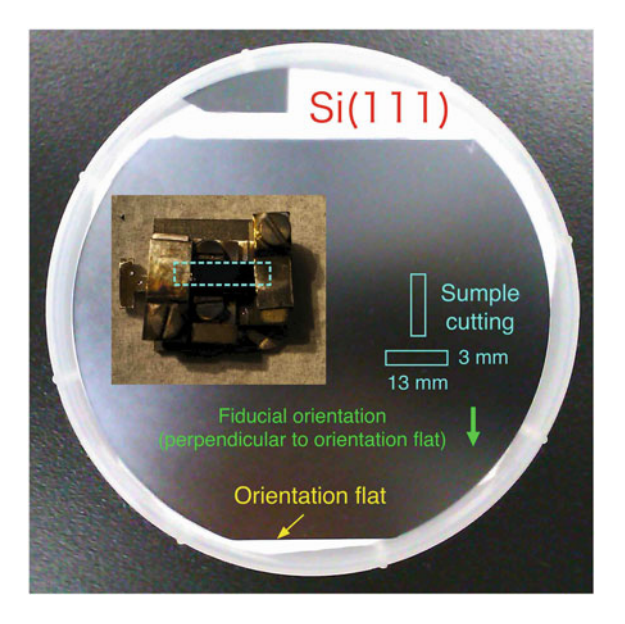
4.2 Experimental Conditions

Bi(111) thin films used in the spin-resolved ARPES measurements were prepared on clean Si(111) substrate. Preparation of the sample was performed at the surface camber. Sample quality was checked at the LEED chamber and the sample was transferred *in situ* to the spin-resolved ARPES spectrometer. This section describes the preparation of the Bi/Si(111) thin film.

One of the requested conditions to make a high-quality Bi thin film is to prepare a clean surface of the Si substrate. A surface of commercially available Si wafer forms native oxide film (SiO₂) in the air, and we must remove it by heating in vacuum to obtain a clean surface. We used an n-type Si wafer which has a low resistance value (As-doped: $0.001 \sim 0.005~\Omega$ cm) in order to accurately control the temperature. As shown in Fig. 4.3, the sample size is $13 \times 3~\text{mm}$ and we have selected four different kinds of crystal orientations when we cut the sample from the original wafer. Here we can identify the crystal orientation with flat part called "orientation flat". The sample geometry has been confirmed by the position/symmetry of the LEED spots.

The most stable structure of the Si(111) surface is the 7×7 reconstructed surface, as shown in Fig. 4.4 [13, 14]. In this case, the number of unstable dangling

Fig. 4.3 Cutting the sample from the Si(111) wafer. Inset shows the picture of a sample holder compared to the sample size. The geometry of the sample was determined by the direction of "orientation flat"



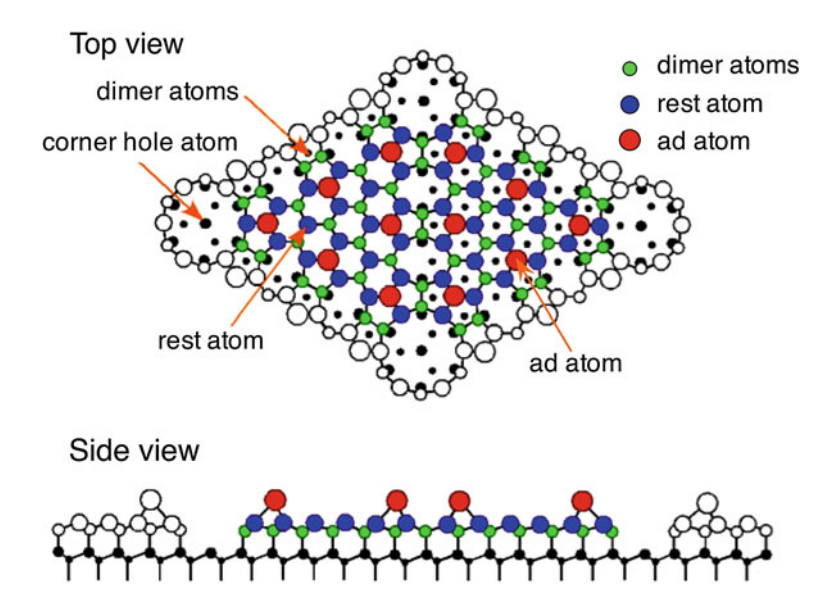
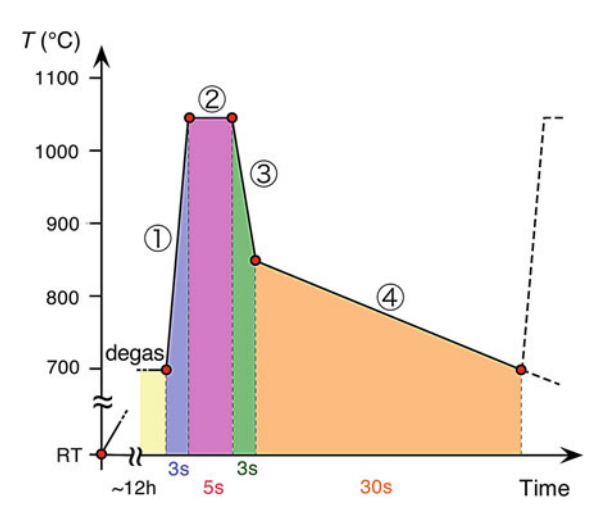


Fig. 4.4 Atomic-structure model (Das model) of $Si(111)-7 \times 7$ [15]

bonds decreases from 49 to 19 by the surface reconstruction. Si(111)-7 \times 7 reconstructed surface has been prepared by the electric heating method under the ultrahigh vacuum of ~1 \times 10⁻¹⁰ Torr. First, the wafers were outgassed for 1 day by slowly raising the temperature up to 700 °C. After the vacuum level of the chamber recovered, we have started cycles of a flash annealing. Figure 4.5 shows a detailed procedure of a flash annealing to obtain a clean Si-7 \times 7 surface; sample was ①

Fig. 4.5 Detailed annealing process to prepare the Si (111)-7 × 7 clean surface



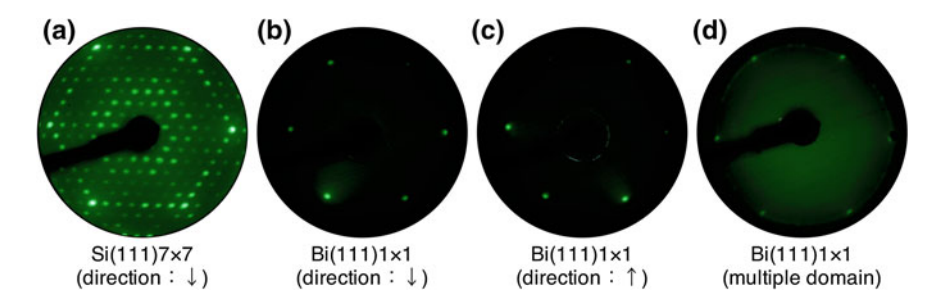


Fig. 4.6 Comparison of the LEED pattern. a Si(111)-7 \times 7. b, c Bi(111)-1 \times 1. These two samples have a different cutting directions from Si wafer (sample direction in c is rotated in 180° from b)

heated at 700–1,050 °C for a few seconds, ② flashed to 1,050 °C for 5 seconds to diffuse residual surface carbon into the bulk, ③ cooled down to 850 °C for a few seconds, and ④ finally cooled to 700 °C in 30 seconds. We have repeated this cycle over ten times. The most critical part of this procedure is a quenching down to 850 °C because the phase transition of Si(111) surface from 1×1 to 7×7 takes place at ~800 °C [15]. To obtain a long-range 7×7 domains, the temperature of the sample was kept at 850 °C for 10 min between the step ③ and ④ in the last cycle of the flash annealing. As shown in Fig. 4.6a, the LEED pattern of the obtained surface indicates the well-ordered 7×7 surface.

Bi atoms were deposited at room temperature on Si(111)-7 \times 7 and the film was annealed at 150 °C. The film thickness was controlled by varying the deposition time with keeping the constant deposition rate (0.09 Å/s) and was estimated by the quartz-oscillator thickness monitor. While the total deposition amount can be expressed in monolayer (ML) or bilayer (BL) unit, this study adopts the BL notation because of the threefold symmetry of the Bi crystal. Here 1 BL is defined as 1.14×10^{15} atoms/cm², and the thickness of 1 BL is 0.39 nm [11]. The film thickness used in the ARPES measurements was estimated to be 40 BL. As shown in Fig. 4.6b, after the deposition of Bi atoms, the 1 \times 1 surface structure was confirmed by the LEED measurement, where the intensity of the spot has shown threefold symmetry. On the other hand, the LEED pattern for the poorer quality surface shows a circular features surrounding the 1 \times 1 spots, which suggests that the sample has a multi-domain structure (Fig. 4.6d). A clean 1 \times 1 surface structure has been confirmed prior to the ARPES measurements.

ARPES measurements were performed using the spin-resolved ARPES spectrometer as presented in Chap. 3, and we used one of the Xe I lines (8.437 eV) to excite photoelectrons. The energy and momentum resolutions during the regular and spin-resolved ARPES measurements were 5 meV and 0.3°, 40 meV and 3°, respectively. The Sherman function value to obtain the spin-resolved ARPES spectra was set at 0.07. The film thickness has been estimated to be 40 BL from the energy position of the quantum well states as described later in detail.

4.3 Results and Discussions

When we discuss the complicated spin structure of the Rashba states which strongly depends on k, it is of particular importance to measure the spin-resolved energy distribution curves (EDCs) by specifying the absolute k location in the 2D Brillouin zone (BZ). At first, regular- (spin-integrated) ARPES measurement of the Bi thin film is performed in order to check the sample quality and geometry, since even a subtle misalignment of the sample orientation would cause a significant error in determining the spin polarization. Figure 4.7a shows the raw ARPES spectra and Fig. 4.7b corresponding intensity plot as a function of the wave vector k_x and the binding energy $E_{\rm B}$ for Bi/Si(111) along the $\overline{\Gamma \rm M}$ line of the surface BZ at $T=30~\rm K$. Enclosed ereas with hatched lines are bulk band projection. Within the bulk band gap, we clearly find a few dispersive bands which cross $E_{\rm F}$. Figure 4.7c shows the plot of ARPES intensity at $E_{\rm F}$ around the $\overline{\Gamma \rm M}$ line as a function of 2D wave vector. One can see three kinds FSs; a small FS centered at the $\overline{\Gamma}$ point (S₁) and surrounding elongated pockets (S_2) , together with the ellipsoidal pocket (S_3) near the \overline{M} point. Judged from the band dispersion in Fig. 4.7a, b, the S_1 and S_3 FSs are attributed to the electron pockets while the S2 FS to a hole pocket, all of which arise from the spin-split surface states [2, 3, 9-11]. It is inffered from the FS plot in Fig. 4.7c that a sample has a single domain. We find that the intensity of the each S_2 FS pocket is different owing to the threefold symmetry of the bulk Bi. Most of the bands located at the binding energies higher than ~0.2 eV belong to the tail of the quantum well states (QWSs).

Next issue is about the spin-resolved ARPES data of the S_2 band where a quite anomalous behavior is clearly observed. In Fig. 4.8b, c, we display the near- $E_{\rm F}$ spin-resolved energy distribution curves (EDCs) for the in-plane (y) and out-of-plane (z) spin components measured in various k regions, A-J as shown in Fig. 4.8a. In the present geometry of the ARPES spectrometer, two detector, namely the MCP and the channeltrons of the Mott detector simultaneously collect the angular dependence of the spin-integrated ARPES intensity and the spin-resolved EDCs, making it possible to specify the k region with higher accuracy as seen in the rectangle of Fig. 4.8a. As displayed in Fig. 4.8b, c, the spin-resolved EDC mainly consists of two components, a slopelike feature which rapidly increases its intensity at the binding energy higher than 0.15 eV, and a weaker broad feature at $E_{\rm F} = 0.1$ eV. The former corresponds to the tail of the QWS, while the latter is assigned as the S_2 band. The broad nature of the S_2 band is due to the k-integration effect of the highly dispersive S_2 band.

This study focuses on the spin structure of the S_2 band. In an ideal 2D Rashba picture, the in-plane spin has a vortical structure and isotropic magnitude as denoted by gray arrows in Fig. 4.8a. First the in-plane (*y*-axis) spin polarization in regions A-D is explained. As seen in Fig. 4.8b, the spin-resolved EDCs of the S_2 band in regions A and B are dominated by the up spin, while the down spin is slightly superior in regions C and D. This indicates that the in-plane spin direction is basically reversed in the two opposite S_2 pockets across the $\overline{\Gamma}$ point, qualitatively

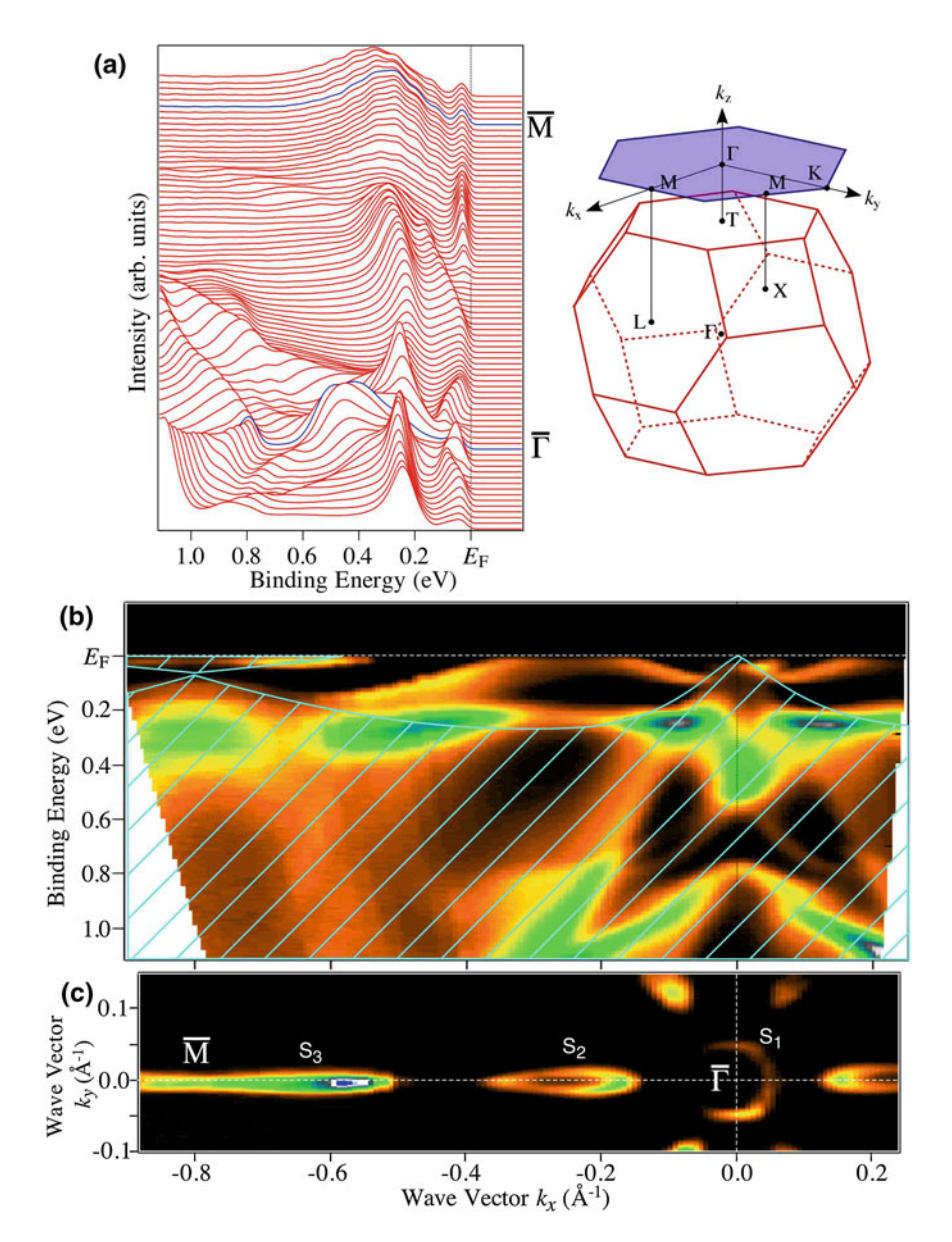
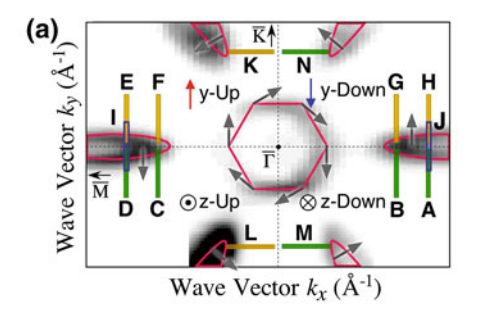


Fig. 4.7 a Raw ARPES spectra of Bi/Si(111) measured along the $\overline{\Gamma M}$ line at T=30 K. Blue lines show the spectra for the symmetry point in BZ. b Corresponding band dispersion of the ARPES spectra in a. Shaded areas indicate the bulk-band projection. c 2D ARPES intensity plot at $E_{\rm F}$ of Bi/Si(111) as a function of k_x and k_y around the $\overline{\Gamma M}$ line

consistent with the Rashba picture [10–12]. However, a closer look also reveals that the spin polarization is markedly suppressed in C and D. In fact, the magnitude of the spin polarization along the y direction $|P_y|$, defined as $P = (N_{\uparrow} - N_{\downarrow}) / (N_{\uparrow} + N_{\downarrow})$



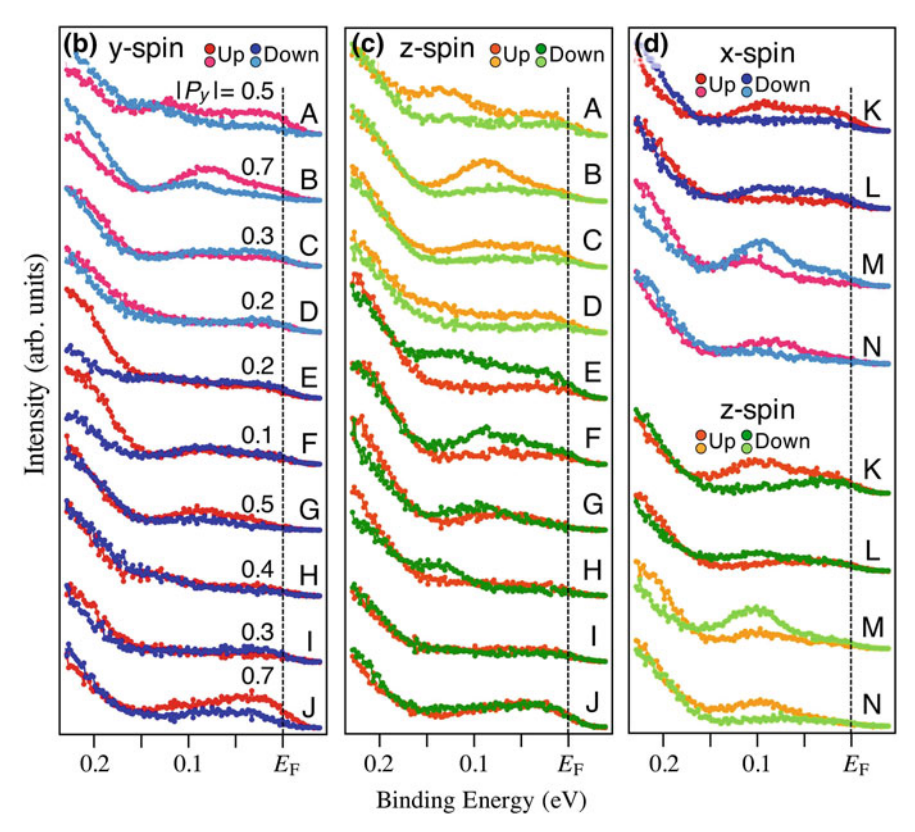


Fig. 4.8 a Fermi surface of Bi/Si(111) around the $\overline{\Gamma M}$ line. *Red lines* are guides for the Fermi surface of the surface bands. Lines A–N represent the k region where the spin-resolved EDCs in \mathbf{b} , \mathbf{c} and \mathbf{d} were obtained. The data in regions E–J (M–N) were taken by rotating the sample by 180° with respect to those in regions A–D (K–L). Expected spin configuration from the normal Rashba spin-obit coupling is indicated by gray arrows. Definition of the spin vectors for y- and z-spin components is also indicated. \mathbf{b} , \mathbf{c} Spin-resolved EDCs in regions A–J, for y- and z-spin components, respectively. Maximum value of $|P_y|$ is also indicated in \mathbf{b} . \mathbf{e} Corresponding Spin-resolved EDCs for both x- and z-spin components

where N_{\uparrow} and N_{\downarrow} are the spectral intensity of the up- and down-spin states, respectively, is 0.5–0.7 in regions A and B, while it is 0.2–0.3 in regions C and D. This is unexpected since $|P_y|$ should keep the same value across the $\overline{\Gamma}$ point in the normal Rashba picture. The result is shown for regions E-H (also regions I and J). In this geometry, the overall intensity of the S₂ band is relatively suppressed, likely due to the photoexcitation selection rule and threefold symmetry of the crystal. Whereas the trend of y-spin asymmetry still holds. In fact, the estimated maximum $|P_y|$ of the S₂ band in regions E and F (0.1–0.2) is much smaller than that in regions G and H (0.4–0.5). A similar trend is also recognized by comparing the EDCs between regions I and J. These results strongly suggest that the observed y-spin asymmetry is robust to the variation of the sample geometry.

Besides the unusual asymmetry in the in-plane spin polarization, we uncovered a sizable out-of-plane (z) spin component. Figure 4.8c plots the spin-resolved EDCs for the z-spin component. We immediately notice that there exists a sizable difference between the up- and down-spin states, while theoretically predicted out-ofplane spin polarization for simple isotropic Rashba system is zero. Surprisingly, the magnitude of the z-axis spin polarization $|P_z|$ (0.4–0.7) is as large as that of $|P_v|$, establishing that the spin of the S_2 band rotates out of the surface. In addition, P_z abruptly switches the sign even on a single FS sheet: the down-spin state is stronger in the positive k_v (regions E–H) while the up-spin state is stronger in the negative k_v (regions A–D). This suggests that the sign of the z-spin component changes across the $\overline{\Gamma M}$ line. The same trend is also confirmed by the data in regions I and J where the up- and down-spin components almost overlap with each other because of the cancellation of two opposite spins. It is noted that a finite in-plane x spin component mixes in the "z-spin" EDCs owing to the geometrical configuration of the ARPES spectrometer, but its influence to the spin polarization is fairly small (e.g., 3 % at the S_2 pocket when we assume $P_x = 0.1$ and $P_z = 0.5$). To see if a similar trend is observed along another high-symmetry line $\overline{\Gamma K}$, we demonstrate in Figs. 4.8d the spin-resolved EDCs measured in regions K-N. It is apparent that the sign of P_z (also P_x) in region K (L) is the same as that in the region N (M), indicating that P_z (P_x) does not switch the sign across the $\overline{\Gamma K}$ line.

Figure 4.9a highlights the main result of Fig. 4.8 by schematically illustrating the spin polarization vectors of the S_2 band. The in-plane spin component has a vortical structure, but the magnitude of the spin polarization perpendicular to k, called here P_{θ} varies as a function of FS angle θ . P_z has a large component comparable to P_{θ} , and switches the sign by every 60° step of θ . As illustrated in Fig. 4.9b, these features would lead to the periodic oscillation of P_{θ} and P_z , unlike the general Rashba spin-orbit coupling where P_{θ} = const and P_z = 0. The threefold symmetric variation of the z-spin component is naturally understood by considering the threefold crystal symmetry due to the presence of a second bismuth layer.

Now we discuss the origin of unconventional in-plane spin polarization. The observed asymmetry with respect to the $\overline{\Gamma}$ point is not well understood by the general Rashba effect [1]. Moreover, the asymmetry might also break the time-revarsal symmetry $[E(k, \uparrow) = E(-k, \downarrow)]$, since the spin polarization between opposite

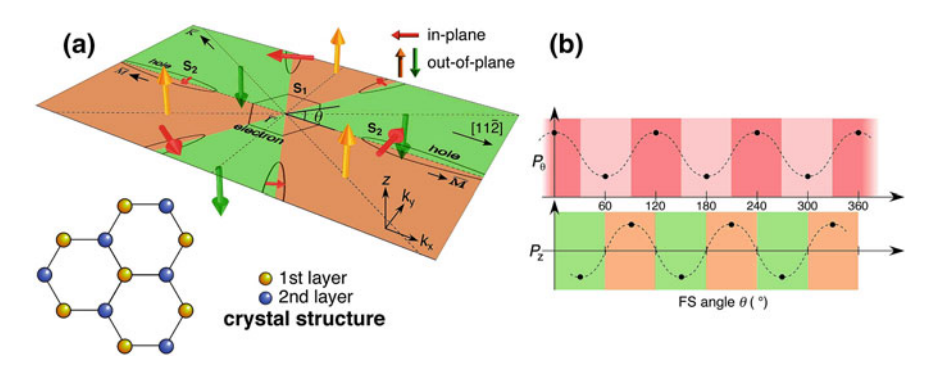


Fig. 4.9 a Schematic view of the spin structure of the S_2 hole pocket in Bi/Si(111). Size (*length*) of arrows roughly scales with the observed spin polarization. Definition of the Fermi surface angle θ is also shown. The data is folded by taking into account the threefold symmetric variation of the bilayer-crystal structure. **b** Schematic view of P_{θ} and P_{τ} as a function of θ

k's is different. If the time-revarsal symmetry breaking really takes place in Bi/Si (111), which only contains nonmagnetic elements, then this is quite intriguing since the time-revarsal symmetry is usually broken by the magnetic order. One cause for the time-revarsal symmetry breaking is the peculiar surface conditions, such as various defects or steps on the surface. This could effectively reduce the symmetry of the spin polarization, although the reproducible nature of the observed spin asymmetry, regardless of the types of Si substrate or the conditions of Bi deposition during the sample preparation, would not be reconciled with this picture. Another possible cause is the final-state effect [16, 17] which does not break the timerevarsal symmetry of the initial state. This effect depends on the vector potential of the incident light, and sometimes causes the observation of false spin polarization for unpolarized bands. It is noted that another research group also reported a similar result using the He I α line (hv = 21.218 eV) [18], suggesting that the observed phenemona is probably final-state independent and this possibility is thus unlikely. While the origin of the in-plane spin asymmetry is unclear at the moment, it would be likely related to the threefold symmetry of the Bi crystal, judged from the periodic pattern of the LEED spots and the ARPES intensity plots.

Next we discuss the out-of-plane spin polarization in relation to other experiments and theories. It has been reported that the out-of-plane spin polarization in some surface alloy systems are caused by the in-plane potential gradient [19–23]. It has been argued that, in the surface alloy system of Bi and Pb on Ag(111), the in-plane potential gradient causes the out-of-plane spin polarization [19, 20]. The distortion of the surface wave function owing to the relaxation or the bucking of the surface Bi atom may also enhance the in-plane potential gradient [23]. In Tl/Si(111) surface which has been fabricated by adsorbing 1 ML Tl on Si(111), the out-of-plane spin polarization, as predicted in group theory, has been also reported [21]. It has been also predicted and observed that the cubic Dresselhaus spin-orbit coupling in Bi₂Te₃ by the $k \cdot p$ theory and spin-resolved ARPES, respectively, responsible for the hexagonal warping of the surface Dirac-cone state, produces a sizable out-of-plane

spin polarization [24, 25]. Thus the appearance of the out-of-plane spin polarization at the Bi surface is likely caused by a similar mechanism as described above. Here it is noted that the ARPES-determined out-of-plane spin polarizaiton and its signchanging behavior (see Fig. 4.9) is in good agreement with the first-principles band calculations of $Bi_{1,y}Sb_y$ [26]. Moreover, the sign-switching behavior of the z spin is consistent with the spin configuration in Au(111) [4] and Bi surface alloys [19], suggesting that the z-spin character is essentially governed by the crystal symmetry. We also note that the x and z components of the spin polarization should vanish on the $\overline{\Gamma M}$ line due to the mirror symmetry. This means that the observed $|P_{\nu}|$ along the $\overline{\Gamma M}$ line would directly reflect the full spin polarization of at most 0.7. This reduction of the full spin polarization is also supported by recent first-principles calculations [27] which predict that the strong spin-orbit entanglement reduces the total spin polarization of the surface states down to 0.5 in Bi₂Se₃ and Bi₂Te₃, although the calculated value of the out-of-plane spin polarizaiton (a few %) is much lower than the value obtained by the ARPES experiment (40-70 %). It is thus necessary to develop a microscopic theory to unravel the observed giant out-of-plane spin polarization.

4.4 Summary

In summary, we found from our spin-resolved ARPES measurements of the Bi thin films on Si(111) that the surface Rashba states show the asymmetry of the in-plane spin polarization and the giant out-of-plane spin polarization. The observed peculiar spin state is not explained in terms of the normal Rashba spin-orbit coupling, and invokes interpretations like time-reversal symmetry breaking and threefold-symmetry of crystal. We concluded that the Bi thin film provides a precious opportunity to investigate the relationship between the spin texture of surface bands and the Rashba spin-orbit coupling that deviates from the ideal 2D system.

References

- 1. Y.A. Bychkov, E.I. Rashba, J. Phys. C 17, 6039 (1984)
- 2. C.R. Ast, H. Höchst, Phys. Rev. Lett. 87, 177602 (2001)
- Y.M. Koroteev, G. Bihlmayer, J.E. Gayone, E.V. Chulkov, S. Blügel, P.M. Echenique, Ph Hofmann, Phys. Rev. Lett. 93, 046403 (2004)
- 4. S. LaShell, B.A. McDougall, E. Jensen, Phys. Rev. Lett. 77, 3419 (1996)
- 5. G. Nicolay, F. Reinert, S. Hüfner, P. Blaha, Phys. Rev. B 65, 033407 (2001)
- J. Henk, M. Hoesch, J. Osterwalder, A. Ernst, P. Bruno, J. Phys.: Condens. Matter 16, 7581 (2004)
- M. Hoesch, M. Muntwiler, V.N. Petrov, M. Hengsberger, L. Patthey, M. Shi, M. Falub, T. Greber, J. Osterwalder, Phys. Rev. B 69, 241401(R) (2004)
- 8. J. Nitta, T. Akazaki, H. Takayanagi, T. Enoki, Phys. Rev. Lett. 78, 1335 (1997)
- 9. Ph Hofmann, Prog. Surf. Sci. 81, 191 (2006)

- T. Hirahara, T. Nagao, I. Matsuda, G. Bihlmayer, E.V. Chulkov, Y.M. Koroteev, P.M. Echenique, M. Saito, S. Hasegawa, Phys. Rev. Lett. 97, 146803 (2006)
- T. Hirahara, K. Miyamoto, I. Matsuda, T. Kadono, A. Kimura, T. Nagao, G. Bihlmayer, E.V. Chulkov, S. Qiao, K. Shimada, H. Namatame, M. Taniguchi, S. Hasegawa, Phys. Rev. B 76, 153305 (2007)
- A. Kimura, E.E. Krasovskii, R. Nishimura, K. Miyamoto, T. Kadono, K. Kanomaru, E.V. Chulkov, G. Bihlmayer, K. Shimada, H. Namatame, M. Taniguchi, Phys. Rev. Lett. 105, 076804 (2010)
- 13. E. Schlier, H.E. Farnsworth, J. Chem. Phys. **30**, 917 (1959)
- K. Takayanagi, Y. Tanishiro, M. Takahashi, S. Takahashi, J. Vac. Sci. Technol. A 3, 1502 (1985)
- 15. J. Viernow, J.L. Lin, D.Y. Petrovykh, F.M. Leibsle, F.K. Men, F.J. Himpsel, Appl. Phys. Lett. 72, 948 (1998)
- 16. J. Kirschner, R. Feder, J.F. Wendelken, Phys. Rev. Lett. 47, 614 (1981)
- 17. H.P. Oepen, K. Hunlich, J. Kirschner, Phys. Rev. Lett. **56**, 496 (1986)
- 18. H. Miyahara, T. Maegawa, K. Kuroda, A. Kimura, K. Miyamoto, H. Namatame, M. Taniguchi, T. Okuda, e-J. Surf. Sci. Nanotech. 10, 153 (2012)
- C.R. Ast, J. Henk, A. Ernst, L. Moreschini, M.C. Falub, D. Pacilé, P. Bruno, K. Kern, M. Grioni, Phys. Rev. Lett. 98, 186807 (2007)
- 20. F. Meier, H. Dil, J. Lobo-Checa, L. Patthey, J. Osterwalder, Phys. Rev. B 77, 165431 (2008)
- K. Sakamoto, T. Oda, A. Kimura, K. Miyamoto, M. Tsujikawa, A. Imai, N. Ueno, H. Namatame, M. Taniguchi, P.E.J. Eriksson, R.I.G. Uhrberg, Phys. Rev. Lett. 102, 096805 (2009)
- 22. K. Yaji, Y. Ohtsubo, S. Hatta, H. Okuyama, K. Miyamoto, T. Okuda, A. Kimura, H. Namatame, M. Taniguchi, T. Aruga, Nat. Commun. 1, 17 (2010)
- 23. G. Bihlmayer, S. Blugel, E.V. Chulkov, Phys. Rev. B 75, 195414 (2007)
- 24. L. Fu, Phys. Rev. Lett. 103, 266801 (2009)
- S. Souma, K. Kosaka, T. Sato, M. Komatsu, A. Takayama, T. Takahashi, M. Kriener, K. Segawa, Y. Ando, Phys. Rev. Lett. 106, 216803 (2011)
- H.J. Zhang, C.X. Liu, X.L. Qi, X.Y. Deng, X. Dai, S.C. Zhang, Z. Fang, Phys. Rev. B 80, 085307 (2009)
- 27. O.V. Yazyev, J.E. Moore, S.G. Louie, Phys. Rev. Lett. 105, 266806 (2010)

Chapter 5 Rashba Effect at Interface of a Bi Thin Film on Si(111)

The electronic structure of the bismuth thin film near the \overline{M} point varies depending on the film thickness d due to the quantization along the thickness direction (perpendicular to the surface). In this chapter, we describe the relationship between the spin polarization of the spin-split Rashba bands and the film thickness near the \overline{M} point of the Bi/Si(111) thin film, as clarified by spin-resolved ARPES. We also show that the spin polarization of the surface states near the \overline{M} point is gradually reduced on decreasing thickness and almost vanishes at d=8 BL. Such an unexpected variation in the polarization value is well understood in term of the hybridization between the Rashba-state wave functions at the vacuum-side surface and the Si-substrate-side interface.

5.1 Background and Goal of Research

The Chap. 5 focuses on the spin structure around the \overline{M} point of the Bi/Si(111) thin film, while the anisotropic spin structure around the $\overline{\Gamma}$ point has been shown in Chap. 4. One of the unsolved phenomena at the \overline{M} point of the Bi thin film is the origin of an electronlike band which also forms the Fermi surface (FS). As shown in Fig. 5.1a, it is predicted from the band structure calculations and the previous ARPES experiments that the band at the \overline{M} point originates from the spin-polarized surface state [1, 2]. However, it is not evident that the band structure observed by ARPES is really of the surface-state origin because the bulk bands overlap with the surface state near the \overline{M} point. Also, it was difficult to discuss the detail of the spin structure around the \overline{M} point due to insufficient energy resolution of the spinresolved ARPES spectrometers (Fig. 5.1b) [2]. Moreover, the existence of the band gap at the \overline{M} point is an unresolved issue. In the calculations, the spin-split bands only degenerate at the high-symmetry point like the $\overline{\Gamma}$ point as shown Fig. 5.2a [1]. At the \overline{M} point, two kinds of bands exist, one is an electronlike band which cross the Fermi level, and the other is a hole like band which is a part of the quantum-well states (QWSs). These bands are regarded as the surface states, judged from the band

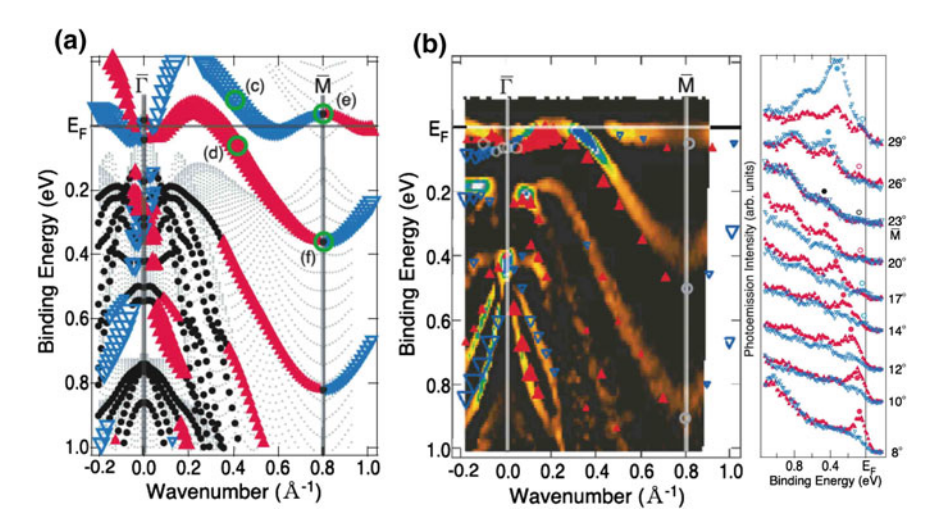


Fig. 5.1 a Spin-polarized band structure of the ab initio calculations for free-standing 7 BL Bi slabs [2]. **b** The spin-split band dispersion of the 7 BL Bi(111) films obtained from spin-resolved ARPES is overlaid on the dispersion obtained by the regular ARPES [2]. The *up* (*down*) spin is shown by the *red* (*blue*) triangles and the magnitude of the spin polarization is shown by the size of the markers

dispersion near the $\overline{\Gamma}$ point, while these states form a band gap although the \overline{M} point is another high-symmetry point of the Brillouin zone (BZ) [3, 4]. Furthermore, the surface state appears to be smoothly connected to the QWSs independent of the film thickness, while the energy interval between the QWSs and the surface state varies upon changing the film thickness. All these results indicate that the film-thickness dependence of the spin polarization is still unclear at present. It is noted that in the case of the ultrathin film, one should also take account into the effect of the substrate and the growth condition of the film.

In this chapter, we report the thickness-dependent ARPES study of the Bi thin film, and discuss the origin of the electronlike band and the thickness dependence of the spin polarization near the \overline{M} point.

5.2 Results and Discussions

Bi thin films used for the ARPES measurements were prepared with the following steps; first a Si(111) substrate was cleaned at 1,000 °C to obtain the well-ordered 7 \times 7 surface, next Bi atoms were deposited on Si(111) substrate at room temperature, and then the film was annealed at 150 °C. The film thickness was controlled by varying the deposition time with keeping the constant deposition rate (0.09 Å/s), and was estimated by the quartz-oscillator thickness monitor and the energy position of the quantum well states (QWSs) in the ARPES spectra [2, 3]. The 1 \times 1

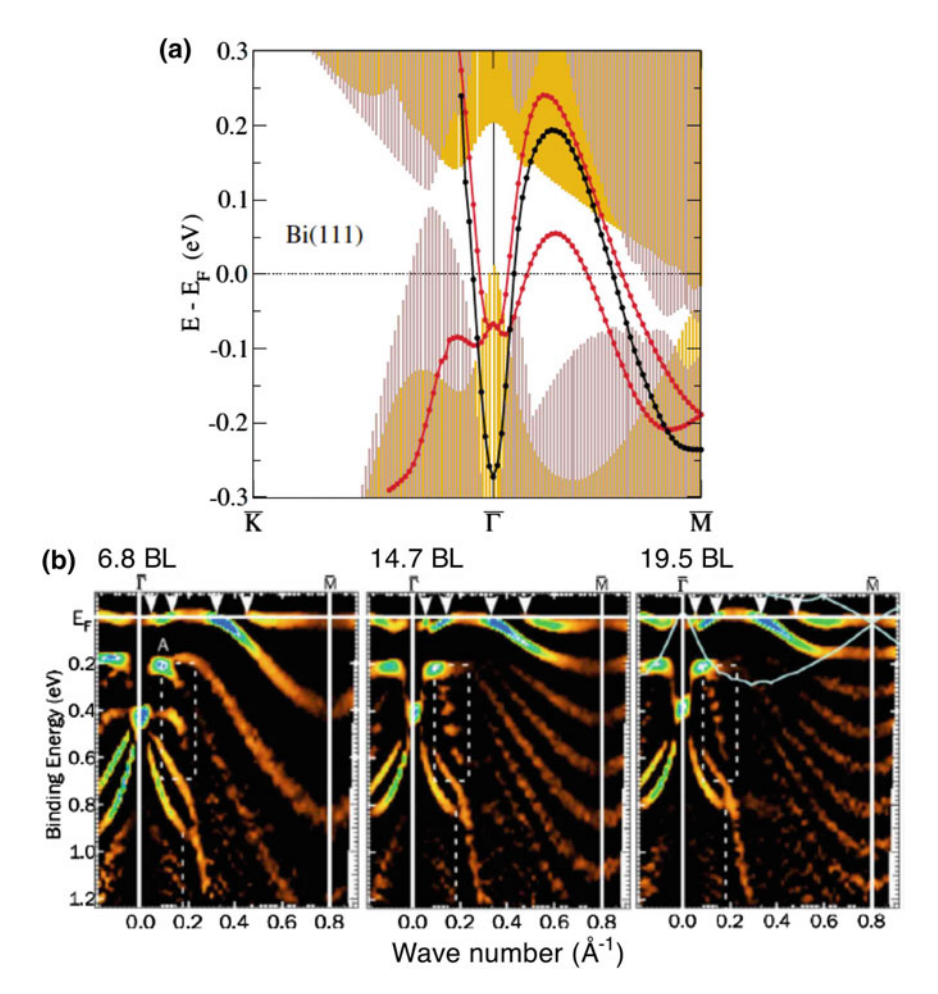


Fig. 5.2 a Surface states of Bi(111) calculated without (*black*) and with (*red*) spin-orbit splitting [1]. The shaded areas show the projection of the bulk bands. **b** The band dispersion image for the 6.8 BL, 14.7 BL and 19.5 BL films

surface structure was confirmed by the low-energy electron diffraction measurement (LEED). ARPES measurements were performed using the spin-resolved ARPES spectrometer as described in Chap. 3. We used one of the Xe I lines (hv = 8. 437 eV). The energy resolutions during the spin-resolved and regular ARPES measurements were 40 and 6 meV, respectively. The Sherman function value was set at 0.07. We could repeatedly use the same Si substrate by a flashing at 1,000 °C.

Figure 5.3a shows the experimentally determined Fermi surface of the Bi thin film with the thickness d of 40 BL (bilayer) grown on a Si(111) substrate along the $\overline{\Gamma}\overline{M}$ line of the surface BZ. As already discussed in Chap. 4, we confirms three kinds of FSs; a small FS centered at the $\overline{\Gamma}$ point (S₁) and surrounding elongated

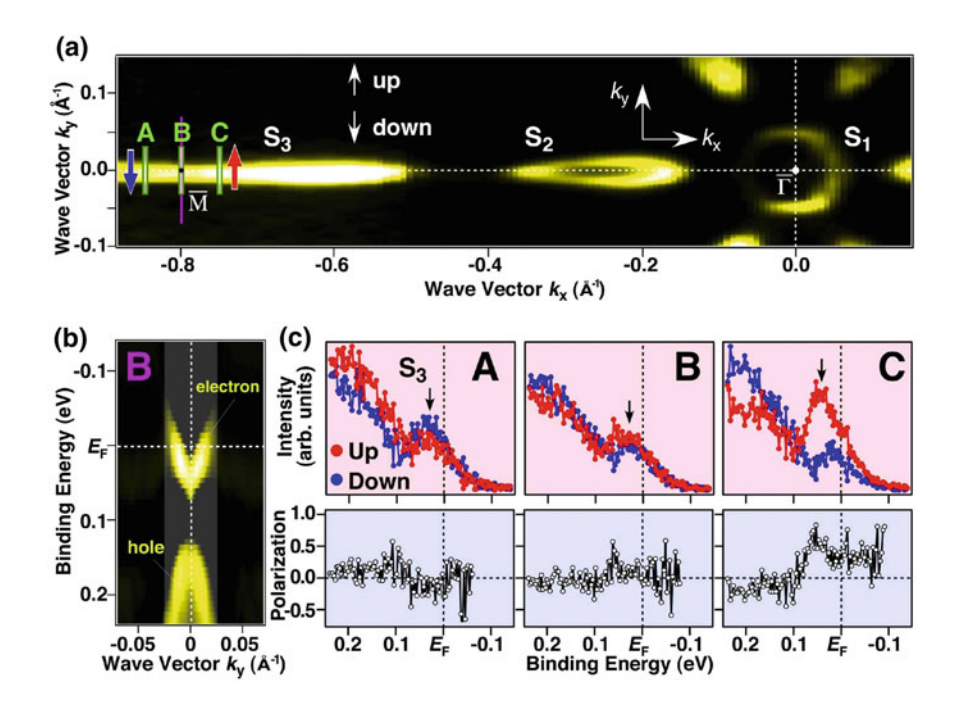


Fig. 5.3 a Plot of the ARPES intensity at $E_{\rm F}$ around the $\overline{\Gamma \rm M}$ line as a function of 2D wave vector on Bi/Si(111) for d=40 BL measured with the Xe I line at 30 K. b Plot of the ARPES intensity near $E_{\rm F}$ as a function of wave vector $k_{\rm y}$ and binding energy measured along cut B (purple line) in a at 300 K. Shaded area represents the k window of the spin-resolved measurement. c Top panels show the spin-resolved EDCs in the vicinity of $E_{\rm F}$ measured in k regions A–C [rectangle areas in a], while the bottom panels display the corresponding spin polarizations

pockets (S_2), together with the ellipsoidal pocket (S_3) near the \overline{M} point. This chapter focuses on the S_3 FS whose detailed spin structure has not been explored previously [4]. As shown in Fig. 5.3b which displays the ARPES intensity along the \overline{MK} cut at T=300 K [cut B in Fig. 5.3a], the S_3 band shows an electronlike dispersion with its bottom energy located at ~ 30 meV below Fermi energy (E_F). This band is well separated from the holelike band at higher binding energy (E_F) arising from the QWSs that originate from the confinement of the wave function in the direction perpendicular to the surface (z direction) [1]. Although the \overline{M} point ($K_y=0$) at cut B is the time-reversal invariant momentum, there is no evidence for the Kramers degeneracy of the S_3 band nor the QWSs, unlike the naive expectation from the requirement of the time-reversal symmetry which is not explicitly broken in the present system. Such an absence of the Kramers degeneracy at the \overline{M} point has also been observed in the previous ARPES study of the Bi thin films and was interpreted in terms of the hybridization of the surface states and the QWS [5, 6].

In the normal Rashba picture, the in-plane polarization vector is perpendicular to k, and thus the spin has a helical texture which points to the clockwise direction with respect to the $\overline{\Gamma}$ point for the S₃ band, as denoted by a red arrow in Fig. 5.3a.

By taking into account the requirement from the time-reversal symmetry where the spin-dependent energy dispersion satisfies $E(\mathbf{G} + k, \uparrow) = E(\mathbf{G} - k, \downarrow)$ with respect to the time-reversal invariant momentum G, the spin direction should be reversed across the \overline{M} point as shown by a blue arrow in Fig. 5.3a, namely, spin polarization might show down- (up-) spin component in region A (C), and spin polarization vanishes in region B. Such a spin-reversing behavior is indeed observed in the spinresolved energy distribution curves (EDCs) displayed in Fig. 5.3c which has been obtained in the shaded area in Fig. 5.3b. All of the EDCs mainly consist of two components, a slope-like feature which rapidly increases its intensity at $E_{\rm B}$ > 0.1 eV, and a peak feature at \sim 50 meV. The former corresponds to the tail of the QWS, while the latter is assigned as the S_3 band. The up-spin intensity of the S_3 band is superior in the first BZ (see an arrow in region C), while it gradually reduces on approaching the \overline{M} point (region B) and eventually appears to be prevailed by the down-spin counterpart in the second BZ (region A). These results are qualitatively consistent with the Rashba picture, and suggest that the S₃ band is a spin-split Rashba surface band. The observed difference (asymmetry) in the shape of the S₃ band in spin-resolved EDCs between region A and C may be due to the matrixelement effect of the photoelectron intensity whose influence would be enhanced as one moves away from the $\overline{\Gamma}$ point (at higher emission angle of photoelectrons).

Another interesting aspect in Fig. 5.3c is that the tail of the QWS also has a finite polarization and its spin vector points to an opposite direction relative to that of the S_3 band, whereas the QWS is theoretically expected to be spin-degenerated since it originates from the bulk band. One of the possibilities is hybridization between the surface state and the QWS because the spin-polarization of the QWS shows the same direction as the Rashba-split surface state. It is also possible to interpret that the spin degeneracy is lifted and a band gap is formed at the \overline{M} point [2, 7]. Another possibility is that the initial states around the surface are spin polarized due to the reflection of wave function of the QWS from the surface barrier, and such a polarization of spins is detected by the surface-sensitive ARPES technique, similarly to the case of bulk Bi crystal [8]. It is noted that out-of-plane (z) spin component is also measured and not observed in region A-C. In addition, this behavior is common to all the measurements performed around the \overline{M} point. Thus we omit the presentation of the out-of-plane spin component hereafter.

What happens to the band structure when we alter the film thickness d? A direct answer is demonstrated in Fig. 5.4a which plots the band dispersion along the $\overline{\rm MK}$ cut (left panels) and the corresponding EDCs at the $\overline{\rm M}$ point (right panels) for various d values of 8–40 BL. As clearly visible, we identify an oscillating feature in the EDC at $E_{\rm B}=0.1$ –0.25 eV for d=40 BL. These hump structures originate from the multiple QWSs with the top of dispersion at binding energy as indicated by allows. Surprisingly, each QWS can be distinguished even for d=40 BL which is in the thickest regime of the ARPES measurements of the Bi thin films performed thus far [1, 5], demonstrating the high-quality well-ordered nature of our films as also confirmed by the atomic-force microscopy measurements. Upon decreasing d, the top of the highest QWS shifts downward, and simultaneously the energy

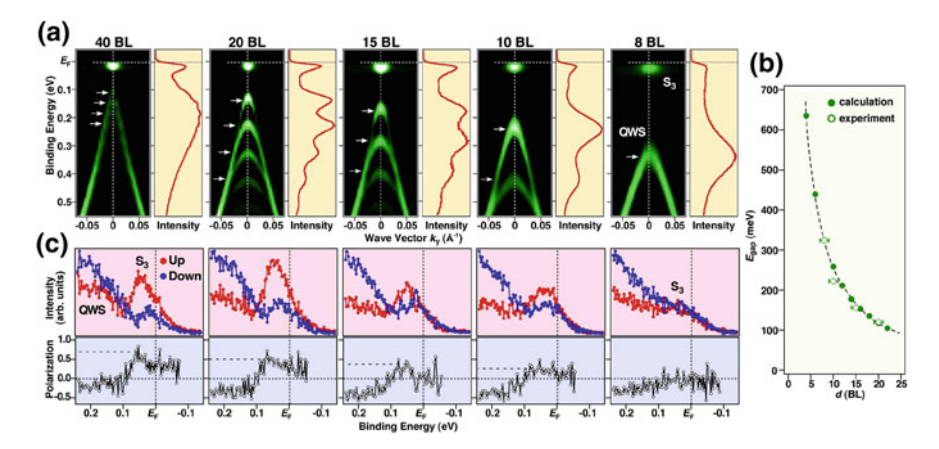


Fig. 5.4 a Thickness-dependence of the band dispersion near $E_{\rm F}$ along cut B in Fig. 5.3a (the $\overline{\rm MK}$ cut), obtained by taking the second derivative of the EDCs at 30 K. EDC at the $\overline{\rm M}$ point is also shown for each thickness. b Comparison of the thickness-dependence of the $E_{\rm gap}$ value between the ARPES experiments and the band calculations. c (top) Corresponding spin-resolved EDCs and (bottom) their spin polarizations for region C in Fig. 5.3a

separation of each QWS becomes wider, enabling us to unambiguously indentify the overall energy dispersion of the individual QWS in both the EDCs and the band-dispersion plots. Such a systematic change in the QWSs is a fingerprint of the well-confined nature of the valence-band wave functions within the film, as described by the phase-accumulation model [7]. In Fig. 5.4b, we plot the experimentally determined energy interval between the bottom of the S_3 band and the top of the QWS (here we call $E_{\rm gap}$) at the $\overline{\rm M}$ point, compared with that of the band calculation. Band calculations were carried out by Prof. T. Oguchi in Osaka University, by means of a first-principles density-functional-theory approach with the all-electron full-potential linearized augmented-plane-wave method in a scalar-relativity plus spin-orbit-coupling manner. Thin-film systems were simulated by adopting free-standing periodic slab models with vacuum layer. Interestingly, we found a reasonable agreement between the two, suggesting that the QWS indeed originates from the quantization of the bulk band, supporting the free-standing nature of the Bi film.

Unexpected physics manifests itself by looking at the spin-resolved EDCs displayed in Fig. 5.4c measured for region C in Fig. 5.3a. One may naturally expect that the intensity ratio of the up- and down-spin bands (or the spin polarization P) of the Rashba surface states is not influenced by the variation of d since the Rashba states may have a surface-localized nature. However, the present result clearly demonstrates that the observed P highly depends on d. As recognized in the EDCs for d = 40 and 20 BL, there exists a sizable difference in the intensity of the up-spin component with respect to the down-spin counterpart in the S_3 band, whereas such a difference is less pronounced for thinner films of d = 15 and 10 BL. Eventually,

the difference becomes indistinguishable at d=8 BL. In fact, the obtained P value which has a maximum at ~ 0.7 at d=40 BL (see lower panel of Fig. 5.4c gradually reduces upon decreasing d, and finally reaches ~ 0 at d=8 BL. Intriguingly, the P value of the QWS keeps nearly the same irrespective of d, suggesting that the thickness-dependent P is the characteristics of the Rashba surface states.

Figure 5.5 displays the experimentally-determined maximal P value of the S_3 band plotted as a function of the film thickness d and the energy-gap size between the bottom of the S_3 band and the top of the QWS at the \overline{M} point $(E_{\rm gap})$. We immediately notice that the P value monotonically increases on increasing d or on reducing $E_{\rm gap}$. The P value is 0.7 ± 0.1 for d = 40 BL $(E_{\rm gap} = 100 \text{ meV})$ in contrast to $P = 0.05 \pm 0.1$ for d = 8 BL $(E_{\rm gap} = 320 \text{ meV})$, quantitatively establishing the thickness-dependent variation of P.

Here we discuss the physical mechanism behind the unusual thickness dependence of P. According to the scanning tunneling microscopy and the electron diffraction experiments [9–11], the coupling between the Bi film and the Si(111)

Fig. 5.5 Maximum spin polarization plotted as a function of the film thickness d and the energy gap size E_{gap} between the *top* of the QWS and the *bottom* of the S_3 band

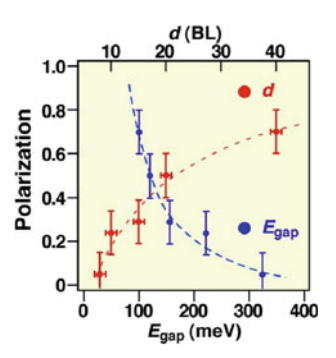
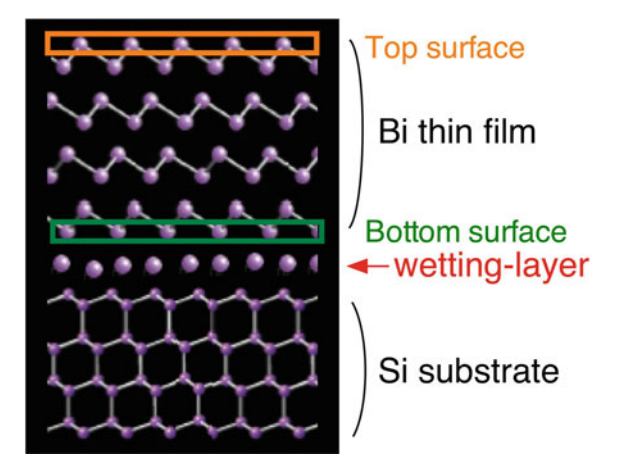
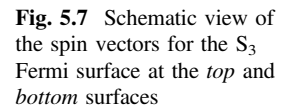
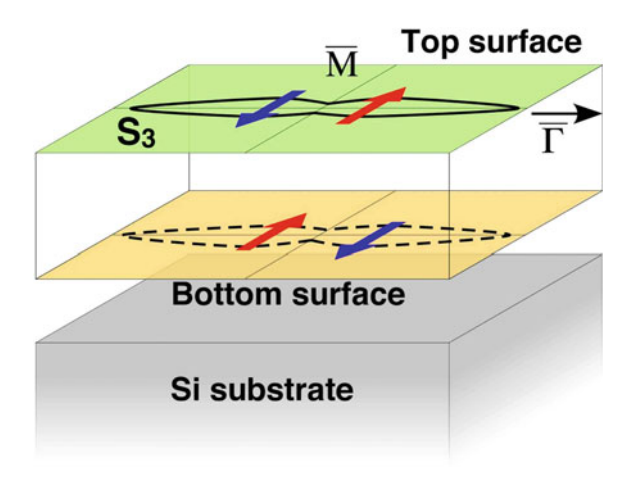


Fig. 5.6 Schematic view of the Bi thin film on Si(111) substrate. The wetting layer exists between Bi then film and Si







substrate is fairly weak due to the presence of a disordered wetting layer at the interface (see Fig. 5.6), suggesting that the Bi film is nearly freestanding. In such a case, the Bi/Si interface can be regarded as another surface (bottom surface) where the Rashba states similar to those at the vacuum-side surface (top surface) would emerge [2, 12, 13] due to the breaking of the space-inversion symmetry at the interface. These two distinct Rashba states should have opposite spin directions because of the symmetry requirement, as illustrated in Fig. 5.7. When the Bi film is thick enough (ultimately the bulk case), the two Rashba states are independent from each other, and there is no hybridization of their wave functions. On reducing d, the wave functions of the two Rashba states start to overlap and hybridize, leading to the admixture of the up- and down-spin states. When the hybridization becomes strong in the thin limit, the observed P would become substantially small. This simple picture nicely explains the observed general trend of the thickness dependence of P. In addition, the absence of the Kramers degeneracy at the \overline{M} point and the large $E_{\rm gap}$ value for the smaller-d samples (see Fig. 5.4a would be also consistent with the stronger hybridization effect for the thinner films [12].

One may think that the hybridization of the top and bottom surfaces is not necessary to account for the reduction of P in a thin film, since it is possible to simultaneously observe both top- and bottom-surface states because of a finite photoelectron escape depth λ . In the present experiment, λ is 20 - 40 Å [14] and the film thickness is ~ 30 Å in the thinnest case of d = 8 BL. The calculated P becomes 0.4 - 0.65 when we assume fully polarized spins and the surface-localized nature of the Rashba states. This value is in stark contrast to the experimentally obtained negligibly small P value for d = 8 BL, demonstrating the importance of the hybridization effect to account for the observed unusual P reduction. It is also noted that the reduction of experimental P is already seen in the film of d = 20 BL (see Fig. 5.5), suggesting that the decay length of the surface-state wave function is around at least 20 BL (~ 80 Å). While the origin of this large decay length is unclear at present, a thin film of Bi₂Se₃ topological insulator also exhibits a similar decay

length, as inferred from the experimental fact that the hybridization gap starts to open at six quintuple layers (~60 Å) [12].

Present observation also suggests the possibility of generating spin-polarized electrons with any desired P values, when one selectively extracts electrons from the Rashba surface states by specifying the electron momentum. Such a tunable P may have potential applications like the spin-polarized source (spin injector) with variable P, which is very useful for the characterization of the device performance in spintronics. In addition, an interface is more stable than the surface in application point of view. The Rashba parameter of Bi ($\alpha_R \sim 0.56 \text{ eVÅ}$ [15]) is one order of magnitude larger than that one of semiconductor heterostructure [16], which is preferable for the control of the spin current. The present result also indicates the necessity to incorporate a finite size effect into the correct understanding of the spin-dependent surface transport phenomena in the strong spin-orbit-coupling systems such as the Rashba metals and the topological insulators.

5.3 Summary

In order to elucidate the surface spin-polarization depending on the film thickness of Bi/Si(111), we have performed spin-resolved ARPES measurement near the $\overline{\rm M}$ point. In the electron-like band, the spin polarization consistent with the Rashba effect has been observed. The spin polarization of the surface states was reduced on decreasing thickness. Such an unexpected behavior in the spin-polarization value is explained by the hybridization of electron wave functions between "top-" and "bottom-" surfaces.

References

- Y.M. Koroteev, G. Bihlmayer, J.E. Gayone, E.V. Chulkov, S. Blügel, P.M. Echenique, Ph Hofmann, Phys. Rev. Lett. 93, 046403 (2004)
- T. Hirahara, K. Miyamoto, A. Kimura, Y. Niinuma, G. Bihlmayer, E.V. Chulkov, T. Nagao, I. Matsuda, S. Qiao, K. Shimada, H. Namatame, M. Taniguchi, S. Hasagawa, New J. Phys. 10, 083038 (2008)
- T. Hirahara, T. Nagao, I. Matsuda, G. Bihlmayer, E.V. Chulkov, Y.M. Koroteev, S. Hasegawa, Phys. Rev. B 75, 035422 (2007)
- 4. A. Takayama, T. Sato, S. Souma, T. Takahashi, Phys. Rev. Lett. 106, 166401 (2011)
- 5. Ph Hofmann, Prog. Surf. Sci. **81**, 191 (2006)
- T. Hirahara, T. Nagao, I. Matsuda, G. Bihlmayer, E.V. Chulkov, Y.M. Koroteev, P.M. Echenique, M. Saito, S. Hasegawa, Phys. Rev. Lett. 97, 146803 (2006)
- T. Hirahara, K. Miyamoto, I. Matsuda, T. Kadono, A. Kimura, T. Nagao, G. Bihlmayer, E.V. Chulkov, S. Qiao, K. Shimada, H. Namatame, M. Taniguchi, S. Hasegawa, Phys. Rev. B 76, 153305 (2007)

- A. Kimura, E.E. Krasovskii, R. Nishimura, K. Miyamoto, T. Kadono, K. Kanomaru, E.V. Chulkov, G. Bihlmayer, K. Shimada, H. Namatame, M. Taniguchi, Phys. Rev. Lett. 105, 076804 (2010)
- 9. T. Nagao, J.T. Sadowski, M. Saito, S. Yaginuma, Y. Fujikawa, T. Kogure, T. Ohno, Y. Hasegawa, S. Hasegawa, T. Sakurai, Phys. Rev. Lett. **93**, 105501 (2004)
- T. Nagao, S. Yaginuma, J.T. Sadowski, M. Saito, Y. Fijikawa, T. Ohno, S. Hasegawa, T. Sakurai, J. Surf. Sci. Soc. Jpn. 26, 344 (2005) (in Japanese)
- 11. T. Shirasawa, M. Ohyama, W. Voegeli, T. Takahashi, Phys. Rev. B 84, 075411 (2011)
- Y. Zhang, K. He, C.Z. Chang, C.L. Song, L.L. Wang, X. Chen, J.F. Jia, Z. Fang, X. Dai, W.Y. Shan, S.Q. Shen, Q. Niu, X.L. Qi, S.C. Zhang, X.C. Ma, Q.K. Xue, Nat. Phys. 6, 584 (2010)
- 13. G. Bian, T. Miller, T.C. Chiang, Phys. Rev. Lett. 107, 036802 (2011)
- 14. M.P. Seah, W.A. Dench, Surf. Interface Anal. 1, 2 (1979)
- C.R. Ast, J. Henk, A. Ernst, L. Moreschini, M.C. Falub, D. Pacilé, P. Bruno, K. Kern, M. Grioni, Phys. Rev. Lett. 98, 186807 (2007)
- 16. J. Nitta, T. Akazaki, H. Takayanagi, T. Enoki, Phys. Rev. Lett. 78, 1335 (1997)

Chapter 6 Conclusion

We have developed an ultrahigh-resolution spin-resolved photoemission spectrometer with a highly efficient mini Mott detector, and uncovered the anomalous Rashba effect of Bi/Si(111) thin film by using the developed spectrometer. In this chapter, conclusions regarding the development of the spin-resolved photoemission spectrometer and the spin-resolved ARPES results of the Bi Rashba effect are made.

6.1 Development of Ultrahigh-Resolution Spin-Resolved Photoemission Spectrometer

We have developed a new spin detector with a large acceptance angle and a flat target to increase the efficiency of the Mott detector. The scattering efficiency of the Mott detector achieved 2.3×10^{-2} . To perform the regular and spin-resolved ARPES measurements at the same time, the MCP was shifted toward the innersphere of the hemispherical electron analyzer. The electron deflector situated between the Mott detector and analyzer enabled the determination of the spin polarization in three independent directions. We have solved the discharge problem of the Mott detector, and have achieved the noise level of ~0.1 cps at 25 kV. In order to fabricate high-quality samples and perform in-situ measurements, a surface chamber connected to the spin-resolved ARPRS spectrometer has been constructed. Energy resolution of spectrometer was checked by measuring the Fermi edge of polycrystalline gold, and it is estimated to be 0.9 and 8 meV for non-spin-resolved and spin-resolved modes, respectively. The performance test of the spectrometer was performed by measuring well-separated spin-polarized Rashba-split surface bands in Bi(111). The effective Sherman function S_{eff} of the Mott detector is estimated as 0.07 ± 0.01 by measuring the Au(111) surface state.

80 6 Conclusion

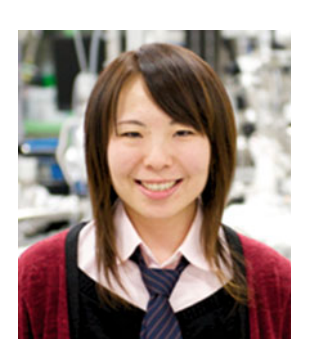
6.2 Elucidation of Rashba Effect for Bi/Si(111) Thin Film by Spin-Resolved ARPES

We have performed high-resolution spin- and angle-resolved photoemission spectroscopy of Bi/Si(111) thin film to investigate the spin structure of surface states. We found from experimental results that the surface Rashba states display the asymmetry of the in-plane spin polarization and the giant out-of-plane spin polarization. Specially, the out-of-plane spin polarization switches the sign across the $\overline{\Gamma M}$ line. The observed peculiar spin state is not explained in terms of the normal Rashba spin-orbit coupling, and invokes interpretations like time-reversal symmetry breaking and threefold-symmetry of crystal. In order to clarify the surface spin-polarization depending on the film thickness of Bi/Si(111), we have performed spin-resolved ARPES measurement near the \overline{M} point. The spin polarization of the electron-like surface band was reduced on decreasing thickness. Such an unexpected behavior in the spin-polarization value is explained by the hybridization of electron wave functions between "top-" and "bottom-" surfaces.

6.3 Future Plans

These results demonstrate that the high-resolution spin-resolved ARPES technique opens a pathway to studying the novel spin states of various materials such as surface Rashba systems, half metals, and topological insulators. The Rashba effect is expected to be applicable to spintronic devices without using ferromagnetism nor applying the magnetic field. On the other hand, the Rashba state at the interface has not been well investigated due to the difficulties in directly detecting the interface electronic states, while the interface plays an important for device applications in many aspects. The next step of this study is to elucidate the interface Rashba states in more detail in various systems, by developing a spin-resolved ARPES system with higher performance.

Curriculum Vitae



Akari Takayama

Address (Former affiliation) 2-1-1 Katahira, Aoba-ku, Sendai, Miyagi 980-8577, Japan

Tel.: +81-22-217-6169 Fax: +81-22-217-6157

e-mail: a.takayama@arpes.phys.tohoku.ac.jp

Education

Tohoku University

Degree: M.S. 2008, Ph.D. March 2013 Thesis advisor: Takashi Takahashi

Thesis topic: Construction of high-resolution spin-resolved photoemission

spectrometer and the study of Rashba effect in bismuth thin film

Fukushima University

Degree: March 2004, B.A. in Education

Major Honors and Awards

Ikushi prize, Japan Society for the Promotion of Science, March 4 (2013) President's Award, Tohoku University, March 27 (2013) L'Oréal–UNESCO award of Japan for women in science, September 11 (2013) 82 Curriculum Vitae

Relevant Employment History

Japan Society for the Promotion Science (JSPS) Research Fellowship for young scientists, 2010–2012

Research Interests

I am interested in novel phenomena occurring in two-dimensional states like surface and thin film. Recently, it has been reported in such systems that anomalous spin structure like the Rashba effect exists due to the strong spin-orbit coupling. I have been very much interested in these phenomena. When one intend to understand the spin structure in the Rashba system, it is indispensable to determine three quantum parameters of electron, i.e. energy, momentum, and spin. Spin- and angle-resolved photoemission spectroscopy is a powerful technique to observe all of these parameters, while this method involves an inherent difficulty in achieving a high-energy resolution. During my Ph.D. course, I have solved this problem with lots of trials and errors, and developed high-performance spectrometer. Moreover, I studied the Rashba spin-split surface states of Bi thin film by using this spin-resolved photoemission spectrometer, and have found anomalous behavior of the spin structure in the surface states.

Publication List

- [1] "Anomalous Rashba effect of Bi(111) thin film studied by high-resolution spin-resolved ARPES" A. Takayama, T. Sato, S. Souma, T. Takahashi, J. Vac. Sci. Tech. B **30**, 04E107 (2012)
- [2] "Development of high-resolution spin-resolved photoemission spectrometer and its application for study of surface Rashba effects" (in Japanese) A. Takayama, S. Souma, T. Takahashi, J. Surf. Sci. Soc. Jpn. 33, 165 (2012)
- [3] "Spin Polarization of Gapped Dirac Surface States Near the Topological Phase Transition in TlBi(S_{1-x}Se_x)₂" S. Souma, M. Komatsu, M. Nomura, T. Sato, A. Takayama, T. Takahashi, K. Eto, K. Segawa, Y. Ando, Phys. Rev. Lett. 109, 186804 (2012)
- [4] "Direct Measurement of the Out-of-Plane Spin Texture in the Dirac Cone Surface State of a Topological Insulator" S. Souma, K. Kosaka, T. Sato, M. Komatsu, A. Takayama, T. Takahashi, M. Kriener, K. Segawa, Y. Ando, Phys. Rev. Lett. 106, 216803 (2011)

Curriculum Vitae 83

[5] "Evolution of surface states in Bi_{1-x}Sb_x alloys across the topological phase transition" H. Guo, K. Sugawara, A. Takayama, S. Souma, T. Sato, N. Satoh, A. Ohnishi, M. Kitaura, M. Sasaki, Q.-K. Xue, T. Takahashi, Phys. Rev. B 83, 201104(R) (2011)

- [6] "Magnetic Phase Transition of CeSb Studied by Low-Energy Angle-Resolved Photoemission Spectroscopy" A. Takayama, S. Souma, T. Sato, T. Arakane, T. Takahashi, J. Phys. Soc. Jpn. 78, 073702 (2009)
- [7] "Observation of Fermi-surface-dependent nodeless superconducting gaps in Ba_{0.6}K_{0.4}Fe₂As₂" H. Ding, P. Richard, K. Nakayama, K. Sugawara, T. Arakane, Y. Sekiba, A. Takayama, S. Souma, T. Sato, T. Takahashi, Z. Wang, X. Dai, Z. Fang, G. F. Chen, J. L. Luo N. L. Wang, Europhysics Letters 83, 47001 (2008)